



LAWRENCE
LIVERMORE
NATIONAL
LABORATORY

Development of High Resolution X-Ray spectrometers for the Investigation of Bioinorganic Chemistry in Metalloproteins

O. B. Drury

June 22, 2007

Disclaimer

This document was prepared as an account of work sponsored by an agency of the United States Government. Neither the United States Government nor the University of California nor any of their employees, makes any warranty, express or implied, or assumes any legal liability or responsibility for the accuracy, completeness, or usefulness of any information, apparatus, product, or process disclosed, or represents that its use would not infringe privately owned rights. Reference herein to any specific commercial product, process, or service by trade name, trademark, manufacturer, or otherwise, does not necessarily constitute or imply its endorsement, recommendation, or favoring by the United States Government or the University of California. The views and opinions of authors expressed herein do not necessarily state or reflect those of the United States Government or the University of California, and shall not be used for advertising or product endorsement purposes.

This work was performed under the auspices of the U.S. Department of Energy by University of California, Lawrence Livermore National Laboratory under Contract W-7405-Eng-48.

Development of High Resolution X-Ray Spectrometers for the Investigation of Bioinorganic Chemistry in Metalloproteins

By

OWEN BYRON DRURY

B.S. (California State University, Sacramento) 1992

M.S. (University of California, Davis) 2000

DISSERTATION

Submitted in partial satisfaction of the requirements for the degree of

DOCTOR OF PHILOSOPHY

in

Biophysics

In the

OFFICE OF GRADUATE STUDIES

of the

UNIVERSITY OF CALIFORNIA,

DAVIS

Approved:

Stephen P. Cramer

Daniel L. Cox

Stephan Friedrich

Committee in Charge

2007

Auspices

This document was prepared as an account of work sponsored by an agency of the United States Government. Neither the United States Government nor the University of California nor any of their employees, makes any warranty, express or implied, or assumes any legal liability or responsibility for the accuracy, completeness, or usefulness of any information, apparatus, product, or process disclosed, or represents that its use would not infringe privately owned rights. Reference herein to any specific commercial product, process, or service by trade name, trademark, manufacturer, or otherwise, does not necessarily constitute or imply its endorsement, recommendation, or favoring by the United States Government or the University of California. The views and opinions of authors expressed herein do not necessarily state or reflect those of the United States Government or the University of California, and shall not be used for advertising or product endorsement purposes.

The Advanced Biological and Environmental X-ray Facility (ABEX) is funded by the Director, Office of Science, Office of Biological and Environmental Research. The biological soft X-ray program at the University of California, Davis is funded by the National Institutes of Health under grant # EB001962 to Professor Stephen P. Cramer.

This work was performed under the auspices of the U.S. Department of Energy by University of California, Lawrence Livermore National Laboratory under Contract W-7405-Eng-48.

UCRL-TH-232067

Acknowledgments

For all those who supported, encouraged, cajoled, threatened and pleaded with me. I thank you. By all means this could never be a proper accounting of all those upon whose shoulders I have stood.

I would like to thank Prof. Stephen Cramer, my academic advisor, for providing a challenging project that made me push the superconducting spectrometer to its limits. I owe a great debt of gratitude to Stephan Friedrich for his guidance in both detector development and operation and for keeping me employed. Similarly, Simon George spent many hours rounding out my understanding of biology, chemistry and spectroscopic analysis. Without their help, none of this would exist.

Thank you Simon Labov, for encouraging me to join the group and pursue this research and for your support during many of the difficult bumps I encountered. I am grateful to Prof. Daniel Cox for serving on my dissertation committee. I have Prof. Barbara Neuhauser to thank for starting me on my journey of doing science well and introducing me to the people who would further my career. Dr. Neuhauser has provided me with first-class clean-room experience, low temperature and ultra-high vacuum techniques that have never let me down.

Jan Batteux's assistance in design and fabrication of so many hair-brained ideas involving complicated parts with tight tolerances has been critical in fielding the instrument. Christie Shannon and Kris Petersen provided good cheer, encouragement and most importantly, shielded me from mounds of paperwork.

Elke Arenholz, and Anthony Young are a pleasure to work with. They provided invaluable assistance and training regarding the operation of Beamline 4.0.2.

Thanks to my friends and co-miserators: Pat Castle, who fielded never-ending processing questions, Mark Cunningham, who went before and reported back there was indeed a light at the end of the tunnel, Thomas Niedermayr, Cinthia Piamonteze, Stephane Terracol, Dragos Hau, and Zaheer Ali.

To my family: Throughout my life, my mother's encouragement and my father's threats have trumped all others. My children, Eamonn and Forrest, have provided true motivation and renewed my sense of wonder. Most importantly, thank you Chandra. Despite years of lost weekends and long beam times with early mornings and late evenings, you have remained my supportive and patient wife. Let's go out to dinner.

Contents

1	Introduction	1
1.1	Metals in Biology	1
1.2	Nitrogenase	4
1.3	X-Ray Absorption Spectroscopy	10
1.4	Other Physical Techniques	18
1.4.1	X-Ray Crystallography	18
1.4.2	Nuclear Magnetic Resonance Spectroscopy	20
1.4.3	Electron Paramagnetic Resonance Spectroscopy	21
1.4.4	Mössbauer Spectroscopy	22
1.4.5	Vibrational Spectroscopy	23
1.5	Dissertation Overview	24
2	Spectrometer Design	26
2.1	Superconductivity	26
2.2	Superconducting Tunnel Junction X-Ray Detectors	34
2.2.1	Operating Principle	34
2.2.2	Statistical Limits to Energy Resolution	38
2.2.3	Superconducting Tunnel Junction Fabrication	41
2.3	Spectrometer	44
2.3.1	ADR Design	44
2.3.2	ADR Fabrication	49
2.3.3	ADR Operation	52
2.4	Spectrometer Characterization	55
2.4.1	STJ Performance	55
2.4.2	Quantification of Spectrometer Sensitivity	65
3	Soft X-Ray Spectroscopy of Nitrogenase	80
3.1	Molybdenum Spectroscopy	84
3.2	Sulfur L-Edge Spectroscopy	96
3.3	Nitrogen Spectroscopy	108
3.4	Iron Spectroscopy	122
4	Summary and Outlook	132
4.1	Summary	132
4.2	Outlook	135
	Appendices	138
A	Analysis Software	138
B	Growth of Paramagnetic FAA Salt Pill	143
C	Cryostat Maintenance	147

List of Figures

1	Zinc Finger Domain (PDB:5ZNF)	2
2	Heme Group (HIC-Up:HEC)	2
3	Iron–Sulfur Cluster (HIC-Up:FS4)	3
4	Soybean Root Nodules	6
5	Nitrogenase P-Cluster	7
6	Nitrogenase Iron-Molybdenum Cofactor	7
7	X-Ray Absorption Edge Regions	12
8	L _{2,3} -Edge Features	13
9	Schematic X-Ray Absorption Experiment	14
10	Electromagnetic Spectrum	19
11	BCS Temperature Dependence of Δ	28
12	Magnetic Flux Vortices in Thin Film Superconductors	29
13	Quasiparticle Density of States	30
14	NIN Tunnel Junction Tunneling Diagram	31
15	NIS Tunnel Junction Tunneling Diagram	32
16	SIS Tunnel Junction Tunneling Diagram	33
17	Band diagram of STJ With Schematic Quasiparticle Flow	35
18	Plot of Quasiparticle Tunneling and Inelastic Scattering Time vs Energy	38
19	Quantum Efficiency for Niobium, Tantalum, and Lead	42
20	Schematic Cross Section of STJ	44
21	Schematic Diagram of ADR	45
22	Photograph of STJ detector array on cold finger	45
23	Entropy vs Temperature of FAA	48
24	Heat Switch Diagram	48
25	IR Filter Transmissivity	50
26	Photograph of the Low Temperature Sub-Unit	51
27	Photograph of FAA crystal growth	52
28	I – V characteristic for STJ	54
29	Single Pixel XRF Spectrum of Hydrogenase	56
30	Monochromatic X-Ray Response	58
31	Relative Layer Absorption vs Energy	59
32	Energy Resolution vs Count Rate	60
33	STJ Response Function Position Dependence	61
34	Surface Layer Artifact Analysis	63
35	9-Channel Array XRF of Hydrogenase	65
36	S/N Ratio vs. Energy Resolution	68
37	S/N Ratio vs. Rate	69
38	S/N Ratio vs. Detection Efficiency	70
39	Sensitivity vs. Detection Efficiency	71
40	Sensitivity vs. Acquisition Time	72
41	Spectrometer comparison	75
42	Limiting S/N ratio for L-Edge XAS	77
43	Element Targets of FeMo-co Spectroscopy	82

44	Molybdenum KLM-Edge Comparison	85
45	Chemical Sensitivity of Different Edges	87
46	Mo Model Compound M _{2,3} -Edge Spectra	89
47	Mo M ₃ -Edge Shift Comparison	90
48	Mo Model Compound M _{4,5} -Edge Spectra	91
49	Mo M ₅ -Edge Shift Comparison.	92
50	XRF of Various Molybdenum compounds	93
51	FeMo-co and Fe-Mo-N Model XRF Spectra	94
52	Na ₂ MoS ₄ Fluorescence Spectra	98
53	Un-normalized Sulfur L _{2,3} -edges	99
54	Sulfur L _{2,3} -edge Spectrum	100
55	36-Pixel Close-Packed Array STJ Detector	103
56	X-ray Transmission of Aluminum and Palladium	105
57	Infrared Transmission of Aluminum and Palladium	106
58	112-pixel Ta-based STJs	107
59	Calculated FeMo-co N K-edge EXAFS Spectrum	110
60	Diagrams of FeMo-co and [Fe ₆ N(CO) ₁₅] ³⁻	112
61	[PPh ₄] ₃ [Fe ₆ N(CO) ₁₅] N XANES Spectra	113
62	[N(C ₂ H ₅) ₄] ₃ [Fe ₆ N(CO) ₁₅] EXAFS Spectrum	114
63	[PPh ₄] ₃ [Fe ₆ N(CO) ₁₅] Smoothed EXAFS Spectrum With Fourier Transform	115
64	FeMo-co Nitrogen XANES Sample #1 (From NMF Solution)	117
65	FeMo-co Radiation Damage Test	118
66	FeMo-co Nitrogen XANES Sample #2 (From Methanol/Acetone Solution)	119
67	FeMo-co Radiation Damage Test Sample #2	120
68	FeMo-co Nitrogen K-edge Spectra Comparison	121
69	Nitrogen K-edge EXAFS absorption spectrum of FeMo-co	122
70	Iron L-edge Energy shift.	124
71	No Observed Iron L-Edge Radiation Chemistry for FeMo-co	126
72	Average Iron Oxidation State of FeMo-co	127
73	UHV Liquid Sample Holders	129
74	Comparison of Solid and Solution K ₃ Fe(CN) ₆ Absorption Spectra	130
75	Iron absorption spectrum of FeMo-co solution	131
76	Detector Pixel Calibration Window	139
77	Detector Pixel Window Tool	141
78	Detector Pixel Absorption Spectrum Tool	141
79	FAA Salt Pill Skeleton and Mold	144
80	Gold FAA Salt Pill Skeleton	145
81	Dry FAA Salt Pill	145
82	FAA Salt Pill and Stainless Steel can	145
83	Tower Assembly Parts	147
84	Clove Hitch	148
85	4 K and 0.1 K Posts After Attaching Kevlar Strings	148
86	4 K, 1 K and 0.1 K Parts on Alignment Fixture	149
87	Kevlar String Adjustor Knot	149
88	Fully Assembled Towers Ready for Tensioning	150

89	Low-Temperature Assembly and Magnet Shield	151
90	Heat Switch Solenoid Parts	152
91	Heat Switch Assembly	153

List of Tables

1	Spectrometer Comparison	75
2	Calculated Molybdenum M-edge Radiative and Non-Radiative Yields	86
3	EXAFSPAK Fit Parameters for $[\text{PPh}_4]_3[\text{Fe}_6\text{N}(\text{CO})_{15}]$	115
4	Iron–Sulfur Cluster Properties	123

1 Introduction

1.1 Metals in Biology

Metals play as varied a role in biology as the proteins they are part of. They are involved in structure formation, they help transfer material and information, and they catalyze chemical reactions. Other proteins transport material or information, such as hemoglobin that distributes O_2 and takes up CO_2 , or insulin that signals cells to increase glucose uptake in response to high blood glucose levels. Again other proteins promote chemical reactions, such as photosystem II responsible for photosynthetic oxygen evolution or nitrogenase which catalyzes the reduction of N_2 to NH_3 . All of these proteins require the presence of a metal ion for their activity.

Often the metal ion is a transition metal, their partially-filled *d*-shells can be oxidized and reduced easily, and they can bind to different ligands in different configurations. The roles transition metals play in protein function mirror those of the proteins themselves, and include structure formation, catalysis, storage and transport. By virtue of a metal's ability to fulfill more than one of these roles, their integration has become critical to protein function. For example, many protein–DNA interactions require the protein to form a structure that fits into one of the grooves of a nucleic acid helix, and zinc binds to a short section of the amino acid chain to help position a small helix that can bind to a specific nucleic acid sequence (Figure 1). Here the zinc ion plays only a structural role. In other contexts zinc is found in nucleic acid polymerases and transcription factors where it provides osmotic balance and facilitates nerve impulses by serving as a charge carrier. Transition metals also function to bind to dioxygen during transport, where it is important that the O–O bond is

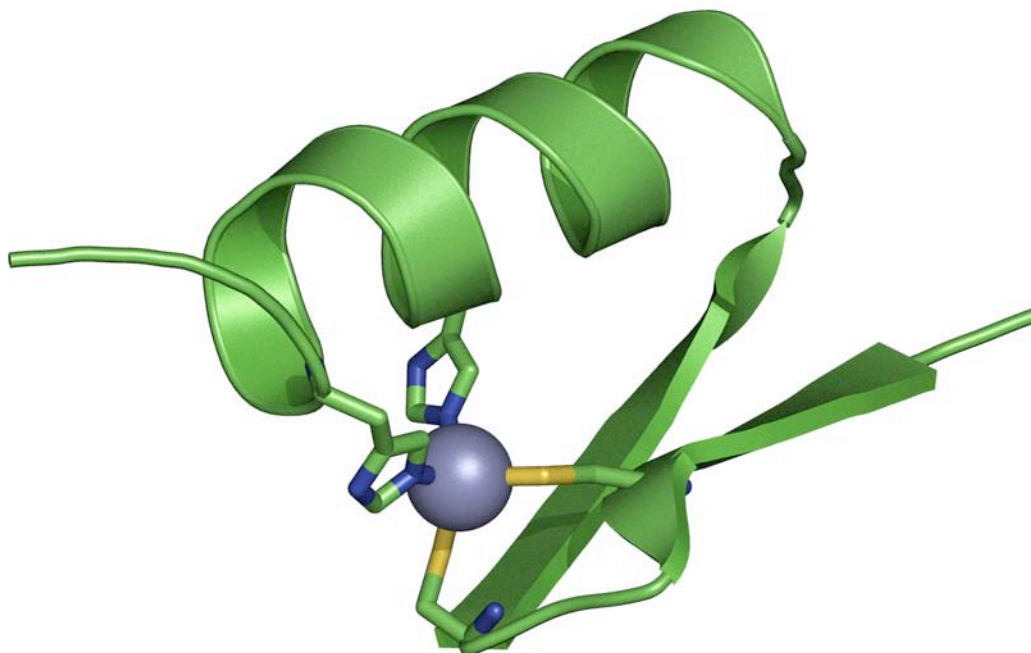


Figure 1: Zinc finger domain from a human enhancer protein. [Kochoyan 91, PDB:5ZNF] Shown here are the common elements of an anti-parallel β -sheet and α -helix held in position by a zinc ion.

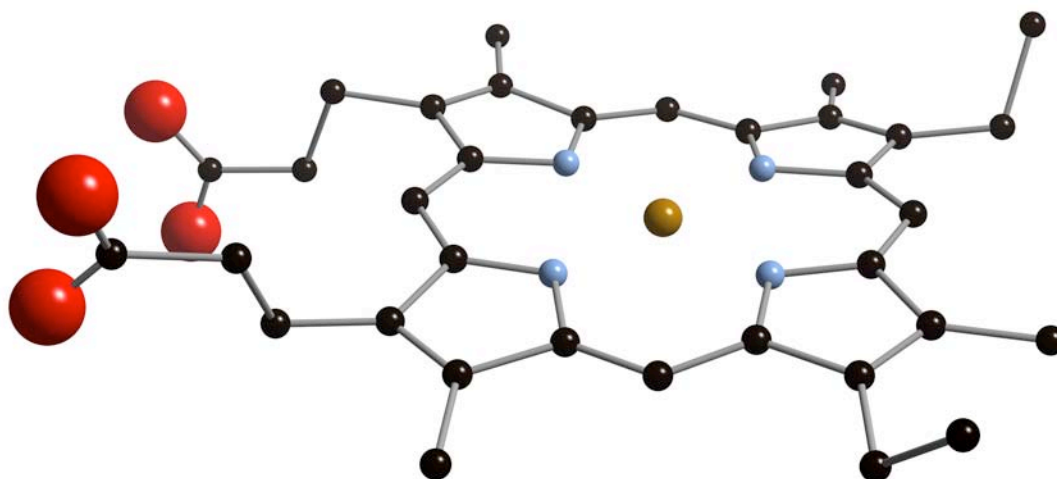


Figure 2: A heme is a prosthetic group that consists of an iron atom in the center of a porphyrin ring. They are typically involved in electron and diatomic gas transfer. [HEC 06, HIC-Up:HEC]

not irreversibly broken, such as the heme functional sub-unit, in which oxygen binds to an iron atom in the center (Figure 2).

Proteins that catalyze redox reactions require the transfer of electrons. These electron exchanges are often handled by iron–sulfur clusters incorporated into such proteins for this purpose. A common iron–sulfur cluster (Fe_4S_4) structure is shown in Figure 3. These structures have de-localized electron states that stabilize the cluster over a range

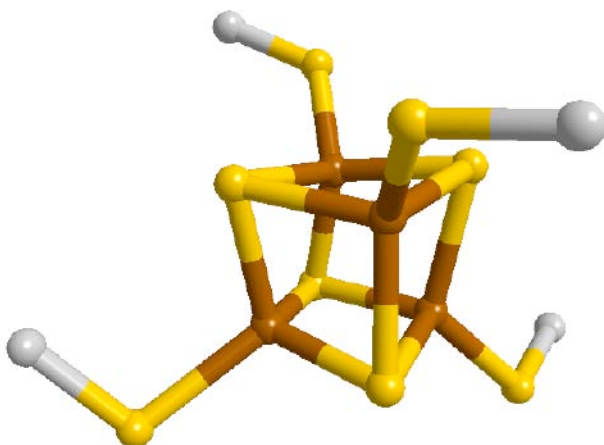


Figure 3: Fe_4S_4 Iron–Sulfur cluster. In addition to the three sulfur atoms (yellow) shown, each iron atom (rust) is usually coordinated to a fourth sulfur atom on a cysteine side chain. [FS4 06, HIC-Up:FS4]

of oxidation states while making the payload electrons more accessible to the exchange pathway. Iron–sulfur clusters are found in many proteins with varying functions across different species.

The roles of metals in biology are the subject of many investigations. Aside from a purely scientific interest in fundamental chemical reactions in biology, there is considerable commercial interest in understanding the mechanisms of biological catalysis. Nitrogen fixation, for example, which requires breaking the triple bond of N_2 , is done industrially under the costly conditions of high temperature and pressure, whereas there are bacteria that can catalyze the same reaction under ambient conditions. As another example, hydrogenase is a protein capable of evolving molecular hydrogen using only iron and nickel metals at the active site, a process of considerable interest for a potential future hydrogen economy given that the majority of industrial hydrogen production currently uses natural gas in a process

called steam reformation which releases CO_2 into the environment [Crabtree 04]. The molecular mechanisms underlying the biological catalytic function, such as the reduction in activation energy at the active site of metalloenzymes, are therefore subject to widespread scientific study.

The study of the metal sites in proteins and their role in the reaction mechanism typically involves questions regarding the state of the metal and its neighbors. What is the ligand environment? What is the coordination number and geometry? What oxidation states do the metals in the active site go through in the course of a catalytic cycle as different substrates bind to it? What happens to the electrons? The goal is to learn as much about the active site throughout the reaction as possible to elucidate the reaction mechanism. Answering these questions poses numerous challenges and requires many complementary analytical techniques. The most common ones will be discussed in sections 1.3 and 1.4.

1.2 Nitrogenase

Despite the fact that nitrogen is by far the most abundant element in the air, the availability of this element is usually the limiting factor in plant growth. The reason for this is the relative inertness of the triply bonded dinitrogen molecule N_2 and the associated inability of most living organisms to oxidize or reduce it. Although the conversion of dinitrogen to ammonia is an exothermic reaction, the high bond dissociation energy of $\sim 10\text{ eV}$ makes it an energetically expensive and therefore slow process. It also means that the enzyme responsible for nitrogen fixation often comprises 2%–5% of cell protein, and bacteria can spend up to 40% of their total energy on nitrogen fixation. Biological nitrogen fixation is

limited to bacteria and archaea, which recycle approximately 10^{11} kg of nitrogen globally per year, roughly equivalent to the abiotic contribution to nitrogen fixation [Schrock 06]. Which makes these microorganisms key elements of the global nitrogen cycle.

Industrially, ammonia is produced through the Haber–Bosch process, which requires high temperatures of ~ 400 °C and pressures ~ 200 atm. Greater than 1% of the energy consumed by humans goes toward the Haber–Bosch process [Schrock 06]. Since industrially-produced ammonia is a key ingredient in fertilizers, its manufacture directly affects agricultural productivity. From an economic point of view, there is therefore considerable interest in understanding the mechanism of natural nitrogen fixation.

Nitrogen-fixing microorganisms are common in many natural environments. For instance, *Azotobacter vinelandii* and *Clostridium pasteurianum* are found in the soil, cyanobacteria live in the ocean, and bacteria of the genus *Rhizobium* live symbiotically in the root-nodules of leguminous plants (Figure 4).

In all of these organisms, nitrogen fixation is carried out by a metalloenzyme complex called nitrogenase. Several classes of nitrogenases have been identified in different organisms, whose active sites contain iron–sulfur clusters and additional molybdenum, vanadium or iron atoms. Among these classes, the molybdenum-dependent enzymes are by far the most common and best studied [Burgess 96]. These enzymes consist of two components, an iron protein homodimer called the Fe-protein, and a molybdenum–iron protein heterodimer called the MoFe-protein, which cooperate to catalyze the reduction of dinitrogen to ammonia. The Fe-protein contains a single [4Fe-4S] cluster that serves as a carrier of electronic charge to the active site of nitrogenase. During a catalytic cycle, this Fe-protein associates and dissociates from the MoFe-protein several times, each time



Figure 4: Root nodules of soybeans harbor nitrogen-fixing bacteria that form a symbiotic relationship with the host plant.

delivering an electron from its $[4\text{Fe-4S}]$ cluster to the MoFe-protein in a reaction that is dependent on the hydrolysis of MgATP [Burgess 96]. Each independently operating $\alpha\beta$ subunit of the MoFe-protein contains two types of metalloclusters: the $[8\text{Fe-7S}]$ so-called P-cluster (Figure 5), which facilitates electron delivery from the Fe-protein to the active-site, and a $[7\text{Fe-9S-Mo}]$ M-cluster (Figure 6) that is the iron–molybdenum cofactor (FeMo-co) where the dinitrogen molecules are reduced. Interestingly, in addition to N_2 , the nitrogenase enzyme also catalyzes the reduction of other molecules with triple bonds. In all cases, the catalysis is accompanied by hydrogen evolution and the consumption of the energy source MgATP. For dinitrogen, this gives a limiting stoichiometry of [Burgess 96]



In many bacteria, two or even three nitrogen fixing systems are present in the genome—

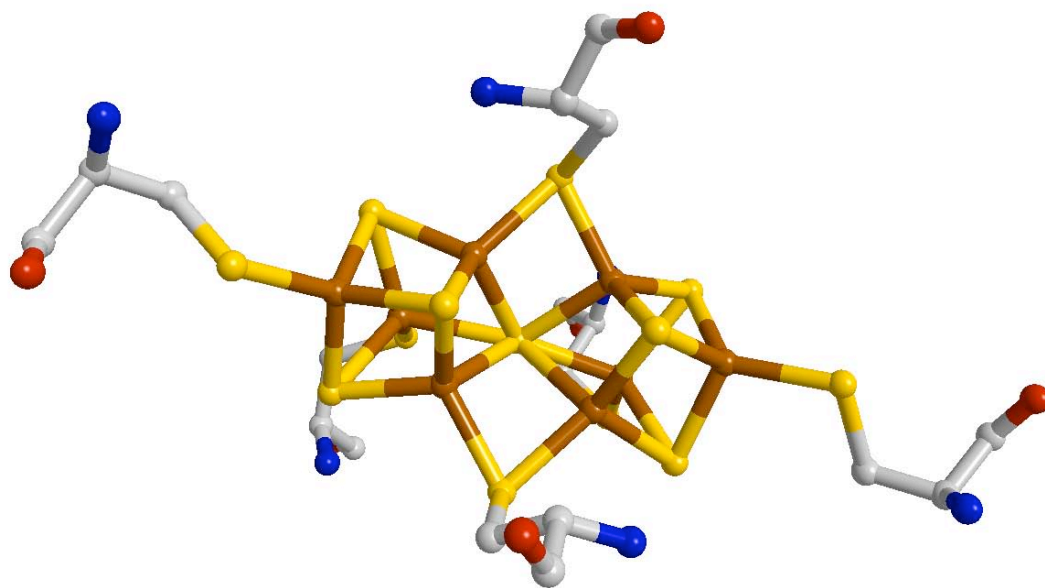


Figure 5: Nitrogenase P-cluster located in the MoFe-protein of nitrogenase in the dithionite reduced form [Einsle 02, PDB:1M1N]. The cysteine ligands are shown; completing the iron–sulfur coordination.

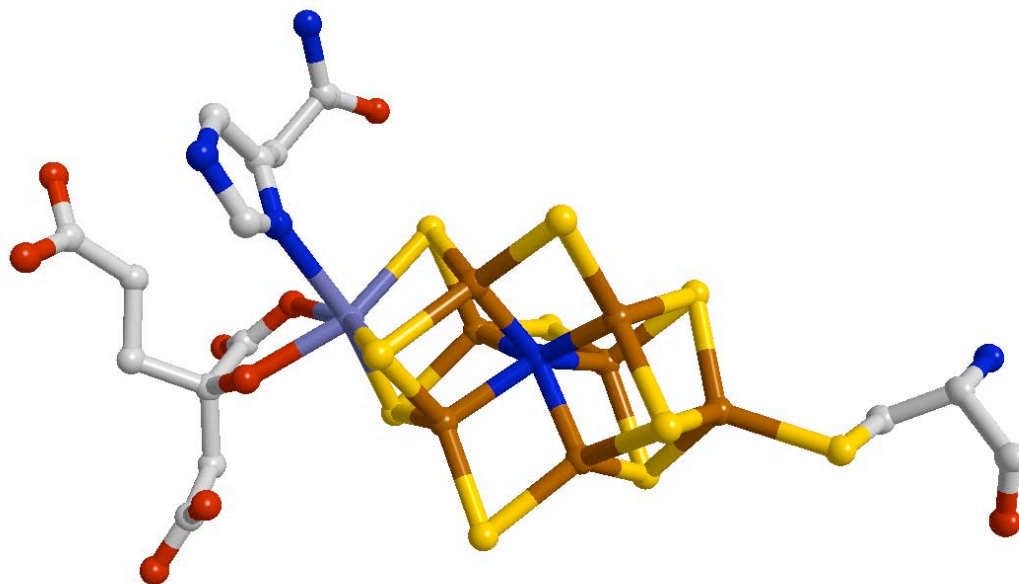


Figure 6: The iron–molybdenum cofactor is shown with the proposed interstitial nitrogen in the dithionite reduced form [Einsle 02, PDB:1M1N]. On the left are the homocitrate and histidine ligands attached to the molybdenum which is in turn bonded to an unusual iron–sulfur cluster. On the right is the cysteine ligand.

the conventional MoFe enzyme together with alternative nitrogenases [Bishop 86] that contain vanadium–iron (VFe) or all-Fe cofactors [Eady 96]. VFe and all-Fe nitrogenases are expressed under low Mo conditions, and they show interesting differences in substrate specificity from the conventional nitrogenases. These form of nitrogenase are not further discussed in this dissertation.

There has been a major effort to understand the mechanism of MoFe nitrogenase from the viewpoints of biochemistry and molecular biology as well as through modeling using inorganic chemistry, both because of its fundamental scientific importance and because of its possible ramification for industrial nitrogen fixation and fertilizer production. These studies have generated a wealth of spectroscopic, kinetic and genetic data leading to much discussion about the mechanism.

The first crystal structure for the *Azotobacter vinelandii* MoFe-protein [Kim 92] was a turning point for nitrogen fixation research, since for the first time mechanistic hypotheses could be based on a firm molecular structure. The protein structure revealed a molybdenum atom at one end of the M-cluster, bound on one side by histidine and homocitrate ligands, and bridged on the other side to three iron atoms through three sulfide ligands. This first set of irons was in turn bridged through sulfide ligands to another iron triangle, followed by a final layer of three sulfides and a terminal iron at the other end of the cluster. The problem was that the mechanism and even the N₂ binding site are not obvious from simple inspection of the M-center structure [Kim 92, Bolin 93, Mayer 99]. Also, the presence of six “trigonal” Fe was a surprise to chemists, many of whom then invoked these under-coordinated metals in the catalytic mechanism [Deng 93]. This trigonal Fe structure was subsequently reproduced in a *Clostridium pasteurianum* MoFe-protein structure at 3 Å

resolution [Kim 93], and a later *Klebsiella pneumoniae* structure at 1.6 Å [Mayer 99].

From 1.16 Å resolution diffraction data, Rees and coworkers have recently proposed the existence of a central light atom (C, N, O), six-fold coordinated by Fe in the center of the 6-Fe cage [Einsle 02]. The appearance of this interstitial atom in the M-center astonished the nitrogenase community. Subsequent density-functional theory calculations suggest nitrogen, but cannot exclude carbon or oxygen, as the central atom leading to a geometrically favorable structure [Hinnemann 03, Dance 03]. Given the previous general acceptance of the “empty cage” M-center structure, and the frequent invocation of trigonal Fe to explain the reactivity of nitrogenase, chemists are still digesting the replacement of a “well-defined cleft” by a “central ligand...most likely nitrogen” [Hinnemann 03]. Using ENDOR and ESEEM spectroscopy (cf. section 1.4.3), and comparing enzyme turned over under $^{14}\text{N}_2$ vs $^{15}\text{N}_2$, Hoffman’s group found no change in any of the N signals [Lee 97]. They concluded that the central N—if it is there—does not exchange under such conditions. This would certainly be a blow to proposals that argue for this N to be a remnant from N_2 cleavage. Our understanding of the identity and even existence of this central atom would benefit from further inspection.

Apart from the above issues about molecular structure, the electronic structure of the M-center would also benefit from additional study. The M-center can be poised in several different redox levels: $\text{M}_{\text{ox}} \rightarrow \text{M}_{\text{N}} \rightarrow \text{M}_{\text{R}} / \text{M}_{\text{I}}$. The M_{ox} state is obtained by dye-oxidation of the as-isolated form M_{N} , while M_{R} is normally obtained by reduction of M_{N} with the Fe-protein.

This dissertation examines the role that X-ray absorption spectroscopy with our high resolution and (comparably) high efficiency of STJ detectors can play in the soft X-ray

region to examine the chemistry of the FeMo-co and associated model compounds by fluorescence-detected XAS on the low-energy edges of the elements involved in nitrogen fixation. Specifically, section 3.1 discusses the first measurements towards the long-term goal of measuring the molybdenum oxidation state in the MoFe M-center of FeMo-co in different redox levels. The narrow natural linewidths of the molybdenum $M_{4,5}$ and $M_{2,3}$ -edges suggest that these edges will provide more sensitive measures of the molybdenum oxidation state than the higher-energy K and L-edges that have traditionally been used for XAS analysis of FeMo-co, since they should be more sensitive to the subtle chemical and structural changes that FeMo-co undergoes during the catalytic cycle. For studying molybdenum in nitrogenase, this advantage needs to be balanced with the poorer detection limits at the lower energy edges due to their lower fluorescence yield.

1.3 X-Ray Absorption Spectroscopy

X-ray absorption spectroscopy (XAS) involves measuring the change in X-ray absorption cross section as the energy of incident photons is scanned over the binding energy of a sample's core electrons. The X-ray absorption spectrum of a given element consists of a series of edges, each corresponding to excitation of a different core electron. K-edges arise from the innermost $1s$ orbital, L-edges from the second shell, M-edges from the third and N-edges from the fourth. While there is only one K-edge, the lower energy edges are further divided by the angular momentum of the resulting core hole vacancy. There are therefore three L-edges, denoted L_1 , L_2 and L_3 , that correspond to excitation of $2s$, $2p_{1/2}$ and $2p_{3/2}$ core electrons, respectively. Similarly, there are five M-edges and seven N-edges.

These edges are well separated from each other in energy. For the case of iron, for example, the K-edge occurs at ~ 7112 eV, the L_1 -edge at ~ 845 eV, the L_2 and L_3 edges are close together at ~ 720 eV and ~ 707 eV, while the observable M-edges have very low energies of ~ 91 eV and ~ 52 eV.

XAS is extremely useful, because the absorption edges and fluorescence energies are element-specific, and because the detailed structure of the absorption edges is sensitive to the chemical form and ligand environment of the element. Specifically, the formal oxidation state, coordination chemistry, and the distances, coordination number and species of the atoms immediately surrounding the selected element all affect the details of the X-ray absorption spectra. Because of this, XAS provides a relatively simple and practical way to determine the chemical state and local atomic structure in a variety of systems. XAS is routinely used in a wide range of scientific fields, including biology, environmental science, catalysts research, and material science. Crystallinity is not required for XAS, making it one of the few direct structural probes available for non-crystalline materials such as proteins in their natural state. Because X-rays are fairly penetrating in matter, XAS is not inherently surface-sensitive. XAS can be acquired on elements of minority and even trace abundance and gives a unique and direct measurement of chemical and physical state of these elements and systems. This combination of characteristics makes XAS a powerful probe to examine the chemistry of metal ions in the active sites of proteins.

The X-ray absorption edge spectrum is typically divided into two distinct regions (Figure 7). The X-ray absorption near-edge structure (XANES) covers the range within a few 10 eV of the absorption edge and provides a sensitive probe of the electronic properties of a given element, like its formal oxidation state and its coordination chemistry. The

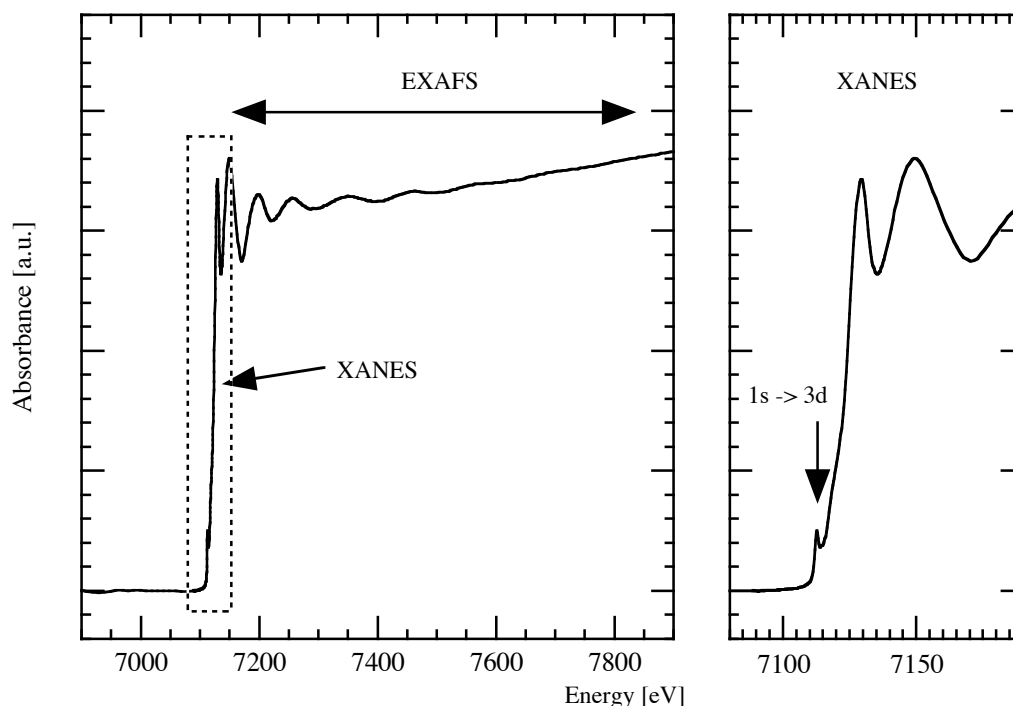


Figure 7: This figure shows the regions of a typical iron X-ray K-edge absorption spectrum.

XANES spectrum is often used as a fingerprint of the chemical species, and its features can often be reproduced quantitatively by ligand field multiplet simulations or density functional theory calculations. The information content of XANES critically depends on the element and edge in question, and in particular whether it contains allowed transitions involving the valence shells. For example, a nitrogen K-edge XAS spectrum will normally contain intense, allowed $1s \rightarrow 2p$ transitions, similarly sulfur K-edge spectroscopy, with allowed $1s \rightarrow 3p$ transitions giving detailed spectra, is well-known as an effective probe of sulfur chemical state. By contrast, the XANES of the iron K-edge exhibits relatively weak bands arising from forbidden $1s \rightarrow 3d$ transitions (Figure 7). To effectively probe the iron electronic structure it is necessary to use lower energy edges such as the $L_{2,3}$ -edges. These involve allowed $2p \rightarrow 3d$ transitions and can produce highly structure spectra where

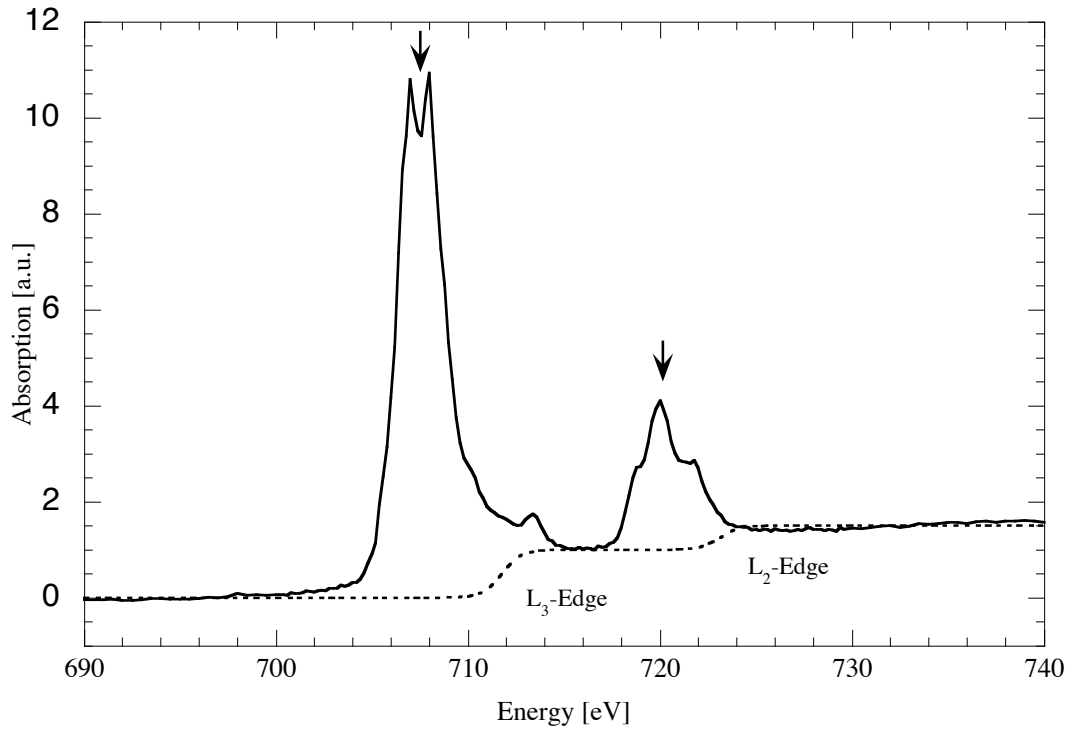


Figure 8: Iron $L_{2,3}$ -edge spectrum. The $L_{2,3}$ -edge jumps are indicated by the dotted line and arrows identify the allowed $2p \rightarrow 3d$ transitions.

the pre-edge transitions are substantially more intense than the corresponding edge-jump (Figure 8). In contrast to the iron K-edge, the iron $L_{2,3}$ -edge spectra readily submit to analysis using multiplet or density functional theoretical approaches.

The extended X-ray absorption fine structure (EXAFS) extends for several hundreds of eV above an absorption edge and is well established as a powerful technique for probing the immediate structural environment of the absorbing element. Quantitative analysis of the EXAFS region yields accurate information regarding number, distances and atomic number of the immediate neighbors of the absorbing atom. Unless crystals are used or multiple scattering effects are present, EXAFS does not normally yield information about relative angles between the absorbing atom and its neighbors.

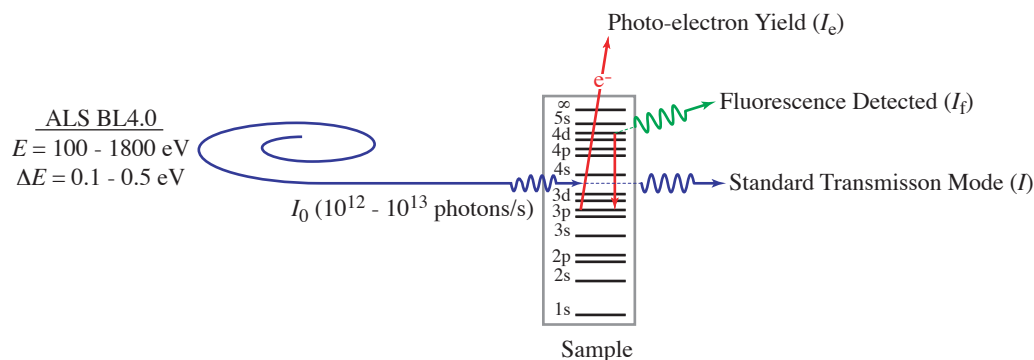


Figure 9: Schematic illustration of an X-ray absorption experiment. In conventional X-ray absorption measurements, there is one incident intensity (I_0), one transmitted intensity (I), and typically a single measured fluorescence (I_f) or electron yield (I_e) intensity.

X-ray absorption measurements depend on the availability of an intense, monochromatic and energy-tunable source of X-rays. In current research, such a source is most commonly provided by a synchrotron facility, and the history and development of XAS closely parallels that of synchrotron radiation. Absorption spectra can be acquired (Figure 9) by measuring the intensity ratio of transmitted to incident beam as a function of energy (transmission mode), or by recording a quantity that is directly proportional to the absorption cross section, i.e. the total electron yield (TEY) or the fluorescence photons associated with the absorption event (partial fluorescence yield, PFY). Metals in enzymes can be probed in all oxidation states and spin states, in dried films or in liquids in different chemically prepared forms. For concentrated samples, TEY is most commonly used, because the experiments only require a simple Channeltron electron detector. For dilute samples like metalloproteins, fluorescence detected XAS offers much higher sensitivity, provided an energy-resolving X-ray detector is used that can separate the fluorescence of the element of interest from incident beam scatter and background fluorescence. By collecting only the fluorescence counts in a narrow energy window around the X-ray

fluorescence of the element of interest, the XAS background can be greatly reduced and the signal-to-noise ratio increased such that the analysis of millimolar protein samples becomes feasible.

XAS experiments are somewhat arbitrarily separated into “hard” and “soft” X-ray energy regions. This separation arises from different technologies necessary to perform an experiment, which in turn depends on the X-ray path length in a given material. X-rays above ~ 2000 eV are considered hard, and experiments in this spectral range are technically straightforward. For example, an iron K-edge transmission measurement at ~ 7 keV uses a crystal monochromator and often comprises a sample held in place with Kapton tape in a 0.5 mm thick Al frame. This is supported in air between an X-ray source and detector. These experiments are comparably simple, and have therefore traditionally been the preferred approach. By contrast, soft X-ray experiments below ~ 2000 eV are technically more involved. An iron L-edge measurement at ~ 700 eV typically uses a grating monochromator and requires an ultra high vacuum (UHV) chamber. Transmission experiments are rare, as the X-ray path length in a solid is of the order of microns. Instead, measurements usually involve monitoring the electron yield or fluorescence concomitant to absorption. The large number and close spacing of emission lines in the soft X-ray band also place much more stringent requirements on the energy resolution of an X-ray detector to separate the fluorescence of interest from the matrix background. The majority of XAS experiments so far performed on dilute materials such as metals in metalloproteins have therefore employed K-edge measurements of XANES and EXAFS in the hard X-ray region.

On the other hand, XAS with soft X-rays, a term used here to describe the energy

range from ~ 50 eV to ~ 2000 eV, offers many advantages. Light elements ($Z < 9$) can only be analyzed with soft X-rays, since the binding energies of their $1s$ electrons are below 1 keV. This includes the biologically relevant elements carbon, nitrogen and oxygen with K-edge absorption energies of ~ 280 eV, ~ 400 eV and ~ 540 eV, respectively. These $1s \rightarrow 2p$ transitions are dipole allowed, show strong dependence on chemical state, and are relatively intense, in contrast to the dipole-forbidden $1s \rightarrow 3d$ transitions at the transition metal K-edges. First-row transition metals have L-edges in the energy range between ~ 400 eV (for scandium) and 1050 eV (for zinc). While hard X-ray K-edge spectroscopy on these elements is possible, the L-edges involve dipole-allowed $2p \rightarrow 3d$ transitions with an intense edge-structure, large chemical shifts, and significantly narrower natural linewidths. This makes them much more sensitive to subtle chemical changes in metal chemistry during the catalytic cycle in metalloproteins. L-edges can be analyzed through theoretical simulations using ligand field multiplet theory, which only require as input parameters the elemental atomic number, its oxidation state, as well as the ligand field symmetry and splitting parameters. In addition, the soft X-ray region covers the M-edges of the second-row transition elements from yttrium (~ 160 eV) to cadmium (~ 770 eV). The $M_{2,3}$ -edges exhibit similar structure as the $L_{2,3}$ -edges, arising from excitation of $3p$ core electrons. The $M_{4,5}$ -edges offer additional information since they are due to transitions out of the $3d$ shell. M-edge linewidths are usually sharper still than L-edges, offering the potential of even greater chemical sensitivity. In the context of bioinorganic chemistry, the molybdenum M-edges at ~ 230 eV and ~ 400 eV are particularly interesting because of the role of molybdenum in several metalloproteins.

Soft X-ray XAS on light element K-edges and transition metal L and M-edges, while

technically challenging, is therefore of considerable interest for the analysis of active sites in proteins. One challenge for XAS with soft X-rays arises from the limitations of current X-ray detectors. The main considerations for good detectors for fluorescence-detected XAS are high solid angle coverage, high quantum efficiency, high energy resolution, and high count-rate capabilities. The solid angle coverage and quantum efficiency are important to capture as much of the available signal as possible, since fluorescence is emitted isotropically. Energy discrimination is important to reject the elastically scattered incident beam and other fluorescence lines, and collect only the intensity of the fluorescence lines of interest, thereby reducing the background intensity and increasing the signal-to-noise ratio. The detector's count rate capabilities need to be high enough to be able to handle the X-ray fluorescence of a modern undulator beam line at a third-generation synchrotron. Of course, ideally such a detector should also be easy to use by non-specialists, and be commercially available at an affordable price.

A common approach in synchrotron science is to use solid-state lithium-drifted silicon (Si(Li)) or high-purity germanium (HPGe) detectors for PFY XAS, which can have an area of 10 mm^2 to 50 mm^2 and thus cover a solid angle of up to 10% when placed close to the sample. These solid-state detectors can achieve an energy resolution of 150 eV full-width at half maximum (FMHM) or better when optimized for soft X-ray operation. They have maximum count rate above 10^5 counts/s per detector element, and are commercially available as multi-element detectors with up to 30 elements. While an energy resolution of 150 eV FWHM or better is impressive, it is not sufficient for many soft X-ray applications, especially when a weak fluorescence signal lies in the wings of a much stronger line such as the oxygen K emission at 525 eV. Also, the highest energy resolution, which is

crucial for many soft X-ray applications, requires long electronic pulse processing times and cannot be achieved at the highest count rate. For an energy resolution below 100 eV FWHM at 525 eV, maximum count rates are typically only a few 10^3 counts/s. This then requires withdrawing the detector from the sample so that the high fluorescence flux does not saturate the detector, and consequently reduces the solid angle coverage. Grating spectrometers, on the other hand, offer extremely high energy resolution below 1 eV FWHM, but their solid angle coverage is typically below 10^{-5} , compounded by an efficiency of only 10%. This makes gratings unsuited for the analysis of dilute metals commonly found in proteins. Despite their drawbacks, the use of solid-state HPGe or Si(Li) detectors is by now fairly common for XAS, especially for dilute and heterogeneous samples and hard XAS, but increasingly also for soft XAS.

1.4 Other Physical Techniques

The characteristic energy levels for atoms provide a tool for probing an atom and its environment. These energy levels can be probed by measuring absorbance, scatter, or fluorescence of electromagnetic radiation. A large portion of the electromagnetic (EM) spectrum is suited to investigating the metal–ligand active site in metalloproteins. Figure 10 shows the spectral range of interest. The most complete characterization requires measurement of as many of the properties as possible.

1.4.1 X-Ray Crystallography

X-Ray crystallography is not a spectroscopic method. It is a technique that yields geometric information. Since hard X-ray wavelengths are on the order of atomic bond distances, they

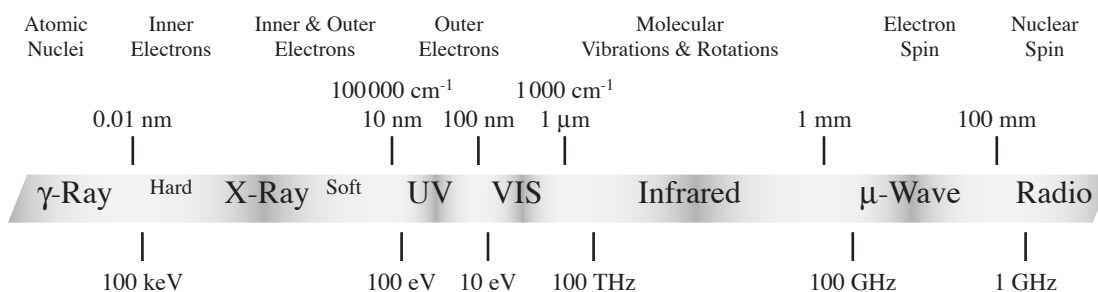


Figure 10: The electromagnetic spectrum showing the range of energies and wavelengths corresponding to atomic and molecular properties commonly studied. This figure relates an atomic or molecular energy level to the corresponding region of the electromagnetic spectrum. The top row shows the physical attribute; the units of cm^{-1} correspond to wavenumber and m correspond to wavelength. Below the bar is the energy associated with the physical attribute.

may be diffracted by the crystal planes of a crystallized sample. The X-ray diffraction pattern from a crystallized protein or sub-unit consists of an array of spots which is analyzed to obtain a map of electron density. For proteins, the electron density and amino acid sequence can be combined to deduce the structure of large protein molecules. The electron density maps can also reveal some chemical information.

Typically, a protein crystal ($\sim 1 \text{ mm}^3$) is placed in an X-ray beam ($\sim 10 \text{ keV}$) from a synchrotron light source. The diffraction pattern is captured by an X-ray CCD camera. The spot intensities are analyzed to determine the three-dimensional structure of the protein.

The spatial resolution is limited by the quality of the crystal, randomly oriented water molecules, and X-ray wavelength. In the case of a protein, the positions can be determined to about 2 \AA . Small molecules, sub-units and co-factors can be determined to less than 1 \AA . Many crystallized proteins retain activity. For such crystals, quenching techniques can provide a method for time resolution and determination of intermediate states.

Crystallization of a protein is the primary limiting factor for structure determination. A good crystallization technique can be extremely elusive for some proteins.

1.4.2 Nuclear Magnetic Resonance Spectroscopy

Nuclear magnetic resonance (NMR) spectroscopy is a technique used to obtain chemical, electronic and structural information about a molecule. At its core, it is a technique for probing atomic bonding based on the Zeeman effect. A magnetic field breaks the degeneracy of the nuclear energy states for those elements with a non-zero nuclear magnetic moment. The non-zero magnetic moment arises from unpaired nucleons. Since the local field each nucleus is exposed to is slightly different due to the magnetic moments of nearby nuclei and electrons, the splittings are also slightly different.

A sample (~ 1 mM, ~ 500 μ L) is placed in an RF (radio frequency) cavity inside a magnetic field (~ 15 T). For ^1H in a 15 T field, there is a 639 MHz resonance corresponding to the splitting. The chemical environment alters the splittings allowing spectroscopic analysis.

Typically, the magnetic field is held constant while the sample is pulsed with a range of RF frequencies of interest. Nuclear spins are aligned, begin to precess and decay back to the equilibrium condition. The precession frequencies produce a decaying signal that is Fourier transformed to produce the spectrum. More complex techniques that take advantage of spin transfer use specific RF pulse trains to study bonded neighbors as well as non-bonded nearest neighbors. Two examples of the continually evolving two-dimensional techniques are correlated spectroscopy (COSY) and nuclear Overhauser spectroscopy (NOESY). COSY probes the spin–spin coupling of bonded nuclei, while NOESY probes the spin–spin

coupling through space of nearest neighbors.

Structural studies of proteins employ NMR spectroscopy on ^1H , ^{13}C , ^{15}N , ^{31}P . One of the strengths of NMR is that the molecule can be in solution unlike crystallography. Kinetics can be studied for time scales longer than ~ 1 s.

1.4.3 Electron Paramagnetic Resonance Spectroscopy

Electron paramagnetic resonance (EPR) spectroscopy is another magnetic resonance technique. It makes use of the magnetic moment arising from unpaired electrons. In organic compounds, unpaired electrons are usually found on free radicals and transition metals.

EPR experiments are usually performed by modulating the magnetic field and holding the RF constant. A free electron in a 0.34 T field will resonate at 9.5 GHz. Note the difference in the frequencies used; the EPR time-scale is quite a bit faster than NMR. The magnetic field required is also smaller which do not require superconducting electromagnets. EPR sample volumes are similar to those of NMR.

Like NMR, there are advanced techniques that enable two-dimensional studies. Two examples are electron–nuclear double resonance (ENDOR) spectroscopy and electron-spin-echo envelope modulation (ESEEM) spectroscopy. ENDOR makes use of the electron-nuclear hyperfine couplings between the unpaired electrons and neighboring nuclei. It is useful for learning about the structure of paramagnetic molecules, as well as information about the distances and orientations of atoms surrounding paramagnetic centers. ESEEM moves into a NMR-like mode where the sample is exposed to an RF pulse. The decay occurs on a smaller time scale.

1.4.4 Mössbauer Spectroscopy

Mössbauer spectroscopy can give very precise information about the chemical, structural, magnetic properties of a material. Nuclear energy levels are influenced by their electronic and magnetic environment which changes or splits these energy levels. Changes in oxidation state shift energy levels (isomer shift δ), and the levels themselves can be split by asymmetry in electronic distribution (quadruple splitting ΔE_Q). Differences in spin states can cause differences in both δ and ΔE_Q since changes in p and d populations changes s screening and overall asymmetric electronic distribution.

A solid sample is exposed to γ -rays from a source element in an excited nuclear state. The γ -rays are absorbed by the element in the sample and a detector measures the intensity of the beam that is transmitted through the sample. The incident γ -ray energy is varied by moving the γ -ray source through a range of velocities. The relative motion between the source and sample results in an energy shift due to the Doppler effect. This technique requires overlap of the emission energy spectrum with the absorption energy spectrum. For the case of low γ -ray energy and samples in a solid matrix, recoilless γ -ray emission and absorption (Mössbauer effect) enables high-quality measurements.

By measuring the absorbance as a function of velocity, a spectrum is measured that shows resonances and splittings which give a measure of δ and ΔE_Q . By cooling a sample below its Curie temperature, magnetic hyperfine interaction splittings can be observed.

1.4.5 Vibrational Spectroscopy

Covalent bonds in molecules are not rigid, but can be stretched and bent. EM waves can interact with the electric and magnetic momenta of the atoms in a molecule and excite various vibration modes. Since an EM wave is a dipole, there are selection rules governing which interactions are strong. The energy associated with molecular vibrations typically lies in infrared (IR) region of the spectrum. To a first approximation the motion in a normal vibration can be described as simple harmonic motion.

Infrared Spectroscopy The vibrational states of a molecule can be probed in a variety of ways. The most direct way is infrared spectroscopy because vibrational transitions typically require an amount of energy that corresponds to the infrared region of the spectrum. This direct absorption requires a molecule with a dipole moment. Infrared light is passed through the sample, and the transmitted beam is measured. This may be done by scanning through the spectrum with a monochromatic beam, or by passing all wavelengths at once and Fourier transforming the result.

The infrared portion of the electromagnetic spectrum is divided into three regions. The far-IR, lying adjacent to the microwave region, has low energy and may be used for rotational spectroscopy. The mid-IR may be used to study the fundamental vibrations and associated rotational-vibrational structure. The higher energy near-IR, lying adjacent to the visible region, can excite higher harmonic vibrations.

Raman Spectroscopy Raman spectroscopy relies on inelastic scattering of monochromatic light. The light interacts with the electron clouds of the bonds in a molecule. The

deformation of the cloud can result in a change in a vibrational mode and the scattering of the photon with an energy shift corresponding to the change in energy of that mode. The energy change corresponds to a vibrational energy level. Transitions that are Raman active occur when the vibrational mode causes a change in the polarizability of the molecule.

Typically, a sample is illuminated with a laser beam. Light from the illuminated spot is sent through a monochromator. Wavelengths close to the laser line are filtered out and those in a certain spectral window away from the laser line are measured.

Resonance Raman Spectroscopy In resonance Raman spectroscopy, the energy of the incoming laser energy is adjusted such that it coincides with an electronic transition of the molecule. The electron is then excited into a higher level and the vibrational modes associated with that particular transition exhibit a greatly increased Raman scattering intensity, while the other modes remain unaffected.

1.5 Dissertation Overview

This dissertation discusses the application of soft X-ray absorption spectroscopy to the enzyme molybdenum nitrogenase. It focusses on the development of a novel type of solid state detector and its application in probing novel X-ray edges namely: molybdenum M-edges; nitrogen K-edges; iron L-edges and sulfur L-edges. These measurements have great potential to resolve several outstanding problems in our understanding of this enzyme. First, the key question of whether the active site iron-molybdenum cofactor includes an interstitial nitrogen atom and whether this atom is exchanged during catalysis. Second, the oxidation states of the molybdenum and iron sites in various isolable states. Third the

role of the sulfur atoms in the electronic structure of the active site cofactor. Soft X-ray spectroscopy has the potential to contribute to all these areas.

Measurement of these soft X-ray edges requires a high sensitivity fluorescence detection with good ($< 15\text{ eV}$) energy resolution and the high efficiency necessary to measure dilute ($\sim 100\text{ ppm}$) samples. The detector described in this work is based on superconducting thin film technology which addresses the limitations of current semiconductor-based detectors for XAS. The superconducting spectrometer offers an order of magnitude improvement in energy resolution over conventional Ge detectors, and thus effectively removes line overlap even in the soft X-ray region for all but the most extreme cases. It has count rate capabilities well over 10^4 counts/s per pixel, sufficient for soft XAS even at a third generation synchrotron. Its main limitation arises from the need for cooling below 0.5 K , and the intrinsically small size of the detector pixels. We have addressed the concerns about refrigeration with the development of a moderately user-friendly refrigerator that holds the superconducting detector at a temperature of $\sim 0.1\text{ K}$ within 10 mm of a room temperature sample inside a UHV chamber at a synchrotron end station. We have addressed the intrinsically small pixel size by developing superconducting detector arrays. We have operated this spectrometer for several years at the Advanced Biological and Environmental X-ray Facility (ABEX) at the Advanced Light Source (ALS) synchrotron in Berkeley, CA.

The first part of this dissertation describes the design, fabrication and characterization of this superconducting solid-state detector. The second part describes its use for the analysis of nitrogenase and related inorganic model compounds at ABEX.

2 Spectrometer Design

2.1 Superconductivity

In 1911, shortly after first succeeding in liquefying helium, Dutch physicist Kamerlingh Onnes observed that the resistivity of mercury suddenly vanished when cooled below 4.2 K [Onnes 11]. Similar observations in tin and lead led him to conclude these metals had undergone a phase transition into a state he called superconducting as the temperature had dropped below a material specific critical temperature T_c . Since then, many other elements, alloys and ceramics have been found to superconduct. Among the elements, niobium has the highest critical temperature at 9.3 K, and critical temperatures of ceramic high temperature superconductors can be well above 100 K.

High currents and magnetic fields were found to destroy superconductivity above a critical field H_c . Typically, H_c is on the order of several hundred Gauss, and scales with T_c . The critical field attains its maximum value $H_c(0)$ at $T = 0$ K and vanishes as $T \rightarrow T_c$.

Meissner and Ochsenfeld observed, in 1931, that superconductors expel all magnetic flux when cooled through the superconducting transition while inside a magnetic field [Meissner 33]. This property of perfect diamagnetism shows that superconductors are more than perfect conductors, since classical electrodynamics predicts that a perfect conductor would trap the magnetic flux present before the onset of superconductivity as opposed to expel it.

F. and H. London proposed a set of equations to phenomenologically describe both the superconducting state and the Meissner effect. Within this model, the magnetic field inside a superconductor is screened exponentially over a characteristic penetration depth λ , which

depends on the number of superconducting electrons [London 35].

In order to explain the thermodynamic properties of superconductors, Gorter and Casimir proposed a two-fluid model of superconductivity in 1934. In this model, there are two classes of conduction electrons, normal electrons and superelectrons [Gorter 34a, Gorter 34b]. These superelectrons would condense into a superfluid where they would exhibit long-range coherence, no entropy and would not scatter as normal electrons do. At $T = 0\text{ K}$, all the electrons would condense into superelectrons, and as $T \rightarrow T_c$ the number of superelectrons would reduce to zero.

Work on microwave absorption in alloys of tin led Pippard to quantify this long-range coherence by introducing a coherence length ξ that characterizes the minimum length scale over which superconductors can change their properties. This coherence length ξ assumes its maximum value ξ_0 for very pure superconductors and is reduced by a finite mean free path due to impurities [Pippard 53].

Up to this point, the theories were purely phenomenological. In 1950, Fröhlich suggested that lattice vibrations could lead to a net attractive force between electrons [Fröhlich 50]. Shortly thereafter, the transition temperatures of isotopes of a particular element were found to be proportional to $M^{-1/2}$, where M is isotopic mass [Maxwell 50, Reynolds 50], suggesting that phonons play an important role in superconductivity. Cooper showed that if there is an attractive force between two electrons, they could lower their energy by forming a bound state [Cooper 56]. The attraction is mediated by an exchange of phonons as suggested by Fröhlich, and the binding is strongest when the two electrons have equal and opposite momentum as well as opposite spins.

In 1957 Bardeen, Cooper, and Schrieffer (BCS) first explained the observations with

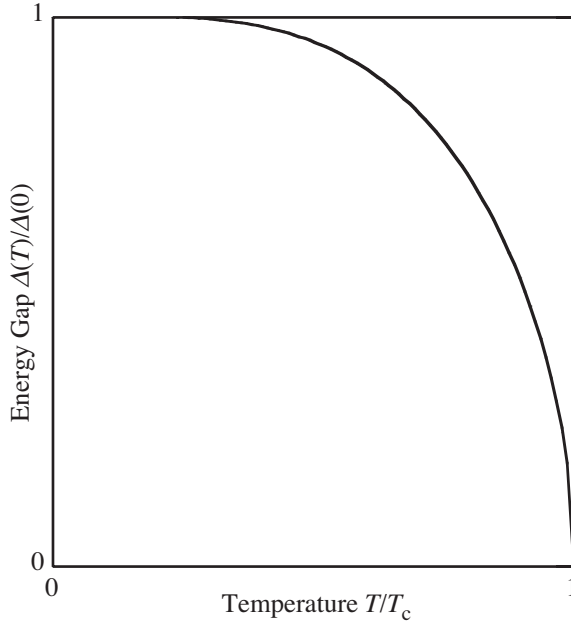


Figure 11: Calculation of the temperature dependence of Δ according to BCS theory. Note that near T_c , $\Delta(T)$ rapidly goes to zero while near $T = 0\text{K}$, it is fairly constant.

a full quantum mechanical treatment [Bardeen 57]. In the superconducting ground state all electrons within the energy range of the attractive interaction about the Fermi energy E_F condense into a macroscopic quantum state formed by overlapping Cooper pairs. The binding energy per electron in a Cooper pair is referred to as Δ and is related to T_c . BCS theory predicts that, in the ground state at $T = 0$, the minimum energy required to break a pair is $2\Delta(0) \approx 3.5kT_c$. Observations yield a range of $(3.0\text{--}4.5)kT_c$, which agrees well with the BCS calculation. It is these Cooper pairs that are the superelectrons previously hypothesized. Pippard's coherence length is thought of as the spatial extension of the Cooper pair wave function. The binding energy Δ changes as a function of temperature, with its maximum value at $T = 0\text{K}$ and reducing to zero as the temperature approaches T_c . A numerical calculation of the temperature dependence of Δ according to the BCS theory is shown in Figure 11.

It turns out that superconductors have fundamentally different magnetic properties

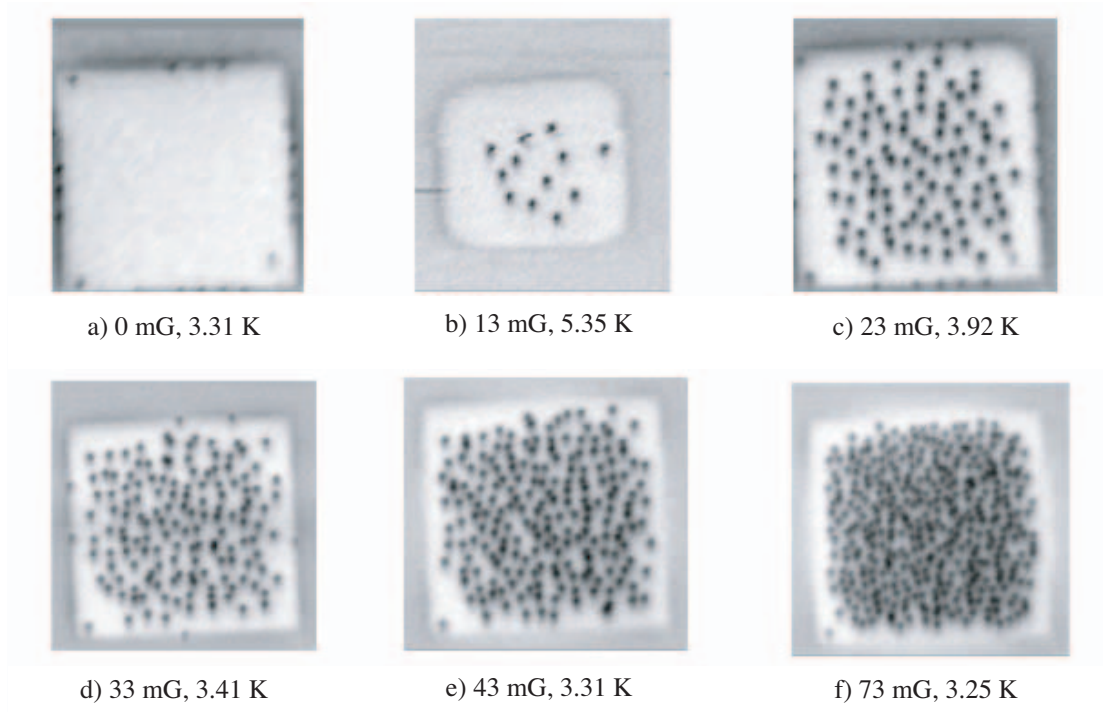


Figure 12: Scanning SQUID micrograph of thin film superconductors with magnetic flux vortices.

depending on the relative sizes of ξ and λ . So-called Type I superconductors, for which $\xi > \sqrt{2}\lambda$, are completely driven normal when $H > H_c$. These are materials with long mean free paths, allowing the Cooper pairs to spread out over micrometer length scales and resulting in uniform electrodynamic properties. In contrast, type II superconductors, for which $\xi < \sqrt{2}\lambda$ do not abruptly lose superconductivity when the external magnetic field exceeds H_c [Abrikosov 57]. Instead the flux is channeled through vortices as shown in Figure 12 [Ohkubo 02], driving that region normal, with each vortex carrying one flux quantum $\Phi_0 = h/2e = 2 \times 10^{-15} \text{ T} \cdot \text{m}^2$. Superconductivity is maintained since there are still regions that have not yet been driven normal. As the magnetic field is increased, more flux vortices are formed, eventually driving the entire superconductor normal. Thin films of type I superconductors are subject to flux penetration only when the thickness is on the

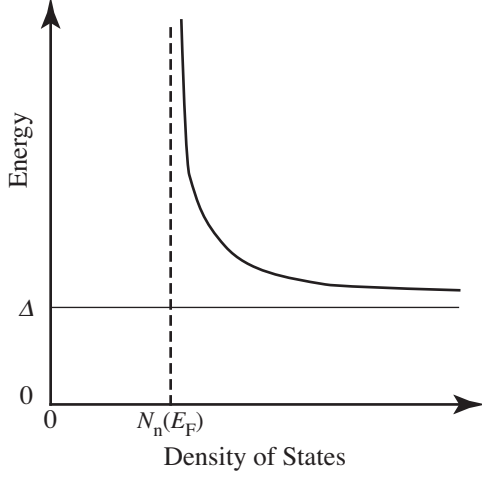


Figure 13: Quasiparticle density of states diagram relative to $E_F = 0$. For $E \gg \Delta$ the density of states approaches its normal metal value $N_n(E_F)$. In this representation, Cooper pairs are located at $E_F = 0$.

order of the bulk coherence length, thereby reducing ξ to a value such that $\xi < \sqrt{2}\lambda$.

In the ground state, the paired electrons occupy a single quantum state with a well-defined phase relation. As the temperature increases, Cooper pairs are broken, that is, the electrons constituting the pair are no longer in coherence. These electrons are called quasiparticles to indicate that they have slightly different properties from regular conduction electrons, such as an increased effective mass and a reduced propagation velocity, but can effectively be considered single particles. A density of states diagram for quasiparticles is shown in Figure 13. There is a gap of magnitude Δ without any allowed states corresponding to the Cooper pair binding energy. Since the number of electrons does not change within the superconducting transition, the electron states with $E < \Delta$ in the normal state now have $E \geq \Delta$, which results in an increased number of states just above Δ . The density of states for superconductivity is given by

$$N_s(E) = \begin{cases} N_n(E_F) \frac{|E - E_F|}{\sqrt{(E - E_F)^2 - \Delta^2}} & \text{for } |E - E_F| > \Delta, \\ 0 & \text{for } |E - E_F| < \Delta. \end{cases} \quad (2)$$

$N_n(E_f)$ is the density of states of this material at the Fermi energy in the normal state.

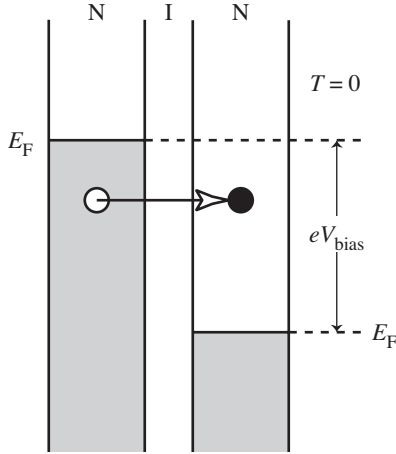


Figure 14: Electron tunneling diagram for a normal-insulator-normal tunnel junction at $T = 0$ K. Density of states is plotted horizontally vs. energy vertically. Shading shows states occupied by electrons. The horizontal arrow indicates allowed tunneling from occupied states into unoccupied states.

The density of states and its occupancy for both normal and superconductors can be examined experimentally using tunnel junctions, devices made of two conductors separated by a thin insulator. If the insulator is thin enough, electrons can tunnel across this barrier whenever occupied states on one side of the barrier face empty available states on the other side. If a bias voltage V_{bias} is applied across the junction, the energies of the conductors are shifted relative to one another by eV_{bias} where e is the electronic charge. As an instructive example, consider a tunnel junction comprised of two normal metals, as shown in Figure 14. The number of electrons on one side with available states on the other side to tunnel into is proportional to the bias voltage, resulting in an Ohmic I - V characteristic with a resistance R_n . Now consider a normal-insulator-superconductor (NIS) junction where one of the electrodes is in the superconducting state (Figure 15). At $T = 0$, the Fermi distribution is a step function in the normal metal, so there is no tunneling current until $V_{\text{bias}} = \Delta/e$, at which point there is a sudden increase in current. With increasing voltage, the tunneling current approaches the Ohmic straight line corresponding to the normal resistance R_n of the junction. In the case of the superconductor-insulator-superconductor (SIS) tunnel junction, no tunneling occurs until $V_{\text{bias}} = 2\Delta/e$, at which point there is a step

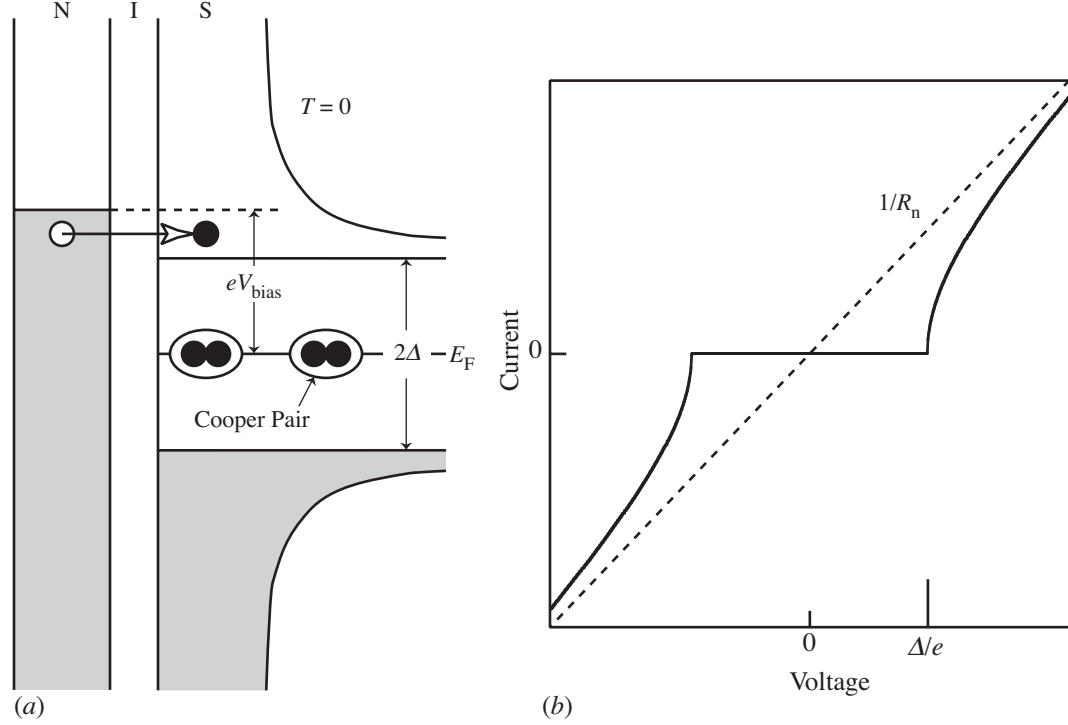


Figure 15: Normal-insulator-superconductor tunnel junction at $T = 0$. (a) Semiconductor model description of electron tunneling for the tunnel junction. The horizontal arrow indicates allowed tunneling. (b) Plot of current vs. voltage. No current flows until the bias voltage exceeds $V_{\text{bias}} = \Delta/e$. The slope of the dashed line shows the normal resistance limit ($1/R_n$).

like current increase. At finite temperatures, thermal broadening of the Fermi distribution broadens the I - V characteristic (Figure 16) [Giaever 60].

In 1962, Josephson predicted that Cooper pairs could also tunnel across the insulating barrier with the same probability. He predicted a DC tunneling current $I = I_c \sin \delta\phi$ at zero bias voltage that depends on the phase difference $\delta\phi$ between the two superconductors due to the coupling of the wavefunctions and assumes its maximum value I_c for $\delta\phi = 0$ (DC Josephson effect). The critical current depends on the geometry of the insulator and the thickness of the tunnel barrier according to

$$I_c R_n = \frac{\pi}{2} \left(\frac{2\Delta}{e} \right). \quad (3)$$

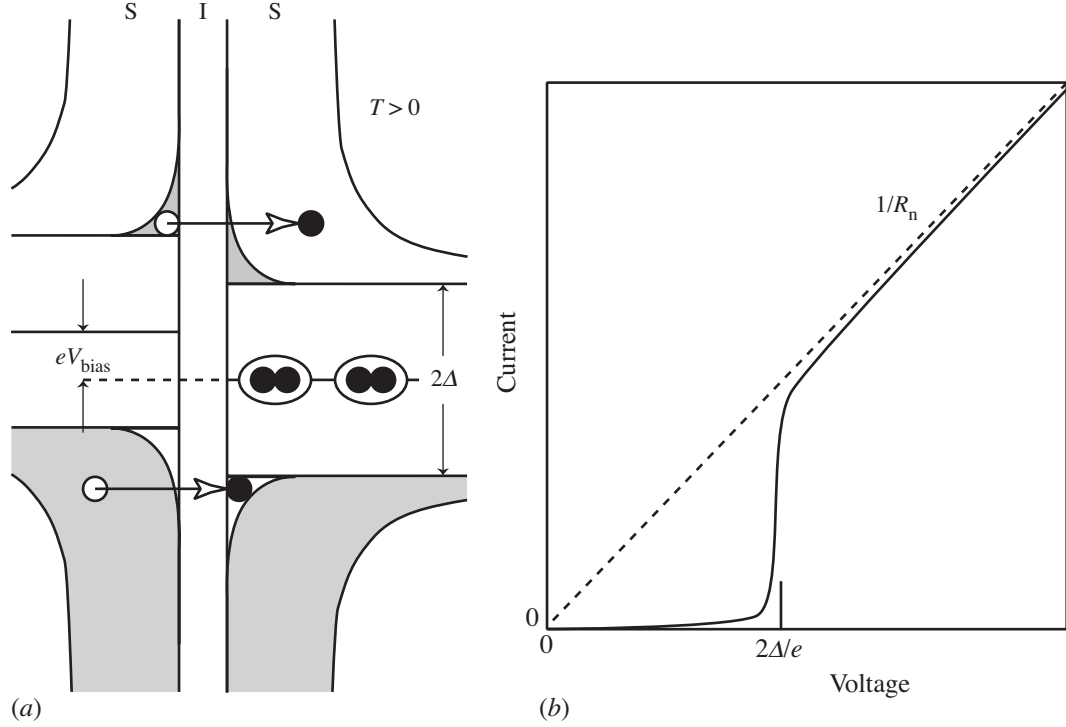


Figure 16: Superconductor-insulator-superconductor tunnel junction at $T > 0$. (a) Semiconductor model description of electron tunneling for the tunnel junction. The horizontal arrows indicate allowed tunneling processes. Thermal energy excites quasiparticles above the gap Δ . In this case they contribute to an exponential tunneling current for $V_{\text{bias}} < \Delta/e$. (b) Plot of current vs. voltage. At $T = 0$, current increases as a step function when $V = 2\Delta/e$. At finite temperature, the excitations reduce the sharpness of the onset of current flow. The slope of the dashed line shows the normal resistance limit ($1/R_n$).

The phase difference varies spatially with magnetic field in the junction plane, and varies temporally with applied voltage across the junction. If a bias voltage is applied, time variations in the phase difference cause the supercurrent to oscillate at a frequency $h\nu = 2eV_{\text{bias}}$ (AC Josephson effect) [Josephson 62]. For each pair that tunnels, a photon of energy $h\nu$ is emitted. This AC Josephson effect has first been measured indirectly through resonances in the DC I - V characteristic excited by the AC Josephson effect in the cavity resonator formed between the junction electrodes (Fiske modes). While the detectors developed as part of this dissertation do not utilize pair tunneling, their performance

is affected by these Fiske mode resonances, which increase the noise and decrease the resolution. If a magnetic field B is applied parallel to the tunnel barrier with a length L perpendicular to the direction of the magnetic field, the phase difference changes linearly with the field along the tunnel barrier. This causes the tunneling current varies spatially across the junction, and causes the critical current and the amplitude of the Fiske mode resonances to vary according to

$$I_c(B) = I_c(0) \left| \frac{\sin(\pi\Phi/\Phi_0)}{(\pi\Phi/\Phi_0)} \right|, \quad (4)$$

where $\Phi = 2\lambda LB$ is the flux through the tunneling region.

2.2 Superconducting Tunnel Junction X-Ray Detectors

2.2.1 Operating Principle

Superconducting tunnel junctions (STJs) can function as X-ray detectors, since photons absorbed in the top electrode can break Cooper pairs and generate excess quasiparticles in proportion to the X-ray energy E_x . These quasiparticles can subsequently be detected as a temporary increase in tunneling current, whose amplitude scales with the number of excess quasiparticles and thus provides a measure of the incident X-ray energy. This section discusses the physics of signal generation and device design of STJ X-ray detectors.

X-ray absorption in the absorber electrode initially creates a single photoelectron, which immediately starts to relax through electron–electron scattering, and thereby distributes its energy among several electrons until their energy is roughly comparable to the maximum phonon energy, also known as the Debye energy E_D . At this point, electron–phonon scattering starts to be the faster and thus the dominant relaxation mechanism,

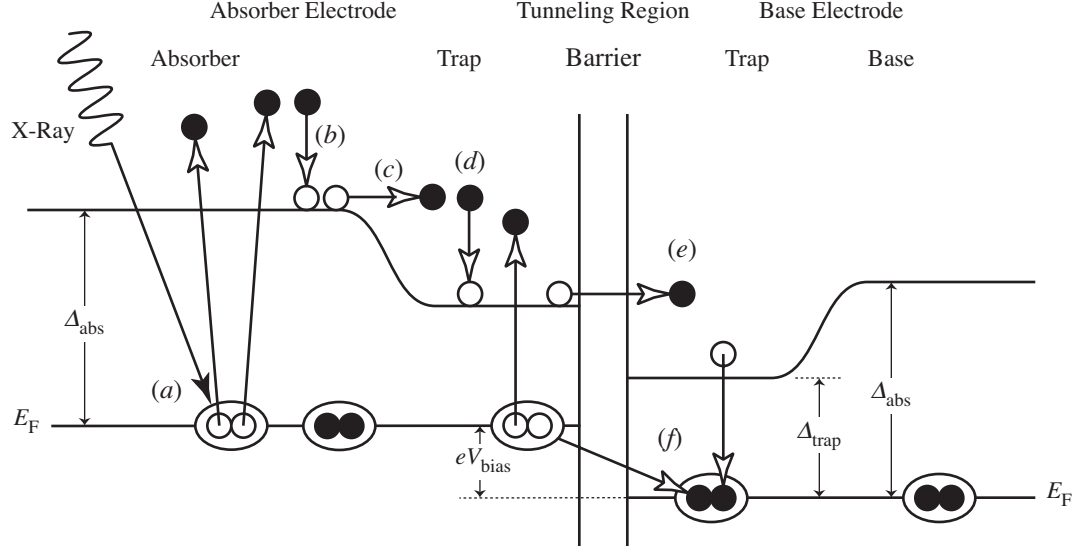


Figure 17: Band diagram of STJ with schematic quasiparticle flow. (a) X-ray absorption generates excess quasiparticles, which (b) consequently relax to $E \approx \Delta_{\text{abs}}$ and (c) diffuse into the low-gap layer, where, (d) they are trapped by inelastic scattering to $E \approx \Delta_{\text{trap}}$. (e) Quasiparticles generate a current signal by tunneling into the base electrode trap and (f) backtunnel to the absorber electrode trap until they eventually recombine and form Cooper pairs again.

leading to the creation of high-energy phonons. These phonons can relax by breaking Cooper pairs until their energy drops below the minimum pair breaking energy of $2\Delta_{\text{abs}}$, at which point their remaining energy is lost to the cold bath. This relaxation cascade occurs within ~ 1 ns after absorption and converts $\sim 60\%$ of the X-ray energy into quasiparticles with energies close to the energy gap Δ_{abs} in the absorber, with the remaining $\sim 40\%$ being converted into sub-gap phonons with $E < 2\Delta_{\text{abs}}$ [Kurakado 82, Rando 92, Zehnder 95]. This means that the average energy ε to create a single excess quasiparticle is given by $\varepsilon \approx 1.7\Delta_{\text{abs}}$ and scales with the energy gap of the absorber [Rando 92]. The total charge $Q = Ne$ created by absorption of an X-ray with energy E_x is therefore given by

$$Q = \frac{eE_x}{\varepsilon} = \frac{eE_x}{1.7\Delta_{\text{abs}}}. \quad (5)$$

High X-ray absorption efficiency requires a thick absorber, whereas fast tunneling

requires a thin electrode. In typical STJ X-ray detectors, these conflicting requirements are satisfied by using two superconducting layers for each electrode, one thick superconductor with a large energy gap Δ_{abs} that acts as the X-ray absorber, and one thin superconductor with a small energy gap Δ_{trap} that acts as a quasiparticle trap. Quasiparticles generated in the absorber diffuse into the thin small-gap region where they are confined (“trapped”) in a region close to the tunnel barrier by inelastic scattering. This bilayer approach allows the separation of the absorption and detection functions of the device, thereby enabling a thick layer for high X-ray absorption efficiency and thin trapping layer for fast tunneling [Booth 87, Kraus 89] (Figure 17). Trapped quasiparticles continue to diffuse throughout the trap, repeatedly impinging upon the insulating barrier until they tunnel across and generate a current signal. The average tunneling time τ_{tun} that it takes a quasiparticle to tunnel therefore depends on the thickness d of the trap, and the barrier transmissivity. Trap thickness sets the frequency with which a quasiparticle impinges on the barrier. Barrier transmissivity sets the likelihood of tunneling each time a quasiparticle hits the barrier, and scales with normal state resistance R_n of the junction. The quasiparticle tunneling time is therefore given by

$$\tau_{\text{tun}} = 4e^2 A d R_n N_n(E_f) \frac{\sqrt{(\Delta + eV_{\text{bias}})^2 - \Delta^2}}{\Delta + eV_{\text{bias}}}, \quad (6)$$

where A is the junction area [de Korte 92]. In the simplest case for which all excess quasiparticles tunnel exactly once across the barrier, the signal current is given by

$$I(t) = \frac{eE_x}{\mathcal{E}\tau_{\text{tun}}} e^{-t/\tau_{\text{tun}}}. \quad (7)$$

Quasiparticles that tunnel from the trap in the absorber electrode to the base electrode (Figure 17e) enter the opposite electrode at an energy at least eV_{bias} above the gap due to

the finite bias voltage. Once they relax to the gap, they cannot directly tunnel back to the absorber electrode since they now face the energy gap of the other electrode. However, if the quasiparticle is prevented from diffusing away from the junction region by a large-gap region in the base electrode, it may still contribute to the tunneling current by breaking a Cooper pair in the *opposite* electrode and pairing with one of the newly unpaired electrons (Figure 17f) [Gray 78]. This backtunneling process moves charge in the *same* direction as direct tunneling, but energy is transferred in the opposite direction. The resulting quasiparticle left in the absorber electrode may then again directly tunnel into the base electrode. Both of these processes occur at the same rate until the quasiparticles ultimately recombine after a characteristic quasiparticle recombination lifetime τ_{rec} . Backtunneling therefore changes the signal waveform to

$$I(t) = \frac{eE_x e^{-t/\tau_{\text{rec}}}}{\mathcal{E} \tau_{\text{tun}}} \quad (8)$$

and results in intrinsic charge amplification equal to the average number of tunneling events per quasiparticle $\langle n \rangle = \tau_{\text{rec}}/\tau_{\text{tun}}$ [Mears 93, Goldie 94].

Note that quasiparticles in either electrode that have not relaxed below $\Delta + eV_{\text{bias}}$ can also tunnel *against* the bias. These reverse processes transfer charge against the bias, and therefore reduce the signal for low voltages by a factor γ given by the fraction of quasiparticles above $\Delta + eV_{\text{bias}}$ in each electrode [Segall 00]. The rates at which tunneling, backtunneling and the reverse processes occur depend on the number of available states to tunnel into and on quasiparticle energy (Figure 18), and are therefore more pronounced for low bias voltages. For example, quasiparticles in aluminum with an energy $\sim 2.5\Delta_{\text{trap}}$ are more likely to scatter inelastically before tunneling, while the opposite is true for

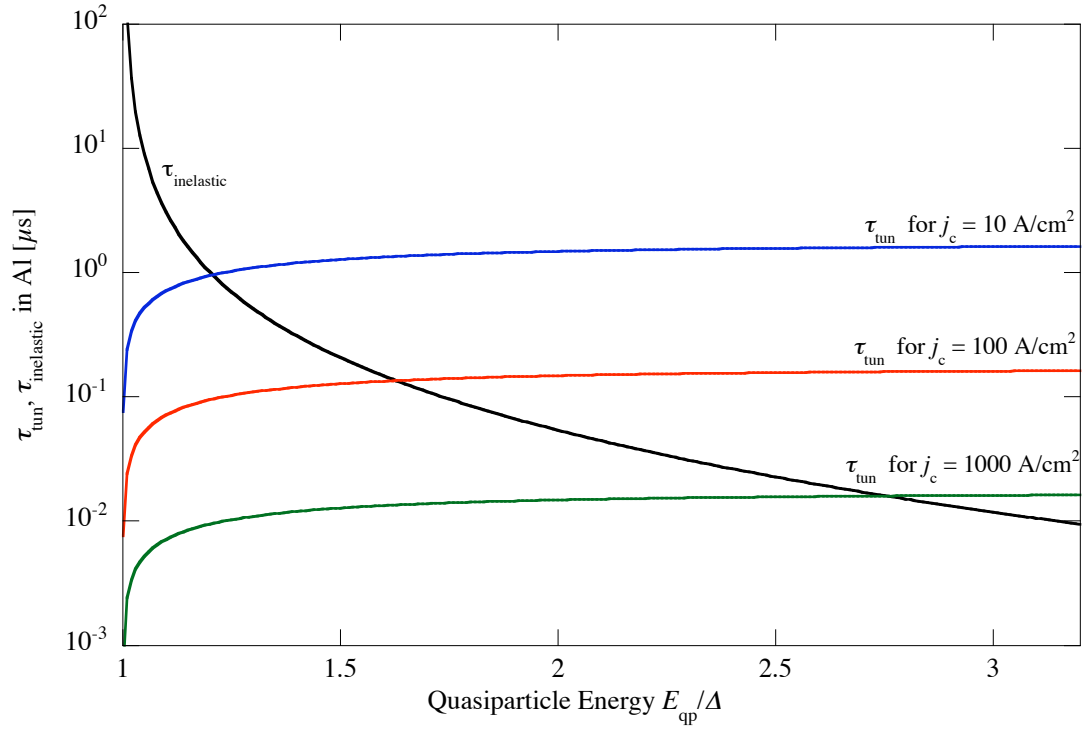


Figure 18: Plot of τ_{tun} and $\tau_{\text{inelastic}}$ vs E_{qp} .

quasiparticles with an energy of $\sim 1.1\Delta_{\text{trap}}$. For full signal charge collection it is therefore important to have a small gap $\Delta_{\text{trap}} \ll \Delta_{\text{abs}}$, and to bias at high voltage.

2.2.2 Statistical Limits to Energy Resolution

The energy resolution of STJ detectors is fundamentally limited only by the statistical fluctuations in charge generation and detection. Due to variations in the partitioning of X-ray energy into quasiparticles and sub-gap phonons, the number of quasiparticles generated by an absorption event fluctuates around its average value $N = E_x/\epsilon$. Since the events that generate quasiparticles are neither identical nor independent, Poisson statistics for which $\Delta N = \sqrt{N}$ do not apply. Instead, the underlying correlations and the attendant reduction in the variance are accounted for by a Fano factor F with $0 \leq F \leq 1$ such that

$\Delta N = \sqrt{FN}$ [Fano 47]. For STJ detectors, the Fano factor has been calculated in Monte Carlo simulations to be $F \approx 0.2$ [Kurakado 82, Rando 92]. The theoretical limit of the energy resolution of an STJ detector, based on quasiparticle generation, is therefore given by

$$\Delta E_{\text{FWHM}} = 2.355 \epsilon \Delta N = 2.355 \sqrt{\epsilon E_x F}, \quad (9)$$

where the factor $2.355 = 2\sqrt{2\ln 2}$ accounts for the conversion of root-mean-square (rms) error to full-width at half-maximum (FWHM).

The average number of tunneling events $\langle n \rangle$ per quasiparticle is also subject to statistical variations. This reduces the attainable energy resolution to [Goldie 94, Mears 93]

$$\Delta E_{\text{FWHM}} = 2.355 \sqrt{\epsilon E_x \left(F + 1 + \frac{1}{\langle n \rangle} \right)}. \quad (10)$$

Backtunneling, therefore not only increases the signal by a factor $\langle n \rangle = \tau_{\text{rec}}/\tau_{\text{tun}}$, but it also reduces the ultimately attainable energy resolution due to the associated variations in $\langle n \rangle$. It is therefore only desirable in devices in which the electronic noise would otherwise limit the performance.

Note that the tunneling processes against the bias not only reduce the signal, but are also subject to statistical fluctuations. This can further reduce the energy resolution according to

$$\Delta E_{\text{FWHM}} = 2.355 \sqrt{\epsilon E_x \left(F + 1 + \frac{1}{\langle n \rangle} + \frac{4\gamma(1-\gamma)}{(1-2\gamma)^2} \right)}, \quad (11)$$

In addition to these fundamental statistical limits, electronic noise of the readout and non-ideal film properties can also degrade the detector performance. For example, quasiparticles that are trapped and recombine in the regions of suppressed gap in the absorber electrode are prevented from tunneling. Such localized regions of suppressed gap

may be present throughout the electrode, either due to flux trapping (Figure 12) oxidation or other chemical contamination. Common areas for local oxidation are grain boundaries as well as the edges and interfaces of the electrode. In addition, the rough edges of the electrode can enhance inelastic phonon scattering and thus increase energy loss to the substrate. Finally, quasiparticles may be lost by diffusion into the electrical contact leads. All these loss mechanisms may have a spatial dependence with respect to the location of the absorption event, and can contribute to peak broadening in the X-ray spectra.

Systematic differences in quasiparticle generation and loss due to recombination can cause additional spectral artifacts. The most significant artifacts are due to X-ray absorption in regions other than the top absorber films, which have a different response function. Since the STJ is a thin film device, there is a finite probability that an X-ray will pass through the absorber layer and be absorbed in the base electrode or in the device substrate. The counter electrode film quality tends to be better than the absorber film quality, because it is protected from oxidation and contamination by the other layers of the junction. The better quality of the base electrode results in fewer quasiparticles lost to recombination in oxide traps compared to absorption events in the top absorber film. This results in an energy dependent line splitting artifact in response to mono-energetic photons, with the X-rays absorbed in the base electrode producing a second spectral line with somewhat higher energy compared to those from the top absorber electrode [Mears 93, for example]. Also, more quasiparticles are created when X-rays are absorbed in trapping layers since $\Delta_{\text{trap}} < \Delta_{\text{abs}}$. In cases where the energy of the X-ray falls in transmissive range for the absorber but not the trap, this effect can be significant [Friedrich 01a].

Finally, absorption events in the substrate produce high-energy phonons, some of

which will move into the base electrode and break Cooper pairs. The signal that such substrate events create depends on the fraction of phonons that are absorbed in the junction electrode and thus on the phonon transmission coefficients between substrate and junction films. Since maximally 50 % of all phonons created in the substrate propagate towards the STJ, and since phonon transmission coefficients are typically no more than 30 %, substrate events tend to cause artifacts located at most six times lower energy than the main line [Friedrich 05].

2.2.3 Superconducting Tunnel Junction Fabrication

Since STJ detectors are thin film devices, their design and performance benefits greatly from technology developed by the semiconductor industry. STJs can be produced photolithographically using well-characterized equipment as long as the materials are compatible with those techniques. Ideally, the absorber should be out of a material with a very high absorption coefficient, with a thickness sufficient to absorb X-Rays over the entire energy of interest with near unity quantum efficiency. Practically, niobium has emerged as the absorber material of choice because a good tunnel junction fabrication processes had already been developed for applications other than X-ray detection. In addition, the absorber thickness is constrained by the increasing film stress due to lattice mismatch between the absorber and the trapping materials. Typically, aluminum is used as a trapping layer because of its small energy gap Δ_{Al} and its high quality native oxide Al_2O_3 . Stress between the layers results in a degradation of detector performance over time and thermal cycling. Figure 19 shows the quantum efficiency of several absorber materials developed for X-ray detection in STJ detectors by different groups.

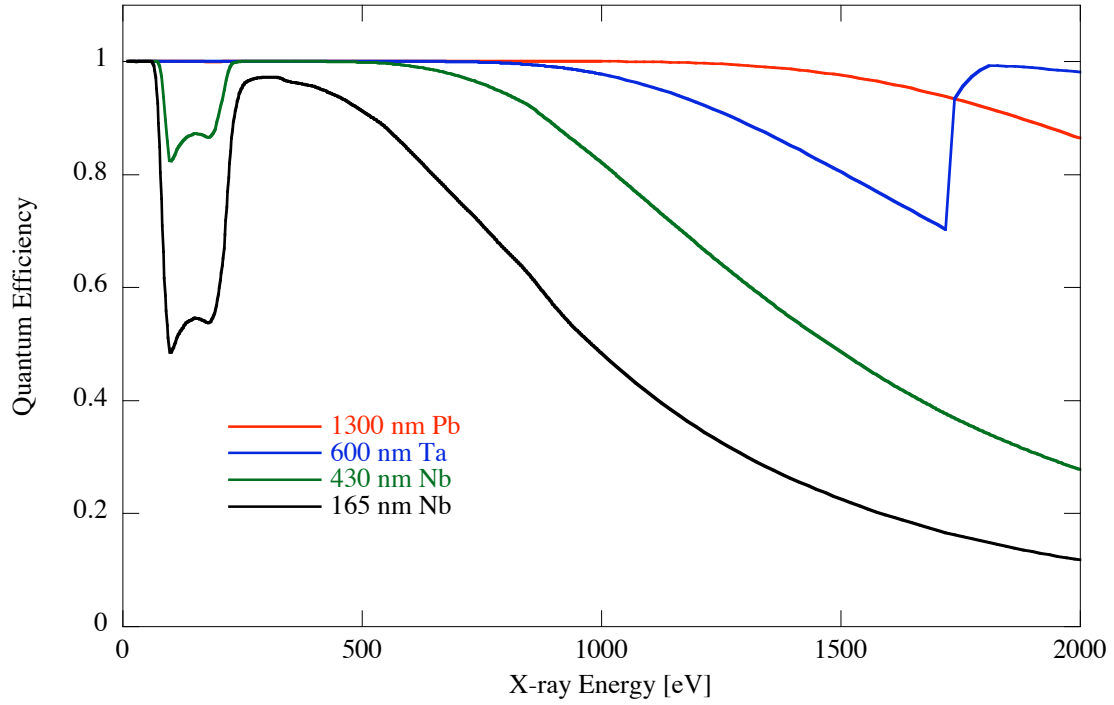


Figure 19: Quantum Efficiency for Niobium, Tantalum, and Lead.

The STJ X-ray detectors developed at Lawrence Livermore National Laboratory were fabricated at Conductus Inc. using a modified version of their standard photolithographic niobium–aluminum trilayer process [Barfknecht 91, Barfknecht 93, Labov 92]. The substrate consists of a 100 mm silicon wafer covered with silicon dioxide grown thermally to a thickness of ~ 200 nm to reduce phonon transmission from substrate events. A 265 nm layer of niobium, followed by a 50 nm layer of aluminum, are sputter-deposited without breaking the vacuum of the deposition system. The tunnel barrier is then formed by moving the wafer to the load lock and exposing it to 10 Torr of oxygen for 30 minutes. This produces reliable high-quality pinhole-free tunnel barriers with a quasiparticle transmissivity corresponding to a critical current density $j_c = 100$ A/cm (Figure 18). Subsequently, another 50 nm of aluminum followed by 165 nm of niobium

are sputter-deposited to form the basic tunneling structure in a single vacuum cycle. While devices with aluminum trapping layers between 50 nm and 200 nm thick have been fabricated, the 50 nm devices are preferred for synchrotron work, since the somewhat larger energy gap Δ_{Al} allows operation of the STJs at temperatures up to ~ 450 mK. All five layers, Nb–Al–Al₂O₃–Al–Nb, are fabricated without ever exposing the wafer to atmosphere in order to minimize unwanted oxidation and contamination of the interfaces and ensure good quasiparticle transmission. The detector pixels are masked, and the top niobium layer is removed by reactive ion etching. The aluminum layers are removed by ion milling. The exposed edges of the active junction area are then passivated by anodization of the side walls in a potassium pentaborate solution. The base electrode wiring is patterned and the unwanted niobium etched away to form the base electrode wiring layer. Subsequently, an 800 nm layer of SiO₂ dielectric is deposited for electrical isolation of the sidewalls using plasma enhanced chemical vapor deposition, and contacts to the absorber electrode are masked and etched. Finally, a 900 nm thick wiring layer of niobium is deposited, patterned and etched. The wiring traces to each junction are 5 μ m wide to reduce quasiparticle loss by diffusion into the detector wiring.

A schematic cross section of the final Nb–Al–Al₂O₃–Al–Nb STJ detector is shown in Figure 20. The 4" wafer contains single pixel devices with areas ranging from 10 μ m \times 10 μ m to 400 μ m \times 400 μ m, as well as 3 \times 3 arrays of 30 μ m \times 30 μ m to 200 μ m \times 200 μ m STJs. For highest energy resolution in the soft X-ray bands comparably small 70 μ m \times 70 μ m and 100 μ m \times 100 μ m are used. These smaller junctions show little resolution degradation due to spatial variations of the detector response or electronic noise. For synchrotron science, where high solid angle coverage is more important than the

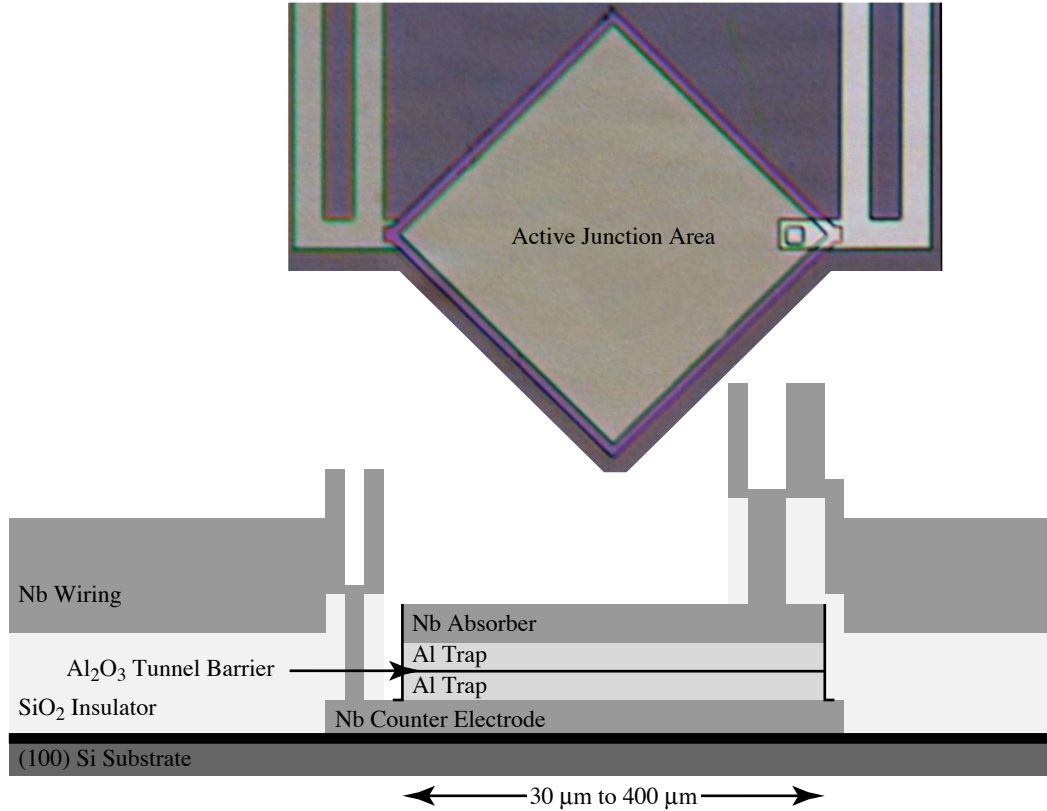


Figure 20: Cross section schematic of STJ with a photograph of a single pixel above.

highest energy resolution, 3×3 arrays of $200 \mu\text{m} \times 200 \mu\text{m}$ STJs were used.

2.3 Spectrometer

2.3.1 ADR Design

To operate STJ detectors in synchrotron-based experiments, the LLNL Advanced Detector Group has developed a two-stage adiabatic demagnetization refrigerator (ADR) with a detector cold finger. Conceptually, the ADR consists of a series of nested shells and stages of decreasing temperature as illustrated in Figure 21. The outer shell (300 K shield) is at room temperature and maintains the vacuum required to insulate the inner stages. The first cold shell (77 K shield) is cooled by a 7.4 L liquid nitrogen tank to $T \approx 77 \text{ K}$. The

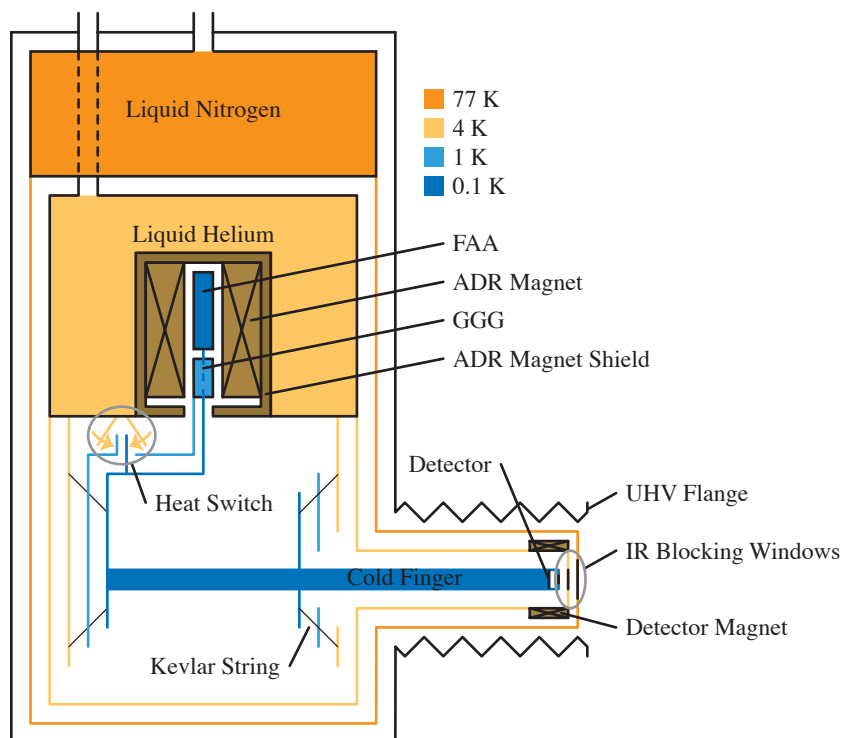


Figure 21: Schematic illustration of the adiabatic demagnetization refrigerator. Figure 22 shows detail of the detector mounted at the end of the cold finger.

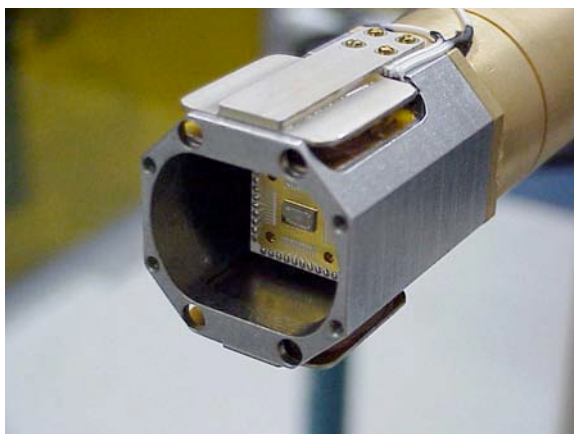


Figure 22: STJ detector array mounted on cold finger with 4 K shield and STJ magnet with the infrared blocking windows removed. In a more recent design, the STJ detector is moved forward for increased solid angle coverage.

next shell (4 K shield) is cooled by a 9.6 L liquid helium tank to $T \approx 4.2$ K. The liquid helium tank has a cavity large enough to accommodate a 5 T superconducting magnet and its Vanadium Permendur (49 % iron, 49 % cobalt, 2 % vanadium) magnetic shielding. High temperature superconducting BSCCO-2212 ($\text{Ba}_2\text{Sr}_2\text{Ca}_1\text{Cu}_2\text{O}_8$, $T_c = 95$ K) leads are used to carry the current between the 77 K and 4 K thermal anchors to reduce the thermal conduction from the nitrogen to the helium and extend the helium hold time. Inside the bore of the magnet there are two paramagnets attached to the two lowest temperature stages, used to reach temperatures below that of a liquid helium bath temperature through magnetic cooling. The paramagnets are chosen based on their ordering temperature which sets the attainable base temperature and heat capacity, which sets the cooling power. The ordering temperature is set by the small dipole interactions, which can be represented by and internal magnetic field, such that kT is on the order of the magnetic energy level splitting in that paramagnet; resulting in a minimum attainable temperature. The heat capacity is related to the spin density of the material [Heer 54]. Gadolinium gallium garnet (GGG, $\text{Gd}_3\text{Ga}_5\text{O}_{12}$) is used for the first stage, since its ordering temperature is ~ 0.7 K, it has good thermal conductivity, is stable under both vacuum and low temperatures, and is commercially available [Fisher 73, Hagmann 94]. Ammonium iron(III) sulfate dodecahydrate ($\text{Fe}(\text{NH}_4)(\text{SO}_4)_2 \cdot 12 \text{H}_2\text{O}$), a paramagnet commonly known as ferric ammonium alum or FAA, was chosen for the second stage paramagnet despite the fact that it is somewhat difficult to work with because of its low thermal conductivity and melting point, since it has an ordering temperature of 25 mK and a high spin density. This two-stage system allows the second stage to attain a base temperature below 0.1 K without pumping on the liquid helium bath, which used to be required to lower its temperature, but introduces

vibrations from the pumping lines.

The first stage (1 K stage) is cooled to ~ 1 K by a 143 g single crystal of paramagnetic GGG. The second stage (0.1 K stage), supported by the first stage, is cooled by 63 g of polycrystalline FAA.

In the first part of the cooling cycle, the paramagnets are isothermally magnetized to lower their entropy (Figure 23), with the heat of magnetization dissipated by a liquid helium bath through a closed heat switch. After opening the heat switch, the magnetic field is decreased sufficiently slowly to prevent heating through loss mechanisms, thereby adiabatically demagnetizing them to lower their temperature. Both paramagnets are magnetically cycled at the same time and dissipate their heat through the same heat switch.

The heat switch used in this ADR to make and break the thermal contact between the two low-temperature stages and the 4 K thermal anchor is a novel electrically-controlled mechanical heat switch. This design avoids air leakage around a sliding, O-ring sealed shaft feed-through found in earlier heat switch designs [Friedrich 01b, van den Berg 03]. It uses an over-center-cam locking mechanism activated by 200 ms 1.5 A current pulses through one of two solenoids that toggle a stainless steel spring between the two stable positions. The heat switch is mounted on 4 K base plate, and provides a force of 1500 N to each of the cold fingers. The jaws of the heat switch are lined with gold-plated oxygen-free high conductivity (OFHC) copper. The jaws clamp fingers on the 1 K and 0.1 K stages providing a link to the 4 K base plate through an OFHC copper braid. Its thermal conductance of 65 mW/K at 4.2 K is set by the thermal conductivity of the braid (Figure 24). This allows the stages to return to liquid helium temperatures ~ 30 minutes after a magnetization,

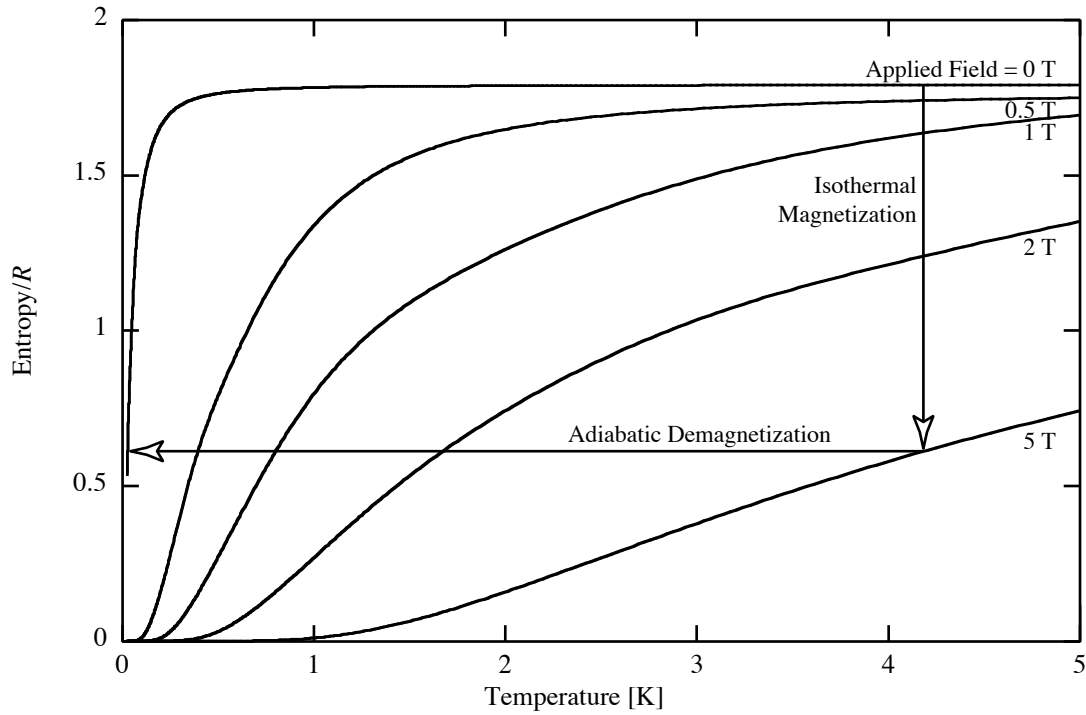


Figure 23: Plot of the entropy of the spin system of FAA normalized by the gas constant vs temperature. Since the ground state of the ferric ion is ${}^6S_{5/2}$, the entropy reaches a maximum value of $S/R = \ln 6$. During isothermal magnetization, excess heat is dissipated by the liquid helium bath. Once thermal equilibrium is reached, the paramagnet is adiabatically demagnetized, isentropically reducing the temperature. [Casimir 39, Hull 41]

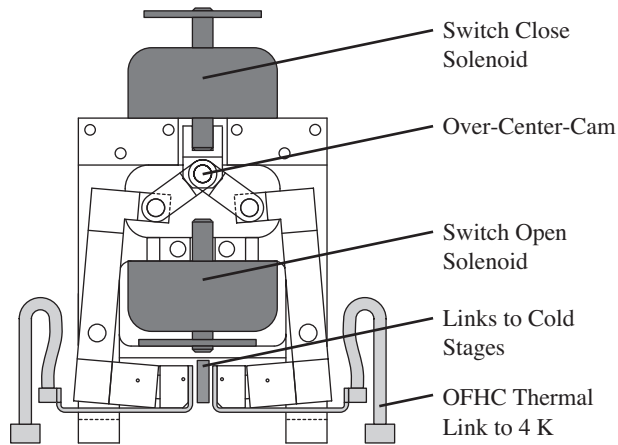


Figure 24: Diagram of the major elements of the heat switch design. The bi-stable over-center-cam is moved by a short current pulse to the appropriate solenoid either releasing or clamping the jaws of the heat switch. The jaws are lined with OFHC copper and connected to the 4 K bath. Thermal links to the 1 K and 0.1 K stages are located between the jaws of the heat switch.

dominating the time required to cycle the ADR.

In order to operate the STJ detector as close to the sample as possible inside an end-station under ultra high vacuum ($\leq 10^{-7}$ Torr), a cold finger is employed to mount the STJ detector array 40 cm from the 300 K cryostat wall. The cold finger consists of a gold-plated OFHC copper rod mounted on the 0.1 K stage. The rod is surrounded by a gold-plated OFHC radiation shield mounted on the liquid helium cooled stage. The 4 K shield also holds the STJ detector magnet needed to suppress the DC Josephson effect, and it is in turn shielded by a gold-plated OFHC radiation shield attached to the liquid nitrogen cooled stage. The 45 mm diameter of the 77 K shield is sufficiently small to enable insertion through standard gate valves. Three infrared (IR) blocking windows prevent room temperature radiation from heating the cold stage and causing IR induced excess noise in the detector. The three windows consist of 200 Å aluminum on 2000 Å parylene on a 95 % transmissive copper grid, and are located in front of the STJ detector on the 77 K shell, 4 K shell and 0.1 K cold finger. The windows are chosen as thin as possible since their transmission limits the spectrometers quantum efficiency at low energy (Figure 25).

2.3.2 ADR Fabrication

The construction of the ADR is based on a model HDL-10 4 K cryostat from Infrared Laboratories [IR Labs 06]. The 300 K shield has a chromate conversion coating, commonly known by commercial names as Alodine and Iridite, which converts the oxide layer at the surface to a corrosion-resistant electrically conductive layer. With this treatment, the outer shell helps to shield the inside of the cryostat from electromagnetic interference (EMI). In addition, all electrical feed-throughs are shielded, and non-signal

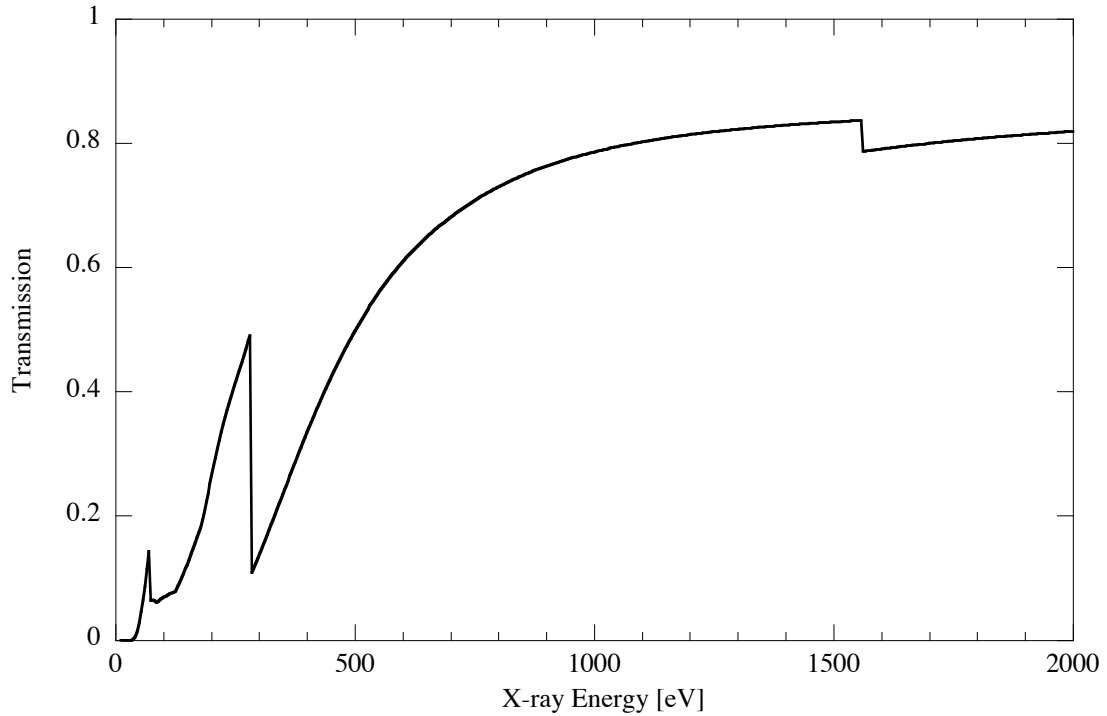


Figure 25: IR filter transmissivity for all three windows. Each window consists of 200 Å aluminum on 2000 Å parylene on a 95 % transmissive copper grid [CXRO 07].

lines are filtered.

The liquid nitrogen tank is suspended from the top plate of the cryostat by three Kel-F tabs and has a thin-wall stainless steel fill tube to reduce thermal conduction between the tank and the top plate. A light-tight aluminum enclosure attached to the tank shields the inner sections from 300 K IR radiation. The liquid helium tank is supported off the liquid nitrogen tank by three Kel-F tabs and has a similar fill tube. Another light-tight aluminum enclosure mounted to the helium tank blocks the 77 K radiation from the coldest stages. Butt joints in the shields require either indium gaskets or epoxy (Emerson & Cuming STYCAST 2850 FT), loaded with graphite to reduce transmission of long wavelength IR.

The thermally isolated stages (1 K and 0.1 K) form a low temperature subunit of the

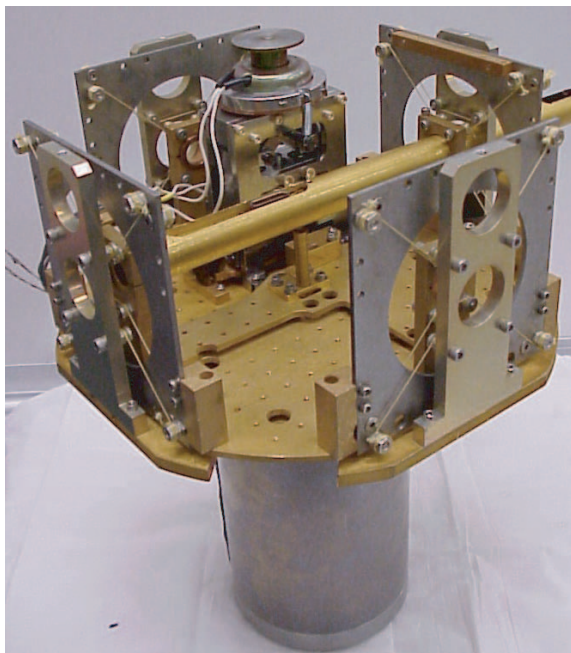


Figure 26: Photograph of the isolated stages sub-unit. The lowest temperature stages are supported by four towers using Kevlar strings. The cold finger in the center is clamped to the 0.1 K stage with a gold-plated copper anchor mount. The 1 K stage is held by four molybdenum anchor mounts (large squares with a circular hole). The tall aluminum anchor mount is mounted on the 4 K base plate. The heat switch is seen in the back. The base plate is supported by the magnetic shielding with the ADR magnet and two paramagnets inside. The orientation of the sub-unit as pictured is inverted during operation.

cryostat, which is attached to the liquid helium tank and can be easily removed for repair and adjustment. (Figure 26). There are four “towers” which support and isolate the two lowest temperature stages by Kevlar strings (50 lbs. working load) under ~ 35 lbs. tension. The stages are made from gold-plated OFHC copper for good thermal conductivity. The materials of the towers are chosen so that they compensate for the lengthening of Kevlar at low temperatures. The 4 K Kevlar anchors of the towers are made of aluminum, the 0.1 K Kevlar anchors are made of OFHC copper and the intermediate 1 K anchors are made of molybdenum. The sub-unit is designed to allow the towers to be easily exchanged since string tension will degrade over time and lead to misalignment of the 1 K and 0.1 K stages.

The cylindrical GGG crystal is attached to the 1 K stage by an OFHC copper clamp. Since FAA does not have the chemical and physical stability of GGG, a more elaborate mounting scheme is required. Materials that come in contact with the crystal must be selected by their ability to withstand the corrosive FAA. Both stainless steel and gold are

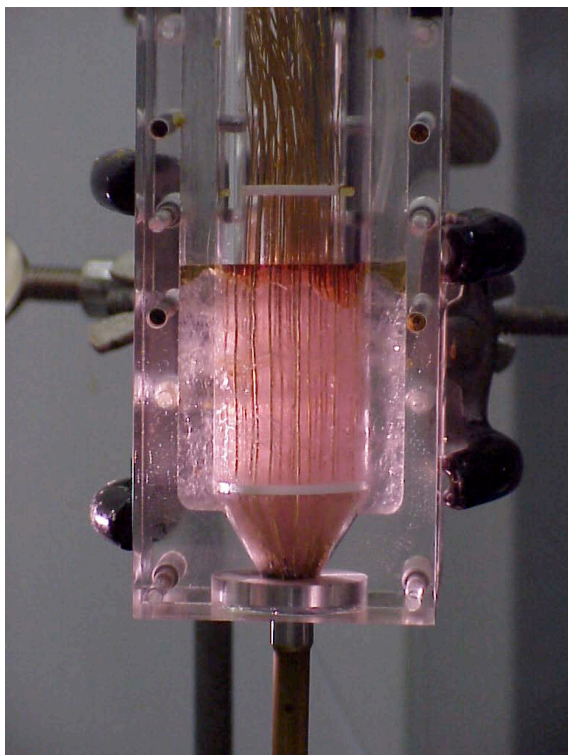


Figure 27: Ferric ammonium alum crystal paramagnet during growth. The crystal is grown around gold wires that assist thermal conduction throughout the crystal. The light pink color is a good indicator of proper crystal hydration for use in an adiabatic demagnetization refrigerator.

appropriate for use with FAA. The FAA paramagnet attached to the 0.1 K stage must be placed inside a vacuum-tight enclosure to prevent dehydration of the crystal. The enclosure is a thin-wall 304 stainless steel tube with welded stainless steel end caps. The polycrystalline FAA is a poor thermal conductor, so entrained gold wires are used to increase conductivity (Figure 27). The wires are separated to prevent energy deposition in the crystal during demagnetization by induced currents. See Appendix B for more construction details.

2.3.3 ADR Operation

To operate the ADR at a UHV end-station, it must first be evacuated at a rate sufficiently slowly to not break the thin IR blocking windows due to the differential pressure between the pumped section and the inner volumes. This is accomplished with a throttle valve

adjusted for a pump-down rate of 0.2 Torr/s at atmospheric pressure. At 1 Torr the rate is further reduced to 0.5 mTorr/s. Below 0.5 Torr the throttle valve can be removed and the pump-down continued to base pressure. Pumping through the gate valve to the UHV chamber for at least 12 h is desirable to reduce the residual gasses that would otherwise freeze out on the IR blocking windows and reduce their transmission.

Both the nitrogen tank and the helium tank are pre-cooled with liquid nitrogen for at least six hours until their temperature has equilibrated close to 77 K. During cool-down, the cold finger is withdrawn from the chamber as far as possible and magnetic shielding is placed around the surrounding bellows to reduce the magnetic field at the location of the junction and thus the amount of flux trapping as the STJ is cooled into the superconducting state. After removing the nitrogen from the helium tank and transferring liquid helium, it takes another six hours until the ADR magnet temperature is sufficiently close to 4 K to avoid quenching during the first demagnetization cycle.

The ADR magnet is energized to a maximum field between 3.5 T and 4.5 T (15 A to 20 A) over a period of ~ 30 minutes, which is sufficiently slow to prevent eddy-currents from heating the magnet above the critical temperature. Note that the current depends exponentially on the applied voltage due to the diodes in the circuit that protect the magnet insulation during a quench. The energized ADR equilibrates to the bath temperature within 30 minutes, with the 1 K stage taking longest due to the large heat capacity of the GGG paramagnet. At this point, the heat switch is opened with a brief 1.5 A current pulse. Wires attached to the 1 K and 0.1 K can be used to confirm that there is no electrically conducting touch between the low temperature stages and ground. The current is then reduced slowly to 0 A and the base temperature equilibrates below 0.1 K. Since the STJ response is not

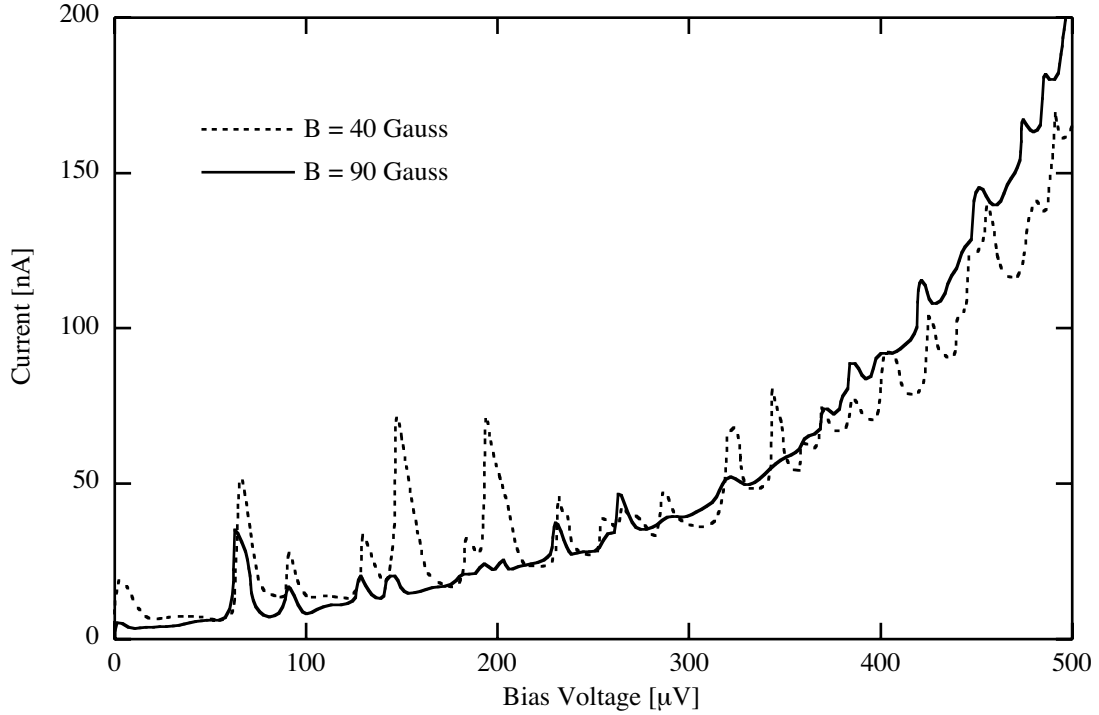


Figure 28: I – V characteristic for a $200\text{ }\mu\text{m} \times 200\text{ }\mu\text{m}$ junction.

temperature dependent as long as there is no thermal contribution to the leakage current, no temperature regulation is necessary and the ADR is allowed to warm up slowly due the heat load into the low temperature stage. For a well shielded stage, the ADR has a hold time ~ 20 h below ~ 450 mK, at which point the increased thermal current starts to cause the detector response to drift and a new de-magnetization cycle is necessary.

A current is applied to the STJ magnet to reduce the amplitude of the DC Josephson current and the Fiske mode resonances to below 20 nA. When the STJ is held in the center of the magnet, a current of ~ 0.4 A is necessary to obtain the required field of ~ 100 G (Figure 28). In the more recent design, where the sensor is moved away from the center and closer to the sample, a current of ~ 0.75 A is necessary. The STJ leakage current exhibits an overall exponential behavior due to SIN type tunneling in regions of trapped flux, with additional narrow peaks at the voltages of the Fiske mode resonances. Note that the signal

increases with increasing bias voltage, since the number of high energy quasiparticles that can tunnel against the bias is reduced. On the other hand, the noise increases with lower dynamic resistance and in the vicinity of Fiske modes. The optimum bias point is therefore between two Fiske modes at the highest voltage where the dynamic resistance is still above $1\text{ k}\Omega$. During operation at the ALS, where no specific magnetic shielding is used, this condition is typically met at a bias voltage of $250\text{ }\mu\text{V}$ or $300\text{ }\mu\text{V}$.

The X-ray induced signals are captured with a current sensitive preamplifier with a gain set by the feedback resistance $R_f = 10^6\text{ V/A}$. For a well biased junction, this produces preamplifier output signals with an amplitude on the order of 100 mV/keV . These signals are further amplified by a spectroscopy main amplifier, whose shaping time of $3\text{ }\mu\text{s}$ to $4\text{ }\mu\text{s}$ is chosen to match the signal decay time. The spectroscopy amplifier has a gain of 150 so that output signals match the range of the subsequent multichannel analyzer (MCA) that captures the signal amplitude. Each STJ pixel has its own separate amplifier/MCA combination and all individual X-Ray spectra are saved to computer.

2.4 Spectrometer Characterization

2.4.1 STJ Performance

The STJ spectrometer performance has been characterized using X-ray fluorescence (XRF) spectra from proteins and model compounds as well as direct illumination with a monochromatic synchrotron X-ray beam. Figure 29 shows the X-ray fluorescence of the metalloprotein hydrogenase, measured with both a $200\text{ }\mu\text{m} \times 200\text{ }\mu\text{m}$ STJ detector and a conventional Ge detector. The energy resolution of the STJ spectrometer is significantly

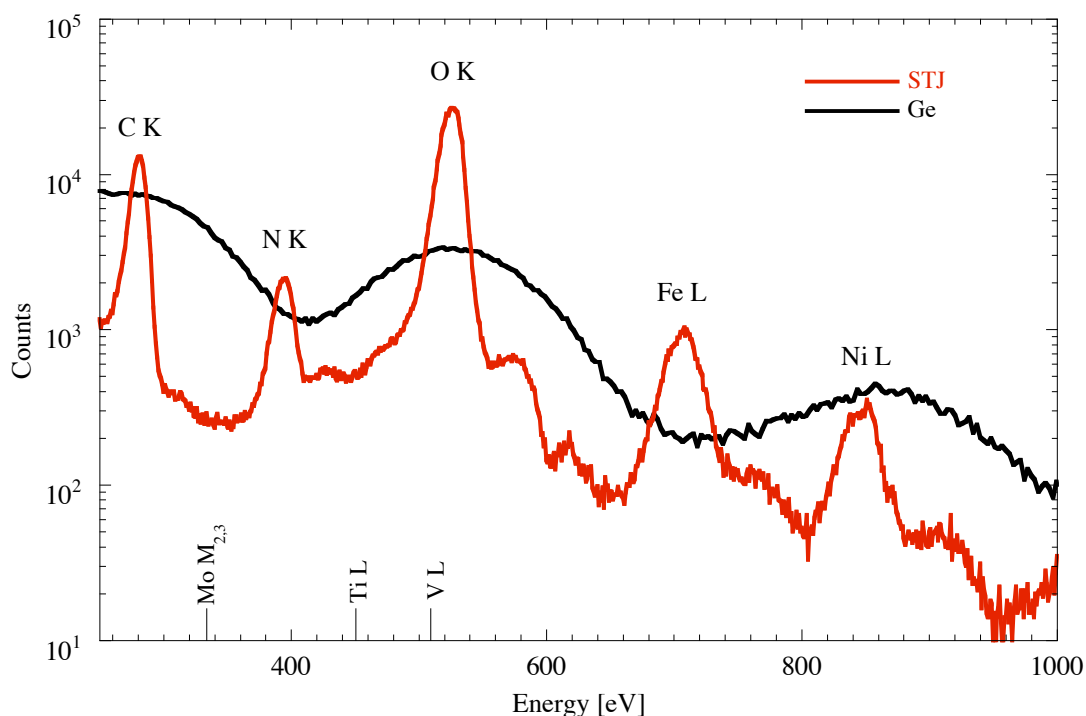


Figure 29: Single-pixel fluorescence spectrum of the metalloprotein hydrogenase from an STJ detector and a Ge detector. Note that the oxygen/nickel ratio is much higher in the STJ XRF spectrum because of the different transmission of the IR-blocking windows in front of the two detectors.

higher, as expected, and allows the full separation of the different X-ray fluorescence lines, and even the detection of the weak iron L_i line at 615 eV. (This is not just an academic curiosity, but can provide significant advantages when gating on the L_i line in moderately concentrated samples, because the L_i line tends to be less affected by self-absorption than the higher-energy $L_{\alpha,\beta}$ lines.) On the other hand, for the analysis of say nickel L-edge spectra the resolution of a good Ge detector is perfectly adequate to separate it from the oxygen K-emission that provides most of the interference in soft X-ray spectroscopy of metalloproteins. In fact, for such an analysis Ge detectors are preferred because of their larger area and solid angle and thus higher sensitivity compared to STJ detectors.

As an aside, the ability of the STJ to fully separate the X-ray emission from different

elements allows us to quantify the elemental composition in samples in exactly the same volume that is examined during XAS scans. This has, for example, led us to discover that Acetyl Cofactor-A Decarboxylase Synthase (ACDS) protein likely contains two nickel atoms per active site, contrary to the prevalent notion that there is only a single nickel atom in it [Funk 04]. It has also helped us to discover that the window in front of our Ge detector was much thicker than specified, based on the ratio of oxygen K to nickel L-fluorescence in Figure 29 that is much higher in the STJ XRF spectra than in the Ge XRF spectra. Also, in the context of this dissertation we have measured the XRF of FeMo-co and compared it to the spectrum of a mixture of model compounds whose ratio was chosen to simulate the nominal elemental composition of the elements of interest in FeMo-co (cf. section 3.1). The differences between the two XRF spectra have revealed that the FeMo-co concentration in a nominally pure FeMo-co sample can be more than an order of magnitude less than calculated.

In earlier work in the Advanced Detector Group at LLNL, the STJ response was systematically characterized as a function of energy and count rate by directly exposing it to a monochromatic synchrotron beam. Here we briefly summarize the results most relevant in the context of metalloprotein spectroscopy. Figure 30 shows the energy resolution of a $141\text{ }\mu\text{m} \times 141\text{ }\mu\text{m}$ junction that was operated at the end of a cold finger and illuminated directly with a monochromatic X-ray beam of high spectral purity at the Radiometry Laboratory of the Physikalisch Technische Bundesanstalt (PTB), the German National Metrology Institute, at the BESSY-II synchrotron in Berlin [Veldkamp 02, Friedrich 05]. The beam was attenuated by several orders of magnitude to avoid a degradation of the energy resolution due to pile-up. The electronic noise was measured concurrently with a

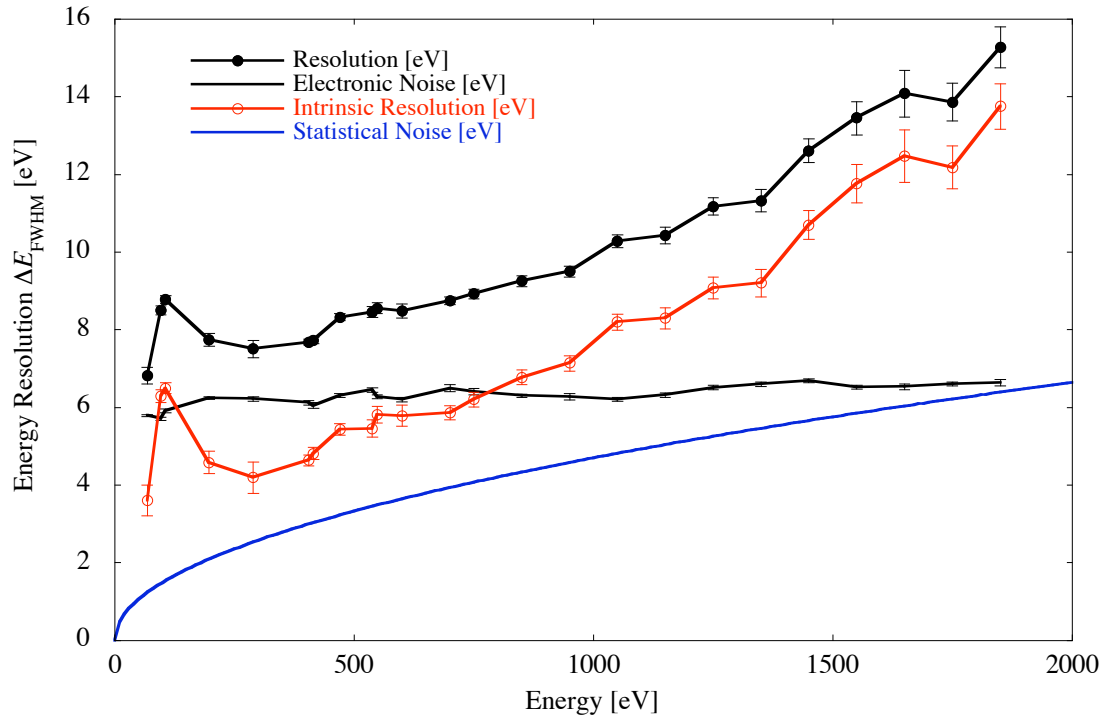


Figure 30: Monochromatic X-Ray Response of a $141\ \mu\text{m} \times 141\ \mu\text{m}$ junction. For energies below 1 keV the energy resolution is below 10 eV FWHM.

pulser. The main peak of the X-ray spectrum was fitted to a Gaussian function, and plotted as a function of incident energy. Figure 30 shows that the energy resolution varies between $\sim 7\ \text{eV}$ and $\sim 15\ \text{eV}$ FWHM for X-rays in the energy range between 50 eV and 2000 eV (solid circles). The degradation in energy resolution in the energy range between $\sim 100\ \text{eV}$ and $\sim 200\ \text{eV}$ is due to the partial transparency of the top niobium absorber film and subsequent partial absorption in the underlying aluminum trap (Figure 31) [Friedrich 01a]. The electronic noise in these measurements was constant at around $\sim 6.5\ \text{eV}$ FWHM (bars). If the electronic noise is subtracted in quadrature, the intrinsic energy resolution varies between 4 eV and $\sim 14\ \text{eV}$ FWHM for energies below 2 keV (open circles). This is still worse than the theoretically achievable energy resolution limited by the statistics of charge

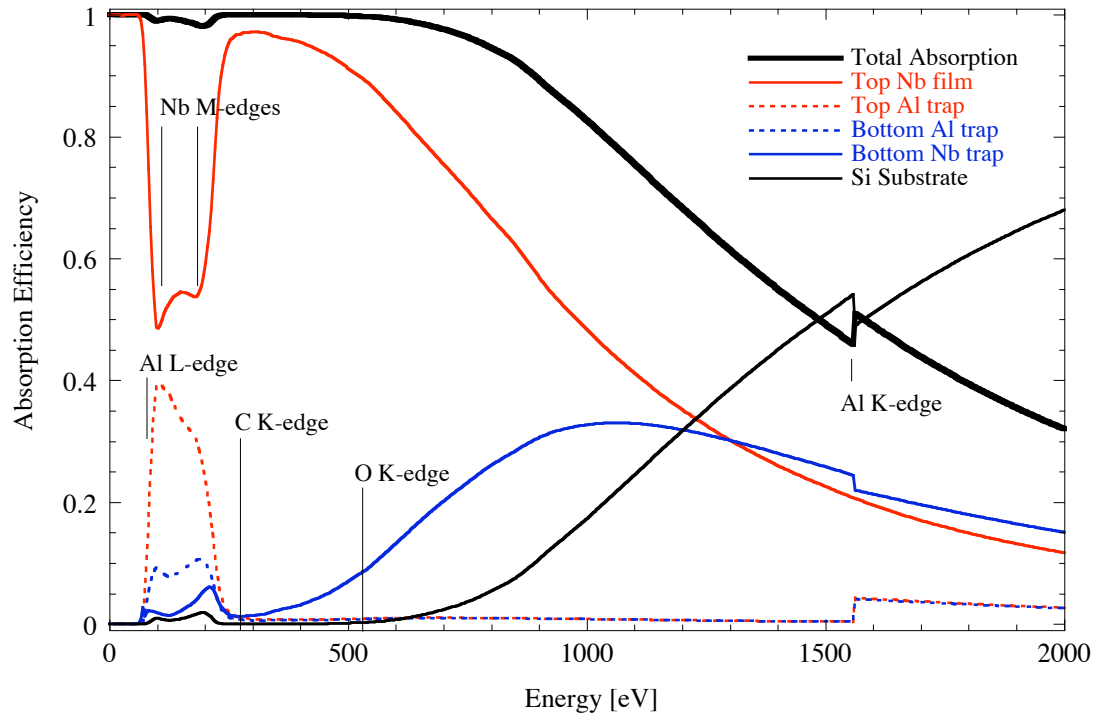


Figure 31: Here the relative absorption of each layer vs energy is shown. For energies between 100 eV and 200 eV, nearly 10% of events are absorbed in the bottom layer.

generation and tunneling (solid line) [Mears 93]. It is also worse than the energy resolution measured for smaller STJs from the same wafer that were operated deep inside the ADR, rather than at the end of a cold finger [le Grand 98, Friedrich 99b]. This suggests that the increased absorption of IR photons and the associated photon shot noise broadens the spectral response when an STJ detector is operated at the end of a cold finger.

Figure 32 shows the energy resolution of the same STJ detector at an energy of 277 eV corresponding to the carbon K-fluorescence as a function of count rate. These data were taken during the same beam time at BESSY-II by systematically varying the attenuation of the incident beam, keeping all other parameters constant. No pile-up rejection was used. The energy resolution remains roughly constant up to 10000 counts/s before it starts to

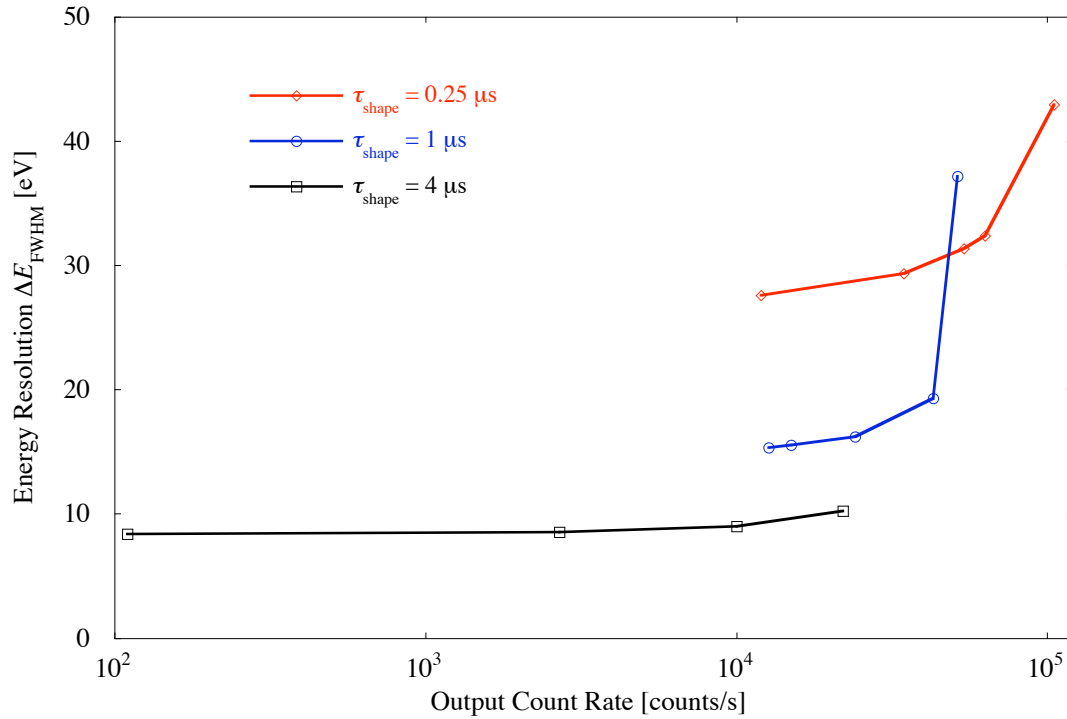


Figure 32: Energy resolution vs count rate. Energy resolution (FWHM) remains flat up to a maximum count rate limited by the amplifier shaping time. For higher count rates, shorter shaping times were used and resulted in modest increases in the FWHM.

degrade due to pile-up. At count rates above 30 000 counts/s the shaping amplifier saturates for a shaping time of 4 μs. Operating at higher rates up to 100 000 counts/s per pixel is still possible, but requires shorter shaping times of 1 μs or even 0.25 μs, with the attendant loss in energy resolution. However, this is not a limitation for synchrotron research with soft X-rays since the STJ pixels are intrinsically small and fluorescence yields below 1 keV are sufficiently low that STJ detectors are in practice rarely operated above 10 000 counts/s per pixel.

Figure 33 shows a photograph of the STJ with an overlay of the different response functions for illumination of different parts of the detector. Again, these data were taken during the same beam time at BESSY-II by illuminating different sections of the STJ

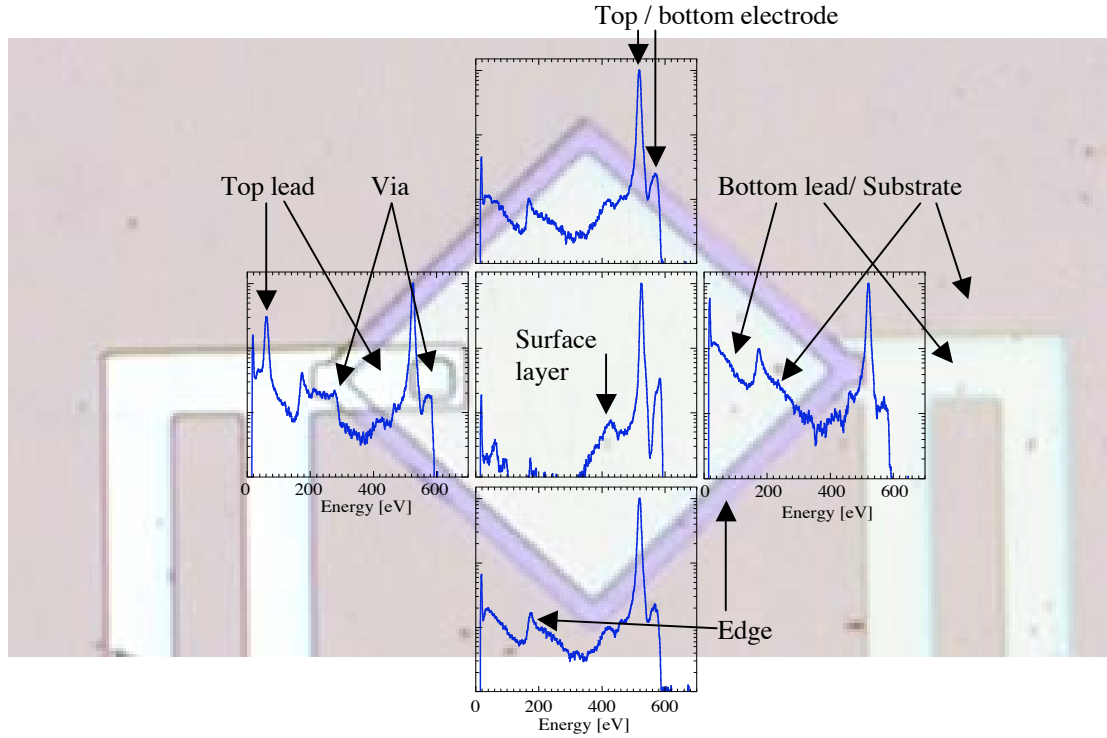


Figure 33: Photograph of a single STJ detector, showing the central square tunneling area, a somewhat larger base electrode extending from underneath, and the four niobium contact wires. Each spectrum is roughly overlaid with the $90\mu\text{m}$ diameter area of the STJ that was illuminated through the pinhole. Spectra are on a log scale and normalized to unity at 525 eV to enhance the artifacts. Comparing the spectra allows assigning each artifact to a particular aspect of the device geometry.

through a computer-controllable pinhole aperture with a $25\mu\text{m}$ diameter. Due to the divergence of the beam, the X-ray spot size was $\sim 90\mu\text{m}$ at the STJ. The data were taken at a constant excitation energy of 525 eV corresponding to the oxygen K-fluorescence, and all spectra are plotted on a log-scale and normalized to unity at 525 eV so that the spectral artifacts appear enhanced. Comparing the different spectra allows assigning each artifact to a particular aspect of the device geometry [Friedrich 05].

It is not surprising that X-ray absorption in locations other than the main niobium absorber film produces spectral artifacts, since the energy of the phonons generated upon

absorption is sufficient to break Cooper pairs in the junction electrodes once the phonons have propagated into them. The main peak at 525 eV is clearly visible in all spectra. It is always accompanied by a smaller peak at ~ 570 eV with the same intensity, which can be assigned to X-ray absorption in the niobium base electrode underneath the main absorber. This base electrode peak increases with increasing X-ray energy as expected from the relative absorption efficiency of the two layers (Figure 31). A peak at ~ 180 eV and a sloped background above that energy is visible in all spectra from the edge of the STJ, but not in the central spectrum. This artifact can be assigned to events in or just below the edge of the base electrode that extends beyond the top niobium film. The different energies are due to different degrees of quasiparticle recombination during lateral diffusion towards the tunnel barrier. The low energy cutoff at 180 eV corresponds to the maximum quasiparticle loss and thus to events at the outer edge of the base electrode. Two artifacts are only visible in the leftmost spectrum where the niobium wiring contacts the top electrode, and can be attributed to X-ray absorption in the wiring itself and in the via. The wide background below 200 eV is due to X-ray absorption in the silicon substrate. Its intensity increases at low energies because there are more absorption locations far away from each junctions from where a smaller fraction of the phonons are captured. Finally, there is a spectral "shoulder" between ~ 350 eV and ~ 500 eV below the main absorption peak in all of the spectra, including the central one. Its magnitude relative to the main peak is the same for all devices on a wafer, but it varies between wafers and sometimes worsens with time. We can assign this artifact to surface contamination on top of the niobium absorber, given that X-rays absorbed in this surface layer are less efficiently converted into electrical charges. This artifact can be a cause of the spectral background in XAS whenever a high-energy line

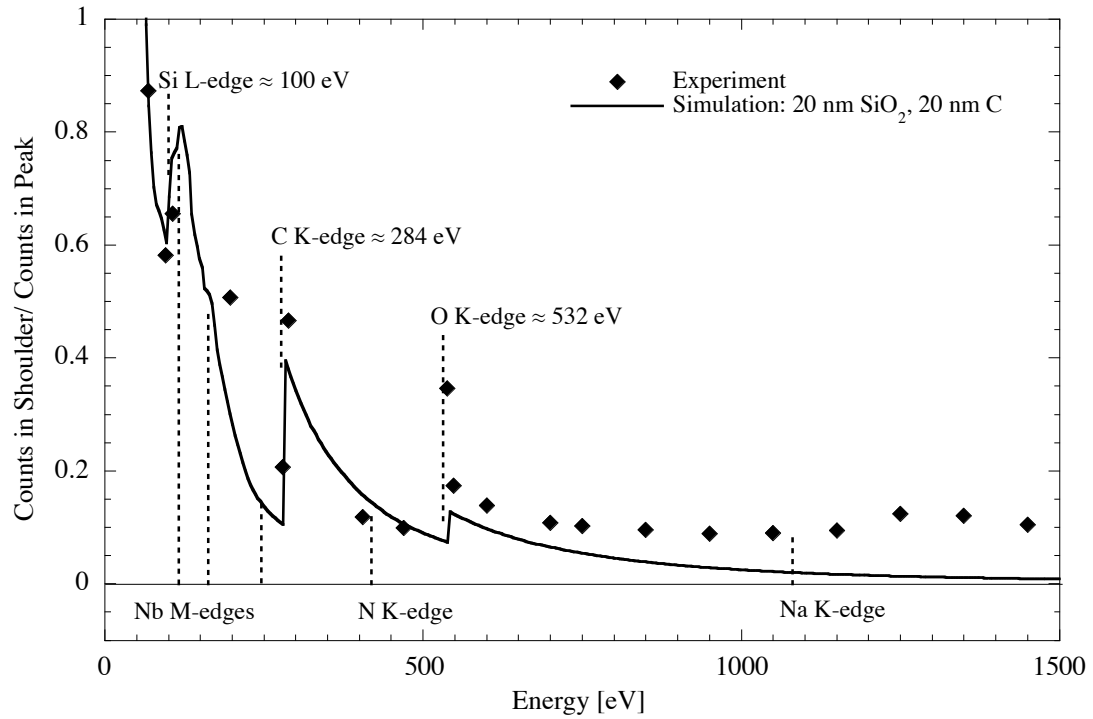


Figure 34: Intensity of the surface layer artifact, normalized to the number of counts in the main peak. The energies at which the number of counts in the artifact increases indicates which element it is caused by, and suggests possible remedies.

is excited by the second order undulator radiation and its associated surface layer artifact leaks into the window of interest. This effect is especially dominant for XAS below the oxygen K-edge at ~ 540 eV.

The surface layer artifact cannot be removed using pinhole masks and illuminating only the center of an STJ, as opposed to the edge and wiring artifacts. We have therefore examined its magnitude as a function of energy to determine its elemental composition and devise ways to reduce it in future STJ designs (Figure 34). We expect an increase of the artifact intensity, defined here as the total number on counts between 350 eV and 500 eV, relative to the intensity of the main peak at energies corresponding to the absorption edges of elements in the surface layer. We observe a clear increase in artifact intensity at the

energies corresponding to the silicon L-edge (~ 100 eV), the carbon K-edge (~ 280 eV) and the oxygen K-edge (~ 530 eV). This suggests that there is a residual SiO_2 layer on top of the niobium absorber that has not been completely removed during reactive ion etching. There is also likely some hydrocarbon contamination of the surface, which has been covered with protective photoresist for years and exposed to laboratory air for weeks at a time. There is no increase in the artifact intensity at the niobium $M_{4,5}$ -edges (~ 205 eV), the nitrogen K-edge (~ 400 eV), or the sodium K-edge (~ 1070 eV). This suggests that the artifact is not caused by a partially degraded niobium absorber, nor by residual nitrogen gas freezing out on top of the STJ, nor by sodium deposits from detector handling [Friedrich 05].

For operation at the synchrotron, it is actually not desirable to operate the STJs with the highest energy resolution. This is because there is, in general, a trade off between high energy resolution and high detection efficiency, as the energy resolution decreases with increased junction area due to increased capacitance and slight inhomogeneities in the detector response. For synchrotron-based XAS, it is more advantageous to increase the STJ spectrometer solid angle coverage by operating large pixels, as long as the energy resolution does not degrade to the point that the different fluorescence lines can no longer be separated. This sets the maximum pixel size to roughly $200\text{ }\mu\text{m} \times 200\text{ }\mu\text{m}$. We have therefore chosen comparably large 3×3 arrays of $200\text{ }\mu\text{m} \times 200\text{ }\mu\text{m}$ STJs for the STJ spectrometer at the ALS. Their response is quite homogeneous for different pixels from the same wafer because of the high-quality photolithographic process used for STJ fabrication (Figure 35) [Barfknecht 91].

In another trade-off between energy resolution and solid-angle coverage, we have also repeatedly modified the cold finger of the ADR cryostat to move these detector arrays

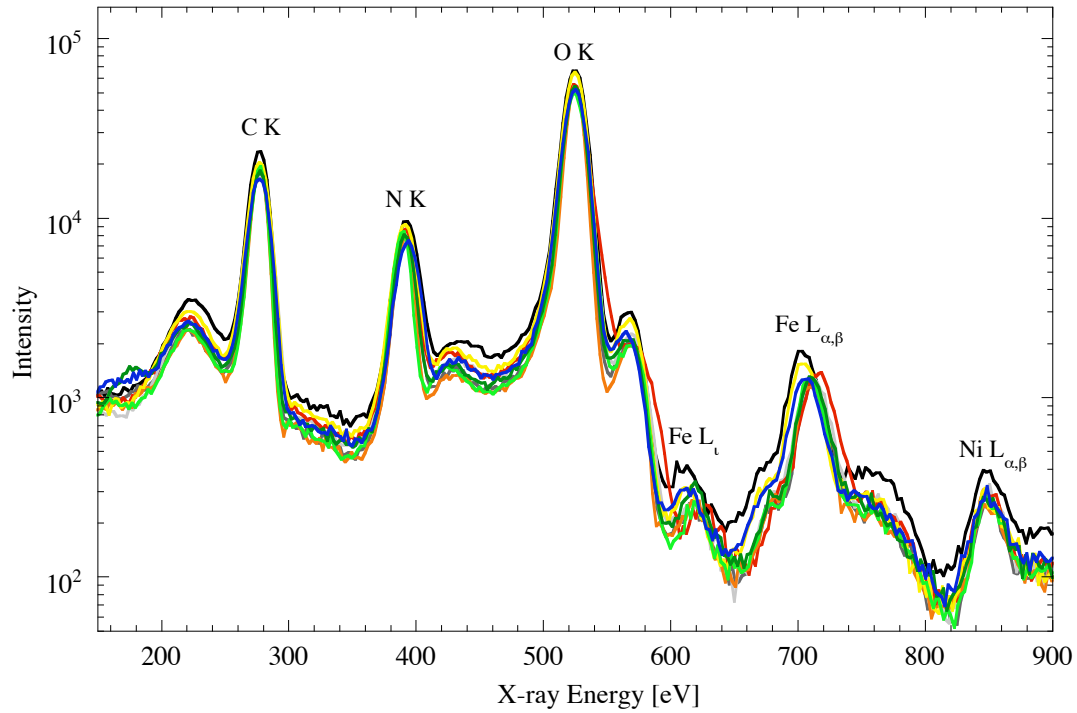


Figure 35: X-ray fluorescence spectra of the iron and nickel-containing metalloprotein hydrogenase, captured with 9 channels of an 3×3 array of STJ detectors.

closer to the sample in the UHV chamber. While this increases the IR-induced shot noise, the attendant loss in energy resolution is more that outweighed by the gain in solid angle coverage. These trade-offs are quantified in more detail in the following chapter.

2.4.2 Quantification of Spectrometer Sensitivity

We now quantify the improvements in sensitivity and signal-to-noise (S/N) ratio that STJ spectrometers can provide over conventional semiconductor or grating spectrometers for soft X-ray spectroscopy [Drury 05]. This analysis helps to determine which spectrometer provides the highest sensitivity for a given application, to assess how close a measurement is to the theoretically best achievable S/N ratio, and to guide future STJ detector development.

We consider the case when the detection of a fluorescence signal from an element x of interest at energy E_x with total counts N_x is affected by a nearby fluorescence line at energy E_y from element y with total counts N_y . We assume that the spectrometer response is Gaussian, and that it is adequately characterized by its full-width at half maximum ΔE_{FWHM} . We also take into account that the signal detection may be affected by a constant spectral background B , either due to elastic scatter of the incident beam, due to pile-up or due to non-idealities of the spectrometer response function. In this case, the limiting statistical contribution to the measurement errors σ_x and σ_y can be determined analytically [Ryder 77] according to

$$\begin{aligned}\sigma_x^2 &= aB + bN_x + cN_y \\ \sigma_y^2 &= aB + bN_y + cN_x\end{aligned}\tag{12}$$

where

$$\begin{aligned}a &= \frac{\Delta E_{\text{FWHM}} \sqrt{\pi}}{\sqrt{2 \ln 2} (1 - d^2)} & b &= \frac{2 - 4d^{\frac{7}{3}} + 2d^{\frac{10}{3}}}{\sqrt{3} (1 - d^2)^2} \\ c &= \frac{2d^{\frac{4}{3}} - 4d^{\frac{7}{3}} + 2d^2}{\sqrt{3} (1 - d^2)^2} & d &= e^{\frac{-2 \ln 2 (E_x - E_y)^2}{\Delta E_{\text{FWHM}}^2}}\end{aligned}$$

Equation 12 describes the statistical precision in the limiting case that systematic errors are negligible. It quantifies this limit in terms of line separation $(E_x - E_y)$ and detector resolution ΔE_{FWHM} , which enter through the parameter d . The parameter a describes the influence of the background B on the precision, and correctly leads to $\sigma_{x,y} \propto \sqrt{\Delta E_{\text{FWHM}}}$ when background statistics dominate the spectrum, i.e. in the limit $d \rightarrow 0$ and $B \gg (N_x + N_y)$. The parameter c quantifies the influence of the overlap of one line on the precision for measuring the other line. As expected, $c \rightarrow 0$ for well separated lines, i.e.

$d \rightarrow 0$ for $(E_x - E_y) \gg \Delta E_{\text{FWHM}}$.

It is now possible to compare the sensitivity of different X-ray spectrometers in terms of their energy resolution, count rate capabilities and detection efficiencies. We focus on the analysis of dilute samples, the primary motivation to develop STJ spectrometers for synchrotron science. Unless explicitly mentioned, we initially assume that there are $N = 10^7$ counts total in the spectrum, roughly corresponding to operating a 30-pixel detector array at rate of ~ 20000 counts/s per pixel and an acquisition time $\tau \sim 15$ s, that the signal N_x from the element x of interest constitutes only 1% of that total, and that the background B is negligible. The assumption of a negligible background is least realistic, and will be relaxed in the later part of this chapter. Assuming that the fluorescence yield of all elements in the sample is roughly comparable, a signal level of 1% roughly corresponds to a concentration of 1000 ppm of the element of interest, since the absorption by that element increases significantly at its absorption edges.

Figure 36 shows the S/N (N_x/σ_x) according to equation 12 as a function of energy resolution for different signal levels N_x corresponding to different concentrations of element x in the sample. If the spectrometer resolution is sufficient to fully separate the two lines, the S/N ratio is independent of energy resolution and approaches $1/\sqrt{N_x}$, since $\sigma_x \rightarrow \sqrt{N_x}$ according to Poisson's statistics. The energy resolution ΔE_{FWHM} starts to matter only when it is comparable to the line separation $(E_x - E_y)$, in which case the S/N ratio degrades roughly proportional to ΔE_{FWHM} or ΔE_{FWHM}^2 depending on the relative magnitude of the lines and the degree of line overlap [Ryder 77, Statham 95]. In general, high-resolution STJ spectrometers are therefore only preferred for soft X-rays where line overlap is more common, while conventional high-efficiency Ge spectrometers are preferred for harder

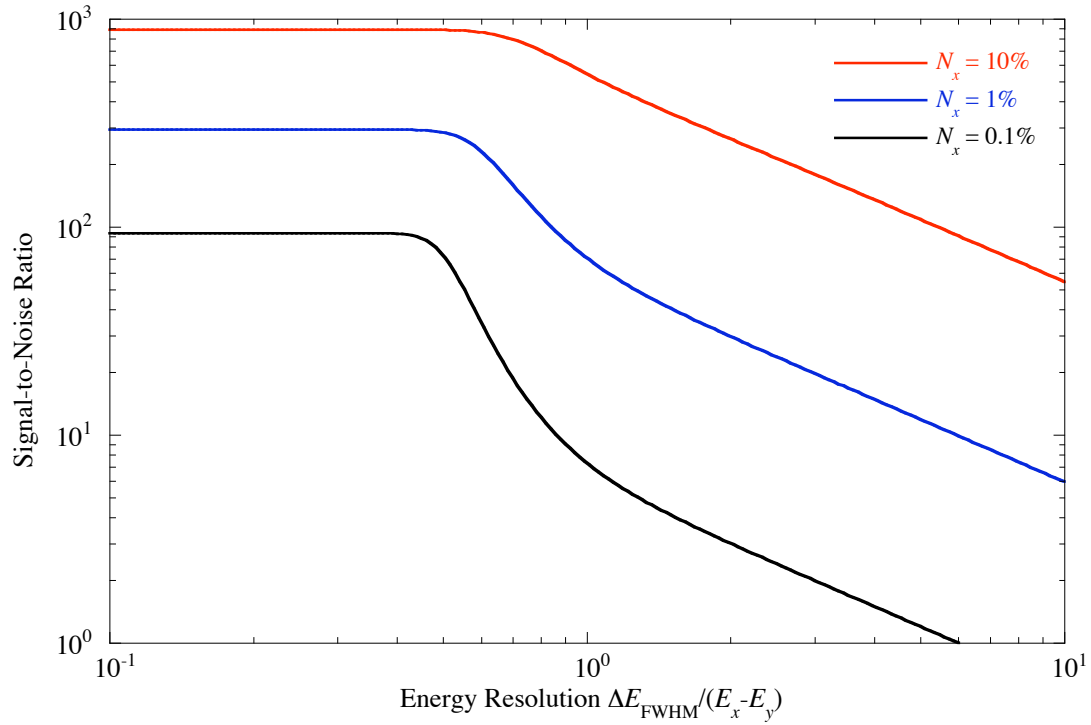


Figure 36: Signal-to-noise ratio for detecting a weak signal N_x at E_x as a function of energy resolution ΔE_{FWHM} in units of the line separation $(E_x - E_y)$ of that signal from a nearby emission line at E_y . The plot shows the limiting S/N ratio when the signal N_x is 10%, 1% and 0.1% of the total ($N = 10^7$). A S/N ratio above 100 is desirable for precise chemical analysis, and S/N ratios below 10 are marginal. A S/N ratio of 3 is often called the detection limit.

X-rays.

In X-ray spectroscopy, there is usually a trade-off between spectrometer energy resolution and count rate. High data acquisition rates require shorter shaping times to reduce pile-up and thus increase the electronic noise. Also, for weak excitation sources or low X-ray fluorescence yield, spectrometers often do not collect sufficient counts to be operated at their maximum rate. Figure 37 shows how the S/N ratio improves with count rate for an acquisition time $\tau = 15$ s and different degrees of line overlap $\Delta E_{\text{FWHM}} / (E_y - E_x)$. For a given τ the S/N ratio improves with the square root of the count rate because of Poisson's statistics. The degree of line overlap then determines the

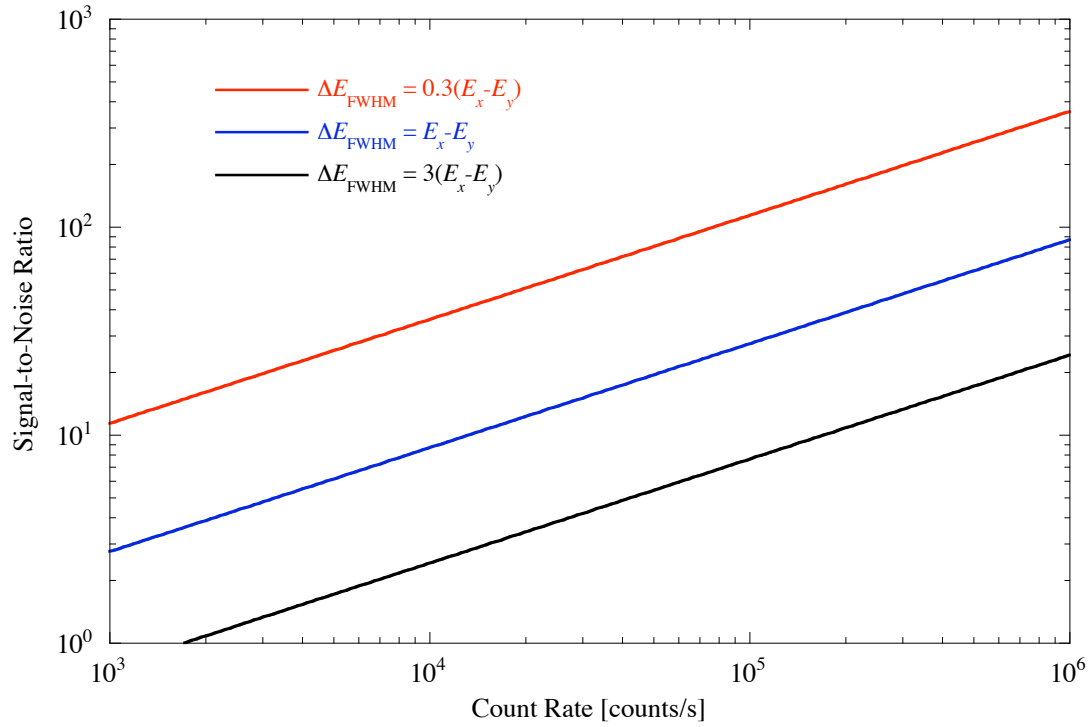


Figure 37: Signal-to-noise ratio as a function of total count rate for different degrees of line overlap, a signal rate of 1% and an acquisition time of 15 s.

absolute value of the S/N ratio that can be attained within a given acquisition time τ .

Ge, STJ and grating spectrometers have vastly different total detection efficiencies, ranging from $\sim 10^{-6}$ for high-resolution gratings to $\sim 10^{-1}$ for large Ge detector arrays. The term “efficiency” is used here to describe the fraction of the total number of fluorescence X-rays emitted from the sample that are recorded in the spectrum. It is given by the product of the solid angle $\Omega/4\pi$ that the spectrometer subtends and the quantum efficiency η of the detection process. Figure 38 demonstrates how the detection efficiency affects the achievable S/N ratio for different degrees of line overlap. The simulation assumes typical values of the incident flux ($I_0 = 10^{12}$ photons/s), the fluorescence yield ($\epsilon = 10^{-3}$ for soft X-rays) so that there is a total fluorescence flux of 10^9 photons/s. As

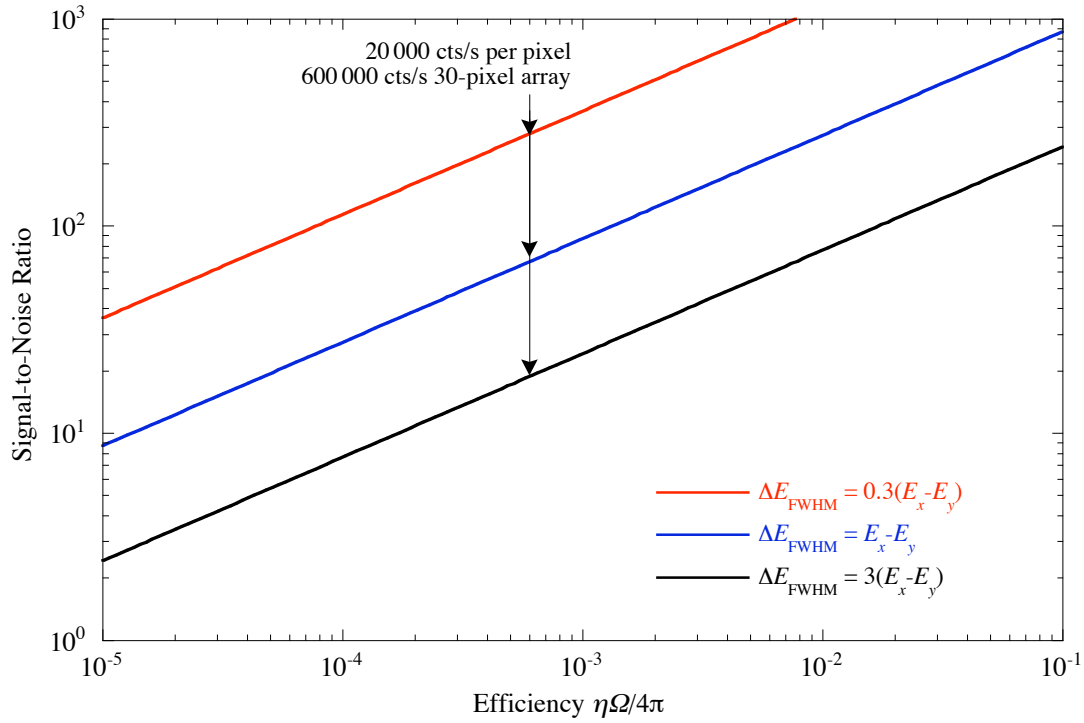


Figure 38: Signal-to-noise ratio as a function of detection efficiency for different degrees of line overlap and a signal rate of 1% of the total. The arrows indicate a total count rate of 20 000 counts/s per detector pixel.

expected, the S/N ratio increases with the square root of the detection efficiency because of Poisson's statistics. However, it decreases more rapidly with line overlap (cf. Figure 36). From a practical point of view this implies that the spectrometer should be used that has the highest efficiency while still being able to separate the lines of interest. Figure 38 is similar to Figure 37, in the sense that the improved S/N ratio relies on improved counting statistics. One difference is that the efficiency cannot be increased arbitrarily without exceeding the maximum count rate capabilities of the spectrometer. This is indicated by the arrow in Figure 38 where the total count rate exceeds 20 000 counts/s per detector pixel.

So far we have assumed that the spectral background B is negligible. Many spectrometers have a peak-to-background (P/B) ratio of 200 or better, so this approximation

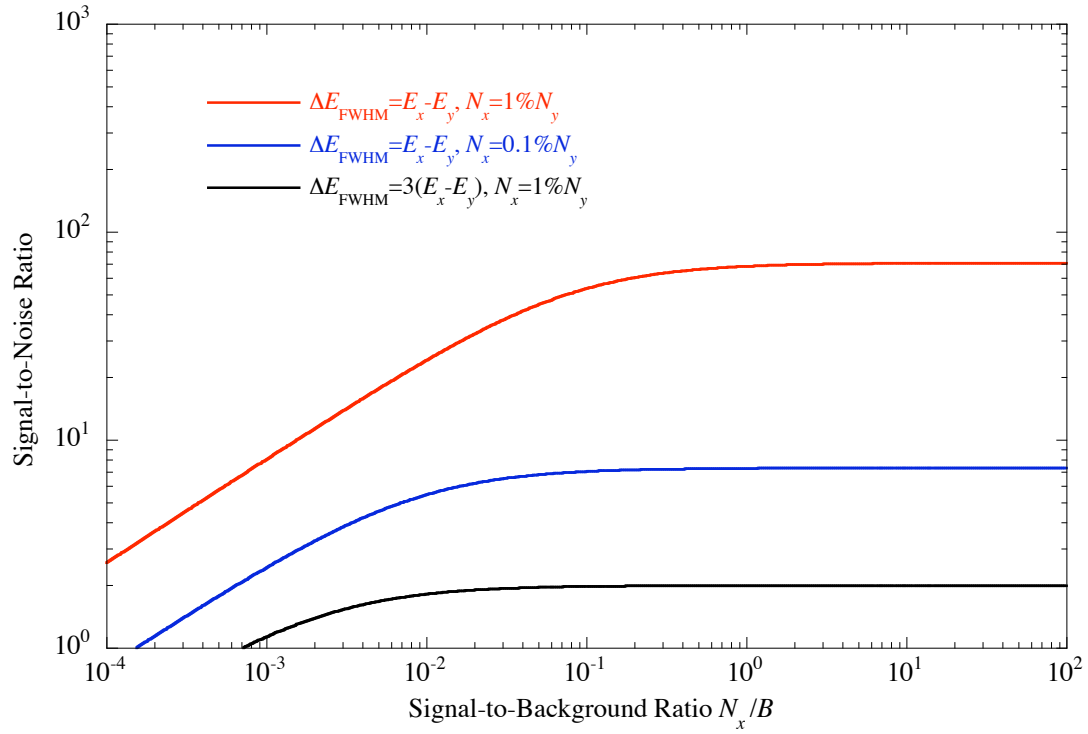


Figure 39: Signal-to-noise ratio as a function of spectral background for different degrees of line overlap and a signal rate of 0.1% and 1% of the total.

is often justified. However, for dilute samples, small spectral artifacts, a finite background due to dark counts, or elastic scatter of the incident beam can dramatically decrease the spectrometer sensitivity. Fluorescence spectra shown in chapter 3 illustrate the importance of the background counts even for XAS with high-resolution STJ detectors. The influence of spectral background is quantified in Figure 39. While we have seen in section 2.4 that the response function of the STJ does not produce a constant background over the entire soft X-ray band, the assumption of a constant background is still roughly justified in the most common case where the line of interest covers only a small fraction of this band and the background counts are dominated by interference from a single other line. As before, we assume a total number of counts $N = 10^7$, and a fraction of 1% or 0.1% in the

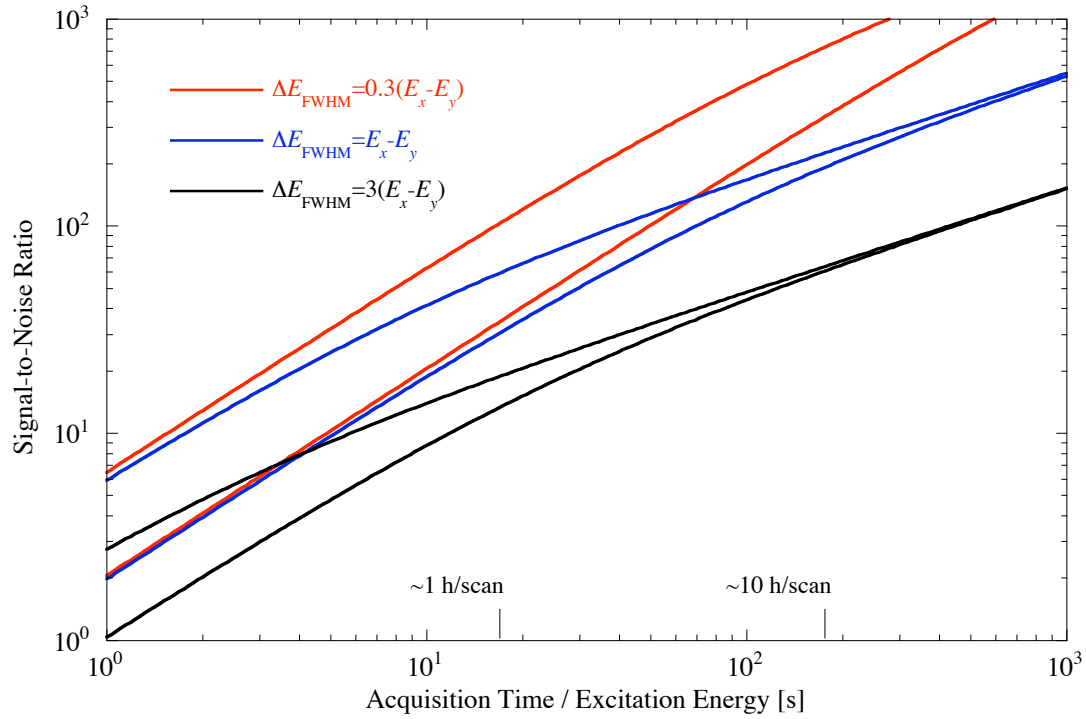


Figure 40: Signal-to-noise ratio as a function of data acquisition time and a signal strength of 1% (upper) and 0.1% of the total (lower line of each pair) for different degrees of line overlap. These signal rates roughly correspond to a sample concentration of 1000 ppm and 100 ppm, respectively.

signal, i.e. $N_x = 10^5$ or 10^4 . In the background-dominated case, the S/N ratio improves with $\sqrt{\Delta E_{\text{FWHM}}}$, since the signal counts are concentrated in a smaller energy range. This energy range decreases linearly with ΔE_{FWHM} , and associated error therefore decreases with $\sqrt{\Delta E_{\text{FWHM}}}$.

Ultimately, it is always possible to compensate for the finite energy resolution of a spectrometer through longer acquisition times, subject only to the constraints of radiation damage and/or patience. The improvements in S/N ratio are shown in Figure 40 for data acquisition times between 1 s and 5 min. This range was chosen since typical X-ray absorption spectra involve stepping the excitation energy through an absorption

edge of the element of interest, and acquiring a fluorescence spectrum at each energy. Typical absorption spectra involve ~ 200 steps, so that an acquisition time of 5 min per excitation energy corresponds to a total scan time of 10 h, the maximum realistic acquisition time per sample even when averaging many scans. Again, we assume an acquisition rate of 6×10^5 counts/s, corresponding to 30 detector elements operating at 20 000 counts/s each. Figure 40 shows that an acquisition time of 10 s to 15 s per step is sufficient to analyze elements at a concentration of ~ 1000 ppm ($\Rightarrow N_x = 1\%$) in a single ~ 1 h XAS scan and obtain an adequate S/N ratio above 100, in agreement with our observations [Friedrich 02, Funk 04]. More dilute samples with a concentration of ~ 10 ppm ($\Rightarrow N_x = 0.01\%$) currently require longer acquisition times of at least 10 h, achieved by averaging the results of several scans. In the future, this time will be reduced using larger detector arrays with higher efficiency and count rate capabilities.

We now apply this analysis to synchrotron-based fluorescence-detected XAS of dilute samples. As an example, we consider the first-row transition metals Sc, Ti, V, Cr, Mn Fe, Co, Ni, Cu and Zn, since they play important roles as trace elements in the metabolic processes in cells. Scientific questions in bioinorganic chemistry often center on the chemical state of the transition metal and its changes under specific conditions, and L-edge XAS is a sensitive element-specific probe of that state [de Groot 90, Cramer 91]. The L-series X-ray emission lines of first row transition metals range from 395 eV for scandium to 1012 eV for zinc. The most common line overlap problems in that energy range tend to be due to strong carbon K and oxygen K-fluorescence at 277 eV and 525 eV. Here we discuss the trade-offs between energy resolution, count rate and efficiency when analyzing these transition metals by XAS, and quantify the sensitivity different spectrometer types

can attain.

If a dilute sample is illuminated at the synchrotron with a monochromatic X-ray beam with energy E_0 and $I_0 = 10^{12}$ photons/s, the measured signal N_x at energy E_x from element x within an acquisition time τ is given by [Jaklevic 77]

$$N_x = I_0 \tau \cdot \frac{\mu_x(E_0) \cdot \epsilon_x}{\mu_{\text{tot}}(E_0) + \mu_{\text{tot}}(E_x)} \cdot \frac{\Omega}{4\pi} \cdot \eta. \quad (13)$$

Here μ_x is the absorption coefficient of the element x and μ_{tot} is the total absorption efficient of the sample, ϵ_x is the fluorescence yield, $\Omega/4\pi$ is the solid angle the detector covers, and η is the detector's quantum efficiency. If all elements in the sample had the same absorption efficiency and fluorescence yield, the term $\mu_x(E_0)/(\mu_{\text{tot}}(E_0) + \mu_x(E_x))$ would be roughly equal to the concentration of element x in the sample. In practice it is about an order of magnitude higher since the element x has an increased absorption coefficient at its absorption edges.

While Ge, STJ and grating spectrometers can be used for fluorescence-detected XAS, these spectrometers vary greatly with respect to energy resolution, count rate capabilities and detection efficiency. Table 1 summarizes their performance at 0.5 keV for (a) typical (Figure 41), (b) state-of-the art, and (c) theoretically ideal instruments. The “typical” Ge detector describes the original average performance of our commercial 30-element Ge spectrometer [CANBERRA 88]. The currently “best” Ge detector, chosen solely for its achieved resolution at 0.5 keV, is a single channel Ge detector optimized for low-energy performance [Gresham05]. The “ideal” Ge detector would combine Fano-limited resolution with 30-channel array capability. Its peak-to-background (P/B) ratio is limited by a ~ 15 nm dead layer at the contact electrode [Lepy 00].

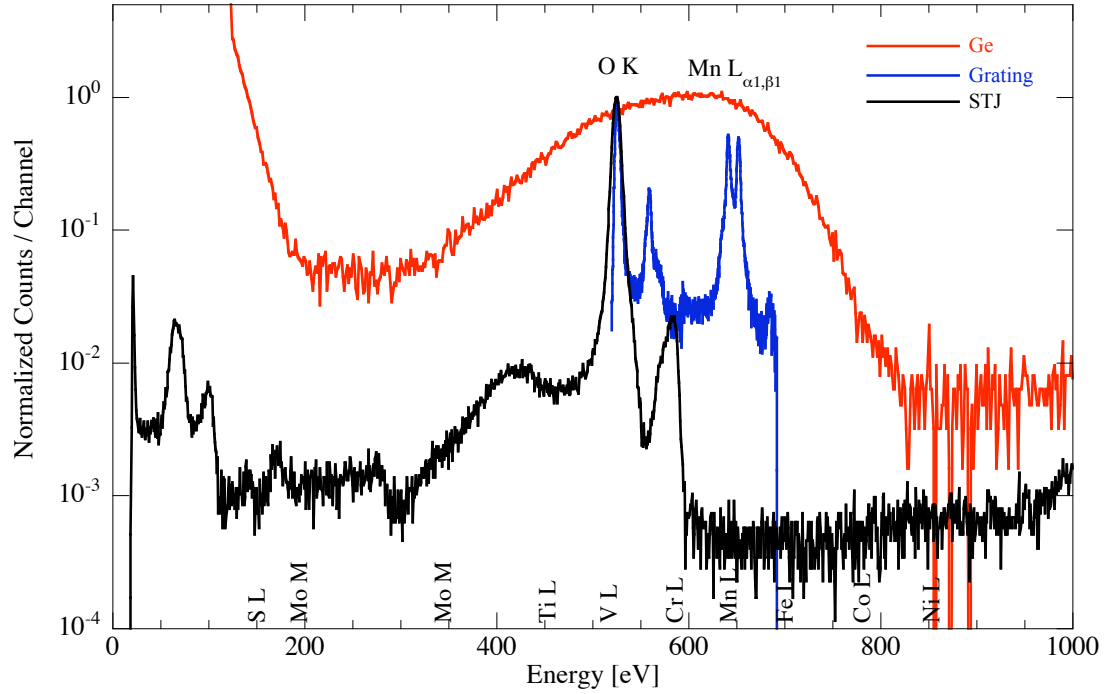


Figure 41: Comparison of normalized detector response functions for MnO (Ge and grating spectrometer) and a monochromatic 525 eV beam (STJ). Labels on the x-axis correspond to the approximate L-series fluorescence energies for sulfur and some first row transition metals as well as Mo M-series. Note the vicinity of the vanadium and chromium emission lines with the oxygen K fluorescence at 525 eV.

Detector	Resolution ΔE_{FWHM}	Count Rate [counts/s]	Efficiency $\eta \Omega / 4\pi$	P/B ratio
Ge (typical)	130 eV	3×10^5	0.1	50:1
Ge (best)	60 eV	3×10^4	3×10^{-2}	200:1
Ge (ideal)	40 eV	10^7	0.1	1000:1
STJ (typical)	20 eV	10^5	10^{-4}	200:1
STJ (best)	10 eV	10^6	10^{-3}	1000:1
STJ (ideal)	5 eV	10^7	10^{-2}	5000:1
Grating (typ.)	0.5 eV	10^5	10^{-6}	200:1
Grating (best)	0.2 eV	10^6	10^{-5}	1000:1
Gr. with optic	0.2 eV	10^6	3×10^{-4}	200:1
Grating (ideal)	0.1 eV	10^7	10^{-3}	5000:1

Table 1: Spectrometer performance at an X-ray energy of 0.5 keV. All values are approximate.

The “typical” STJ detector describes the performance of our current 9-pixel STJ spectrometer during past routine operation [Friedrich 02]. The “best” STJ combines achieved energy resolution [le Grand 98] and P/B ratios [Friedrich 99a, Bechstein 04] with the efficiency and count rate capabilities of our recent 36-pixel upgrade (Figure 41). The “ideal” STJ combines Fano-limited resolution [Mears 93] with a future upgrade to ~ 1000 pixels. Unlike Ge detectors, STJs do not have an unavoidable dead layer. While the small detector size limits its solid angle coverage, it allows placing most of the STJ array at an angle of 90° to the incident beam, thereby limiting elastic scatter and maintaining a high P/B ratio.

Grating spectrometers are typically optimized for spectroscopy and routinely achieve sub-eV resolution below 1 keV [Nordgren 00], at the expense of low efficiency (Figure 41). However, the efficiency can be improved by using a point-to-parallel X-ray optic before the diffraction grating with large cone angles [Parallax05]. The P/B ratio is typically set by the scattered incident beam.

We now apply the sensitivity analysis based on equation 12 to X-ray spectroscopy of dilute transition metals using signal rates according to equation 13 and the spectrometer characteristics of table 1. We assume an incident flux $I_0 = 10^{12}$ photons/s characteristic for beam line BL 4.0.2 at the ALS and an acquisition time $\tau = 15$ s per excitation energy for an XAS scan time of ~ 1 h. Considering the increased μ_x at the absorption edges, we set $\mu_x(E_0)/(\mu_{\text{tot}}(E_0) + \mu_x(E_x))$ to 10^{-3} for a metal concentration of 1000 ppm, and use published values for the fluorescence yield ε_x , which varies between 8.4×10^{-4} for scandium and 1.2×10^{-2} for zinc L-edges [Krause 79]. The count rate is either set by the spectrometer characteristics or by the signal rate from the sample. We also assume that

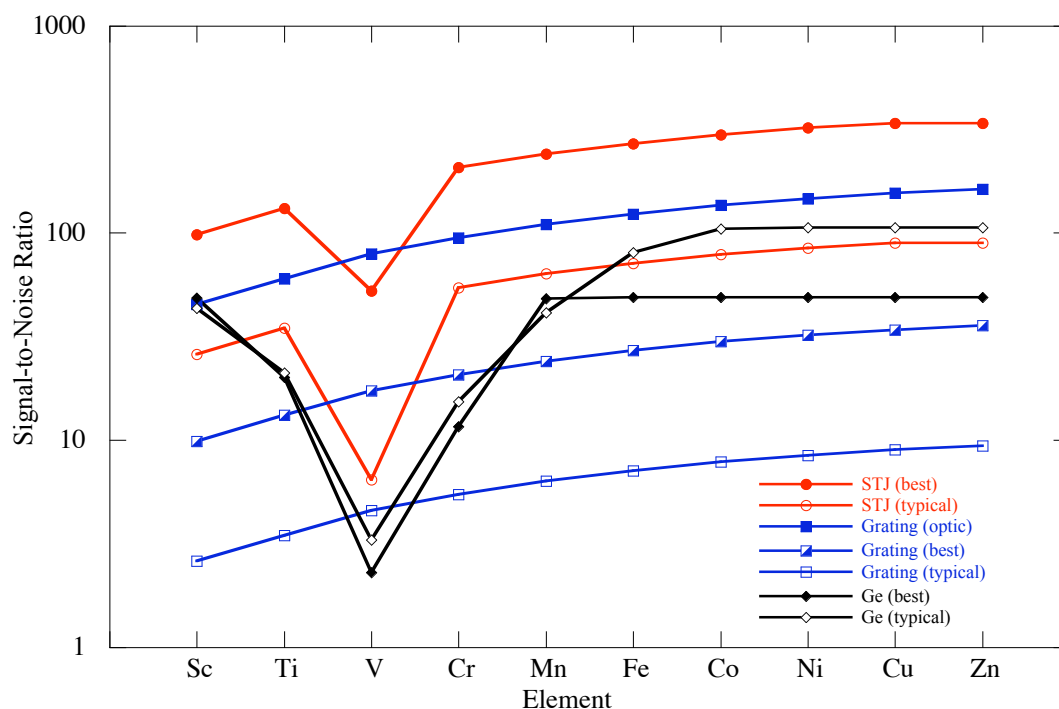


Figure 42: Signal-to noise ratio for analyzing L-series X-rays of first-row transition metals with a concentration of ~ 1000 ppm for a data acquisition time of 15 s. Spectrometer parameters are taken from table 1.

the only potential line overlap arises from the oxygen K-fluorescence at 525 eV, and that this line is 100 times stronger than the fluorescence from the transition element of interest. These are typical numbers for the analysis of transition metals in ~ 20 mM protein films.

Figure 42 shows the statistics-limited S/N ratio for the analysis of first-row transition metals with a metal concentration of ~ 1000 ppm for different spectrometer types. In general, the S/N ratio increases slightly for the heavier elements because of the higher fluorescence yield ϵ_x and thus higher signal rates, with lower S/N ratios for vanadium, chromium and manganese whose emission lines are near the interfering oxygen K-fluorescence at 525 eV. For the elements scandium and iron to zinc, 30-element Ge spectrometers (diamonds) offer higher sensitivity than a typical 9-pixel STJ spectrometer,

because they efficiently capture the weak signal with high S/N ratio as long as there are no large interfering fluorescence lines nearby. STJ spectrometers (circles) are favorable for the elements titanium to manganese because they can separate their weak metal fluorescence from the interfering oxygen K-fluorescence line, with lower efficiency than Ge spectrometers, but sufficient to acquire XAS spectra with high S/N ratio within a ~ 1 h scan. The recent 36-pixel detector upgrade significantly enhances the sensitivity of STJ spectrometers because of the higher detection efficiency and count rate capabilities (solid circles).

Note that even the best single-channel Ge spectrometer with an energy resolution of 60 eV and an area of 10 mm^2 does not provide higher sensitivity because of its limited count rate capabilities (which cause the S/N ratio to remain constant for the elements manganese to zinc in this simulation) and the spectral background due to the electrode's dead layer. Except for the case of severe line overlap between the vanadium L and oxygen K-emission, grating spectrometers (squares) tend to be less favorable for the analysis of dilute specimens despite their high energy resolution because of their low detection efficiency. High efficiency X-ray focusing optics can partially alleviate this problem, although they could of course also be used to further improve the efficiency of STJ spectrometers.

In summary, we have quantified the signal-to-noise ratio that different X-ray spectrometers can attain as a function of energy resolution, count rate and detection efficiency for samples with different metal concentrations and degrees of line overlap. STJ spectrometers tend to be preferred for the L-edge XAS of first-row transition metals over conventional high-purity Ge spectrometers for the analysis of the lighter elements titanium to manganese when oxygen fluorescence can cause a significant spectral background.

STJs can also be used to analyze heavier elements, although current multi-element Ge spectrometers are more sensitive in that case because of their larger effective area. Future STJ detector development should focus on increasing their detection efficiency and sensitivity by improving the spectral purity of their response function and by developing larger arrays. There is less need to further improve energy resolution, since most lines can already be well separated with STJs, and count rate capabilities, since the fluorescence yield for soft X-rays is low. The recent upgrade to 36 pixels makes STJ spectrometers the preferred instrument for the chemical analysis of dilute (~ 100 ppm range) specimens by soft X-ray absorption spectroscopy. The next upgrade to 112 pixel STJ detectors will increase the sensitivity to metal concentrations into the 10 ppm range, corresponding to, for iron, ~ 0.2 mM concentration.

3 Soft X-Ray Spectroscopy of Nitrogenase

The superconducting tunnel junction (STJ) spectrometer introduced in the last section was built for use at the Advanced Biological and Environmental X-ray Facility at Lawrence Berkeley National Laboratory in order to study the molecular reaction mechanisms of biological processes such as photosynthesis, nitrogen fixation or hydrogen evolution [Friedrich 03, Funk 04, Lordi 03]. These reactions occur at metallic centers in the active sites of proteins, and are accompanied by changes in the electronic structure of the metal atoms and the ligands involved in the chemical binding. One approach to study this electronic structure and its changes during the catalytic cycle is by fluorescence-detected X-ray absorption spectroscopy (XAS) at the synchrotron. X-ray spectroscopy provides elemental specificity, and the tunable monochromatic X-ray beam at a synchrotron allows sampling the associated electronic states with natural linewidth limited resolution. In this context, STJ spectrometers allow the extension of XAS to the soft X-ray band to study the lower energy absorption edges and exploit their increased sensitivity to chemical changes because of their narrower natural linewidths.

The active sites of enzymes that catalyze oxidation and reduction reactions often contain transition metals such as manganese, iron or nickel, because they can easily change oxidation states by accepting electrons into or donating electrons from their partially-filled *d*-shells, as required to bind substrates and catalyze their reactions. Among the metals, molybdenum is the only second-row transition metal naturally employed in biological reactions. Since molybdenum is comparably abundant and can bind to a wide variety of substrates in different oxidation states and ligand symmetries, enzymes containing

molybdenum are found throughout the range of life, from plants to bacteria to higher animals.

Another common component in biological systems are iron–sulfur clusters, which function both as catalysts and as electron carriers for redox reactions. The chemical versatility of both iron and sulfur ions accounts for one of the most prominent functions for iron–sulfur clusters, namely that of electron transfer [Beinert 97, Rees 03]. These clusters exist in different structural stoichiometries that can contain one, two, three or four iron atoms together with inorganic sulfide. In all of these structures, the iron atoms are tetrahedrally coordinated to four ligands. In most cases all four ligands are sulfur, and the structures are therefore collectively described as $[n\text{Fe}-m\text{S}]$ clusters, where n and m are integers.

In this dissertation we examine how the STJ spectrometer can contribute to the study of lower energy edges of elements that are involved in biological catalysis. We focus on the metalloprotein nitrogenase responsible for converting dinitrogen to ammonia, because it is a chemical reaction of fundamental scientific and technological importance whose reaction mechanisms has been the subject of debate for a long time, and because the variety of metals involved makes it an interesting test case for the use of STJ spectrometers at the synchrotron.

Figure 43 shows the FeMo-co molecule with the element targets for soft X-ray spectroscopy. It is clear that every element of the FeMo-co core can be probed using the soft X-ray region. Specifically, we examine if spectroscopy of the molybdenum M-edges at $\sim 220\text{ eV}$ and $\sim 400\text{ eV}$ and sulfur L-edges at $\sim 160\text{ eV}$ can provide complementary information to the commonly used molybdenum K and L-edges at 20 keV and 2.6 keV ,

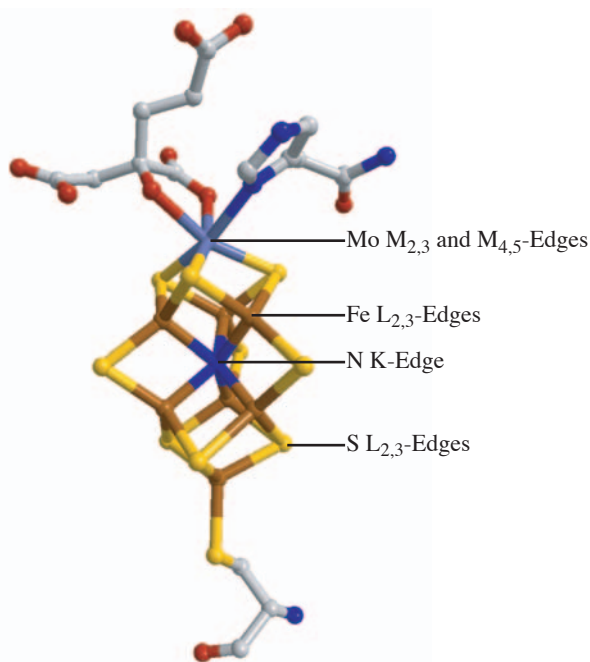


Figure 43: Soft X-ray spectroscopy targets for FeMo-co. Every element at the core of the cofactor has an edge in the soft X-ray region that contains allowed transitions.

respectively, and the sulfur K-edges at 2.5 keV. We also examine if chemical reactions involving the binding of light elements (such as nitrogen) to a metal (such as iron) can be examined by complementary spectroscopy of the same electronic orbitals at the light element and the metal edges.

Section 3.2 examines if it is possible to use the STJ spectrometer for sulfur L-edge spectroscopy to detect possible changes in sulfur chemical state in FeMo-co and other iron–sulfur clusters of biological interest. Very little fluorescence-detected XAS at the sulfur L-edges has ever been published, because the extremely low sulfur L-fluorescence energy of ~ 140 eV precludes the use of conventional high-purity Ge detectors. While STJ detectors work comfortably in that energy range, the need for three IR-blocking windows between the sample and the STJ detector reduces the detection efficiency and thus the sensitivity at these very low energies. In this context the use of alternative window materials such as palladium with potentially better X-ray transmission at that energy than

the conventional Al-parylene filters is examined.

Section 3.3 addresses the question whether the M-center of the MoFe nitrogenase does in fact contain an interstitial nitrogen ligand. The presence of an interstitial nitrogen can be tested using nitrogen K-edge XANES and EXAFS. The EXAFS signal for a central nitrogen atom is expected to be very strong if it is coordinated by six iron atoms. However, for this experiment we first need to examine if it is possible to extend the range of nitrogen EXAFS spectra through the oxygen K-edge at 525 eV without being affected by interference from the oxygen K-fluorescence. These measurements also require the availability of the M-center in a state where the only nitrogen signal arises from the potential interstitial nitrogen, which is difficult given that FeMo-co is typically extracted with nitrogen-containing N-methyl formamide (NMF). We tested the feasibility of this experiment by examining interstitial nitrogen model compounds such as $[\text{Fe}_6\text{N}(\text{CO})_{15}]^{3-}$ [Della Pergola 96].

Section 3.4 uses the STJ to measure the average iron oxidation state in FeMo-co at the iron L-edge through comparison with spectra of iron in different $[n\text{Fe}-m\text{S}]$ clusters with known oxidation states. While it is possible to take iron L-edge spectra with Ge detectors, the signal-to-noise (S/N) ratio tends to be higher when a high-resolution STJ is used. Furthermore, spectroscopy of the different elements of a biological system at absorption edges that are accessible at the same soft X-ray beam line allows examining different scientific questions on the exact same sample during a single run.

3.1 Molybdenum Spectroscopy

Molybdenum is the only second-row transition element that plays a significant role in natural biological processes. It is involved in oxygen transfer in oxidases, and in the process of nitrogen fixation in various nitrogenases. Under molybdenum-poor conditions, organisms can still fix nitrogen with vanadium substituting for molybdenum in the active site, or even with an all-iron nitrogenase protein. However, the process is most efficient (and most-studied) when molybdenum is used. The molybdenum chemistry in the active site of nitrogenase has been examined by XAS with hard X-rays for several decades [Cramer 77, Cramer 78]. This has provided significant insight about the structure of the active site. However, the molecular mechanisms of nitrogen fixation and the potential role of molybdenum in it are still not fully understood.

Here we examine if spectroscopy on the lower energy molybdenum M-edges in the soft X-ray band, which require high energy resolution and thus an STJ detector, can provide additional insights into molybdenum chemistry of the M-cluster in nitrogenase. These lower energy M-edges are known to have narrow intrinsic linewidths and large edge energy shifts with oxidation state, and are thus expected to provide higher sensitivity to chemical changes, since the ratio of the edge shift per oxidation state to absorption linewidth is much larger than at the K and L-edges.

Figure 44 illustrates the increasing sharpness of lower energy edges by comparing the Mo K, L, and M-edges. of the same compound Na_2MoO_4 . The spectra have been shifted by the different edge energies so that transitions into the same empty electronic states line up at $E = 0$. As expected, the lower energy edges have a much narrower edge

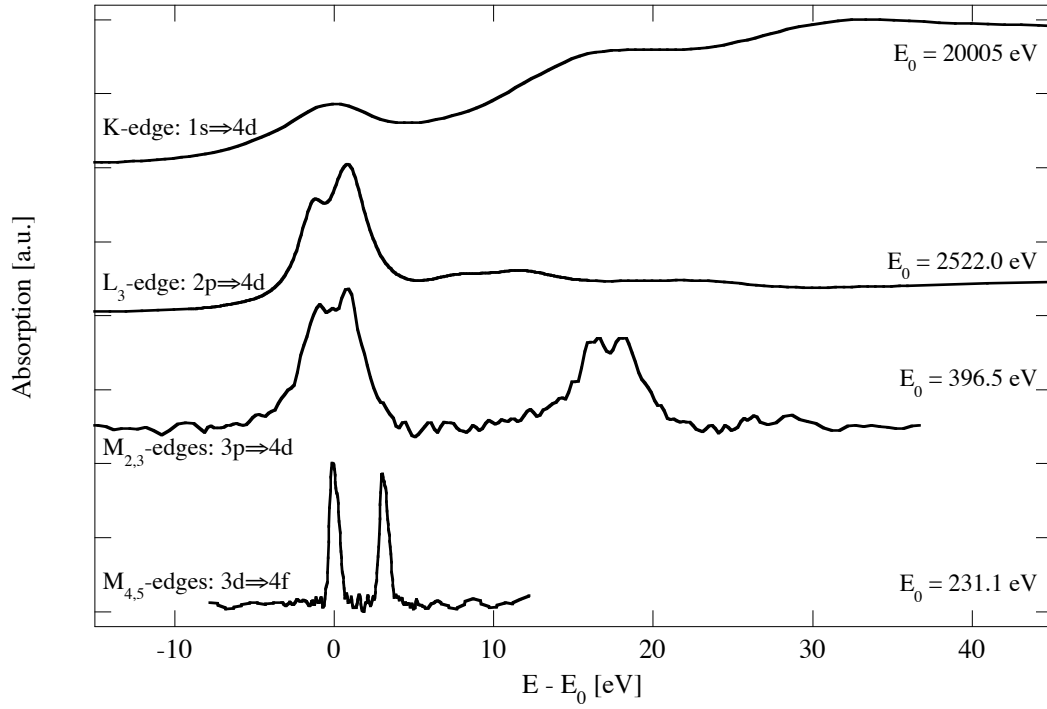


Figure 44: A comparison of the molybdenum fluorescence detected absorption K, L, and M-edges for the model compound Na_2MoO_4 . Note the narrow linewidths of the $\text{M}_{4,5}$ -edges.

width because of the longer core hole life time. However, note that the molybdenum $\text{M}_{2,3}$ -edges are hardly narrower than the molybdenum $\text{L}_{2,3}$ -edges, although the former are factor > 6 lower in energy. This is because Coster-Kronig transitions, i.e. transitions from a higher-energy sub-shell with the same principal quantum number, are very fast. They provide a fast decay channel of the molybdenum $3p_{\frac{1}{2}}$ and $3p_{\frac{3}{2}}$ core holes that broadens the molybdenum $\text{M}_{2,3}$ -edges, while they are not available as a decay channel at the $\text{L}_{2,3}$ -edges. Table 2 shows calculations of radiative and non-radiative yields and level widths for molybdenum M-edges. The fast Coster-Kronig transitions, which dominate the decay of the molybdenum $3s$, $3p_{\frac{1}{2}}$, $3p_{\frac{3}{2}}$ core holes, lead to the larger $\text{M}_{1,2,3}$ -edge level widths. A comparison of these numbers for the K through N_3 -edges of molybdenum reveals

Sub-Level	M ₁	M ₂	M ₃	M _{4,5}
Level Width [eV]	7.18	2.67	2.69	0.157
Core Hole Lifetime [ps]	0.096	0.26	0.25	4.38
Auger Yield	0.030	0.084	0.081	0.997
Coster-Kronig Yield	0.988	0.916	0.919	0
Fluorescence Yield	9.5×10^{-5}	2.0×10^{-4}	1.9×10^{-4}	3.5×10^{-4}

Table 2: Calculated molybdenum M-edge radiative and non-radiative M-edge yields and level widths for molybdenum. (Linear interpolation from tables [McGuire 72a, McGuire 72b].)

that the M_{4,5}-edge are narrowest and thus offer the highest sensitivity to chemical changes.

For the chemical analysis of dilute molybdenum compounds like the M-center in nitrogenase, the advantage of narrow edge width and consequently high chemical sensitivity needs to be weighed against the fact that the fluorescence yield (table 2) is much lower for these lower energy edges. That reduces the sensitivity for analyzing dilute samples. The preponderance of Coster-Kronig transitions does somewhat mitigate the low fluorescence yield when studying molybdenum, since a fast Coster-Kronig transition can still be followed by a fluorescence decay. As an illustrative example, consider molybdenum 3s vacancies, which relax 99% by Coster-Kronig transitions, with 70% of those producing vacancies in the $3p_{\frac{1}{2}}$ and $3p_{\frac{3}{2}}$ levels. The fluorescence yield of the $3p_{\frac{1}{2}}$ and $3p_{\frac{3}{2}}$ core holes is twice that of M₁. These $3p_{\frac{1}{2}}$ and $3p_{\frac{3}{2}}$ vacancies again predominantly decay through Coster-Kronig transitions. This nearly equalizes the effective fluorescence yields of the M-edges, and causes the molybdenum M_ζ (after [Bearden 67]) line at 193 eV to always be the strongest molybdenum M-emission line in the XRF spectra, even for excitation at the M_{1,2,3}-edges.

Figure 45 illustrates the trade off between effective fluorescence yield and relative edge width. The fluorescence yield is plotted along the y-axis and determines the elemental

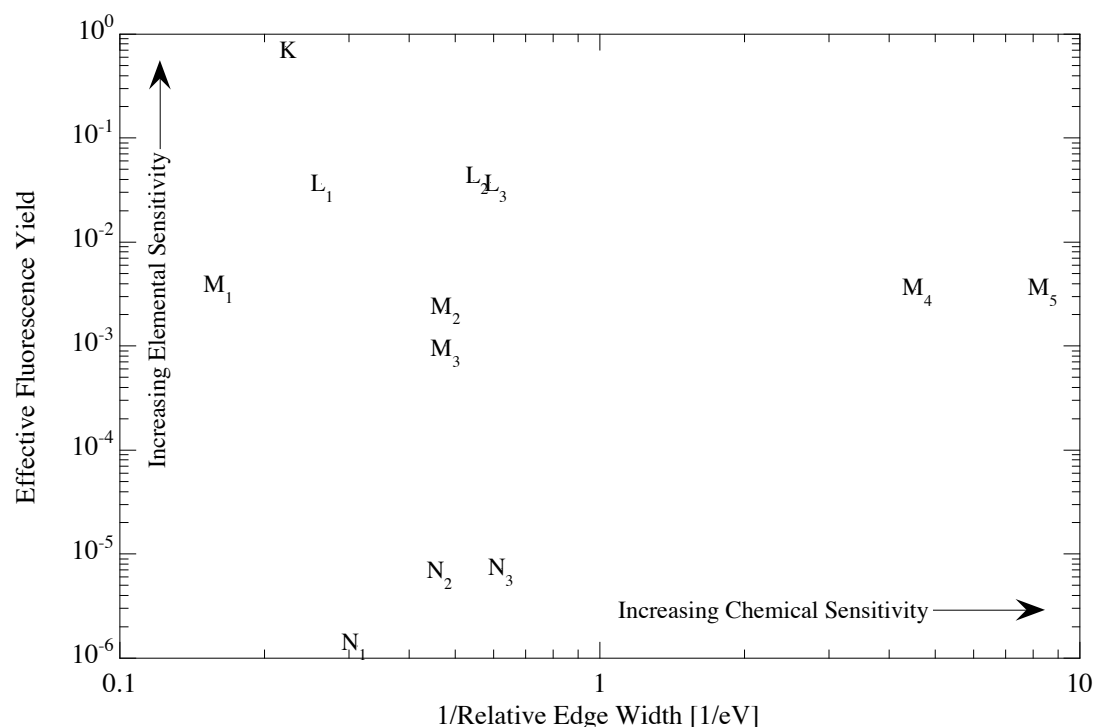


Figure 45: The trade-off between elemental sensitivity and chemical sensitivity is illustrated by this plot. The greater the fluorescence yield, the greater the elemental sensitivity. Chemical sensitivity, obtained by multiplying the relative edge width by the chemical shift, is greatest for narrow edge widths and large chemical shifts.

sensitivity of fluorescence-detected XAS measurements because it (and the spectrometer efficiency) sets the fluorescence signal strength. To determine chemical sensitivity, the relative edge width is multiplied by the chemical shift per change in oxidation state and plotted along the x -axis. A typical K-edge shift between Mo(0) and Mo(VI) is 10 eV, while the $L_{2,3}$ -edge shifts are 6 eV and $M_{2,3,4,5}$ -edge shifts are 2.5 eV for the same range of oxidation states [George 90]. For molybdenum, the most precise edges for chemical analysis are the $M_{4,5}$ -edges, provided the spectrometer efficiency is adequate to take the measurement despite the low fluorescence yield. Here we examine the question how much information we can extract from these low-energy molybdenum M-edges.

We have taken absorption spectra by total electron yield at the $M_{2,3}$ -edges and $M_{4,5}$ -edges for different model compounds containing molybdenum in oxidation states from 0 to 6. All the samples were fine powders on carbon tape, except for the elemental molybdenum, which consisted of a 2000 Å film sputter deposited on a silicon substrate and capped with 20 Å sputter deposited silicon to prevent oxidation. Air sensitive samples were prepared in a high-integrity anaerobic glove box with less than 0.2 ppm oxygen. The $M_{2,3}$ spectra (Figure 46) were calibrated relative to the absorption edge of NaMoO_4 , and exhibit a systematic shift of the absorption edge to higher energy for higher oxidation state. This is expected since the electron density at the molybdenum atom is reduced for higher oxidation state, which reduces screening of the core levels and thus increases their binding energy. Figure 47 summarizes the shifts in the energy of the M_3 -edge versus oxidation state. Note that the edge shifts are much stronger for the hard ligands oxygen, chlorine and bromine than for the soft ligand sulfur, because the Mo–S bond has a more covalent character. These edge shifts can be used to determine the molybdenum oxidation state in unknown compounds, provided molybdenum is known to be bound to hard ligands.

Figure 48 summarizes the absorption spectra at the molybdenum $M_{4,5}$ -edges. They confirm the narrowness the $M_{4,5}$ -edges and also show large shifts with molybdenum oxidation state (cf. Figure 49). Surprisingly, the $M_{4,5}$ -edge energies are higher for MoO_2 and MoCl_3 than for Na_2MoO_4 , despite the fact that their formal oxidation state is lower and both oxygen and chlorine are hard ligands. These results were reproducible at different beam times, and the Na_2MoO_4 calibration sample was run immediately after the MoO_2 and MoCl_3 samples. At present, we do not understand the high absorption edge energy measured for MoO_2 and MoCl_3 , and suspect that the source material was not as pure as

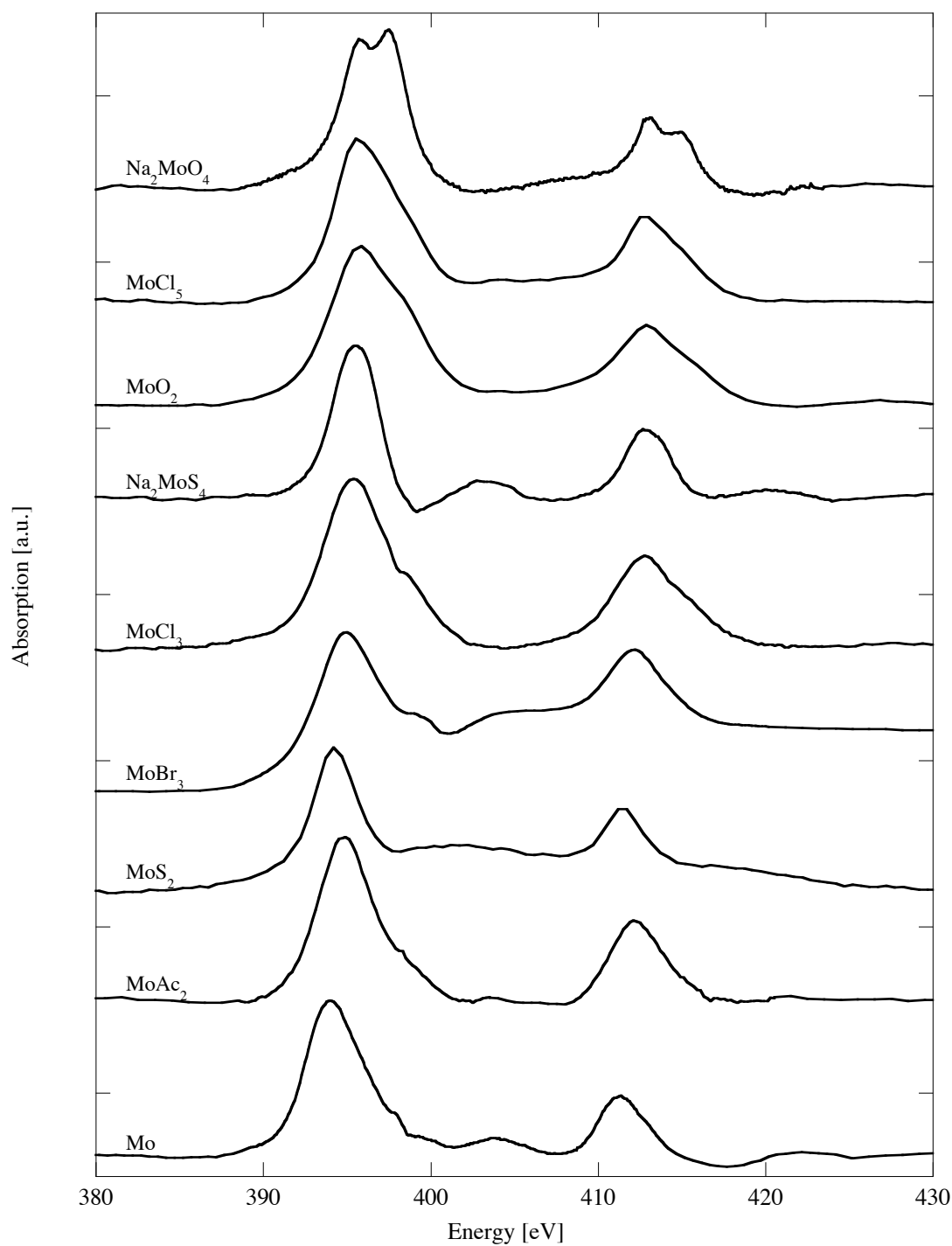


Figure 46: Molybdenum model compound $M_{2,3}$ -edge spectra covering oxidation states from Mo(0) to Mo(VI).

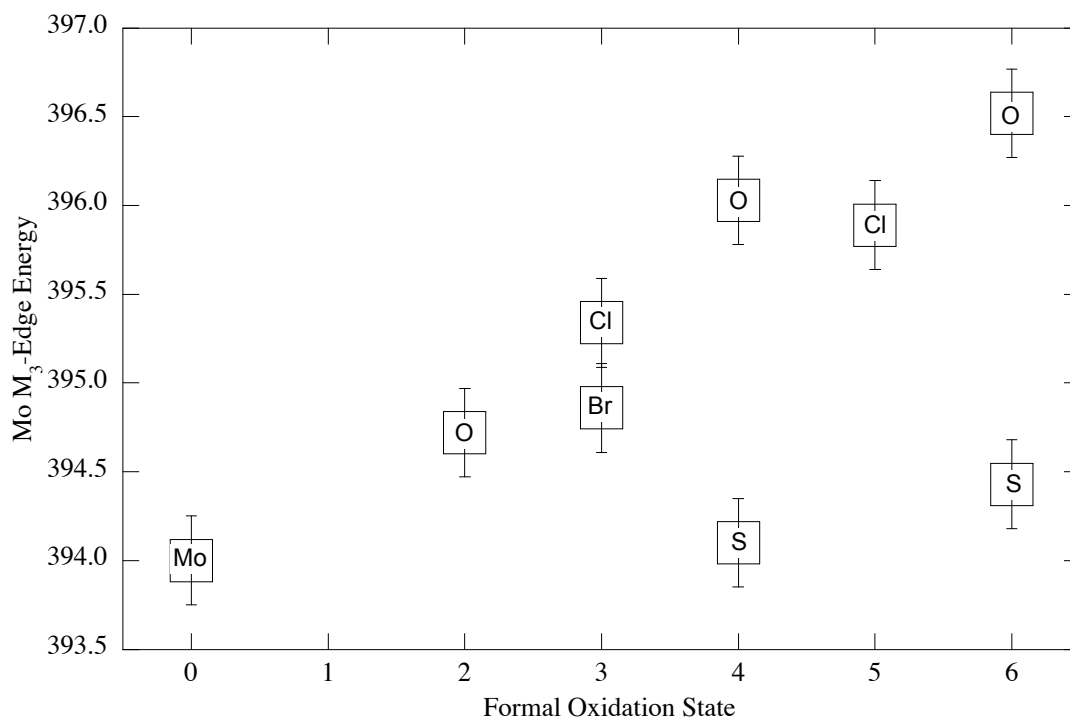


Figure 47: Molybdenum M₃-edge shift comparison. The edge shift vs oxidation state is stronger for hard ligands.

expected.

XAS on the molybdenum M-edges using total electron yield is comparably straightforward. Unfortunately, total electron yield (TEY) is surface sensitive, and many biological samples have degraded properties at the surface. This always casts some doubt on whether the data are representative of the system in a biologically relevant state. Partial fluorescence yield (PFY), which examines a sample over the photon absorption length of $\sim 1 \mu\text{m}$ from the surface, is therefore preferred. PFY measurements also tend to have higher sensitivity, provided an X-ray detector is used that can separate the fluorescence line of interest from the matrix background and thus greatly reduce the background signal.

For molybdenum, the strongest M-fluorescence lines are around 195 eV and 330 eV,

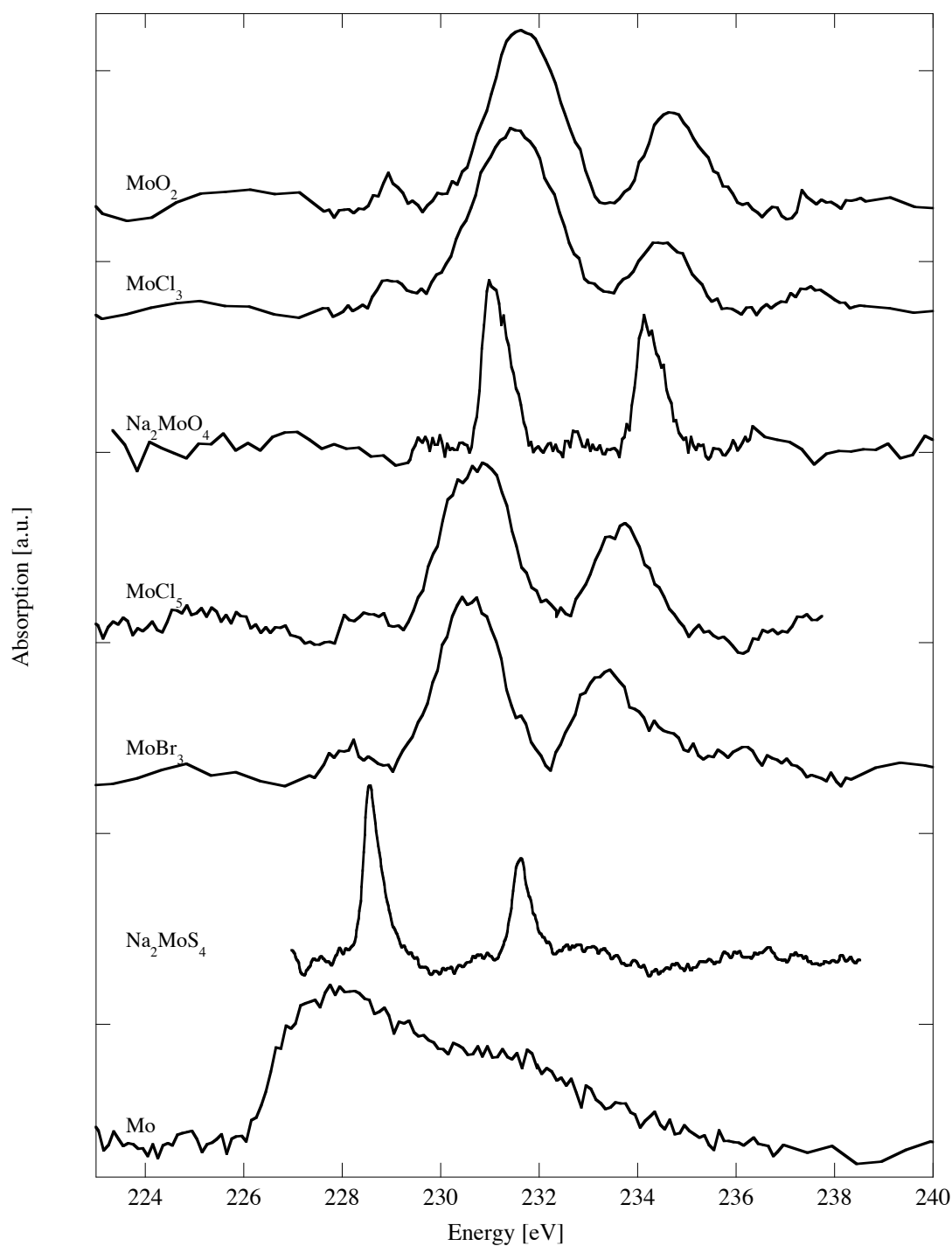


Figure 48: Molybdenum model compound $M_{4,5}$ -edge spectra covering oxidation states from Mo(0) to Mo(VI). Note that these are weak signals on strong backgrounds and that substantial background corrections have been made. The weak peak structure for the elemental Mo sample is likely to be related to the interface between the Mo and a thin Si protective layer.

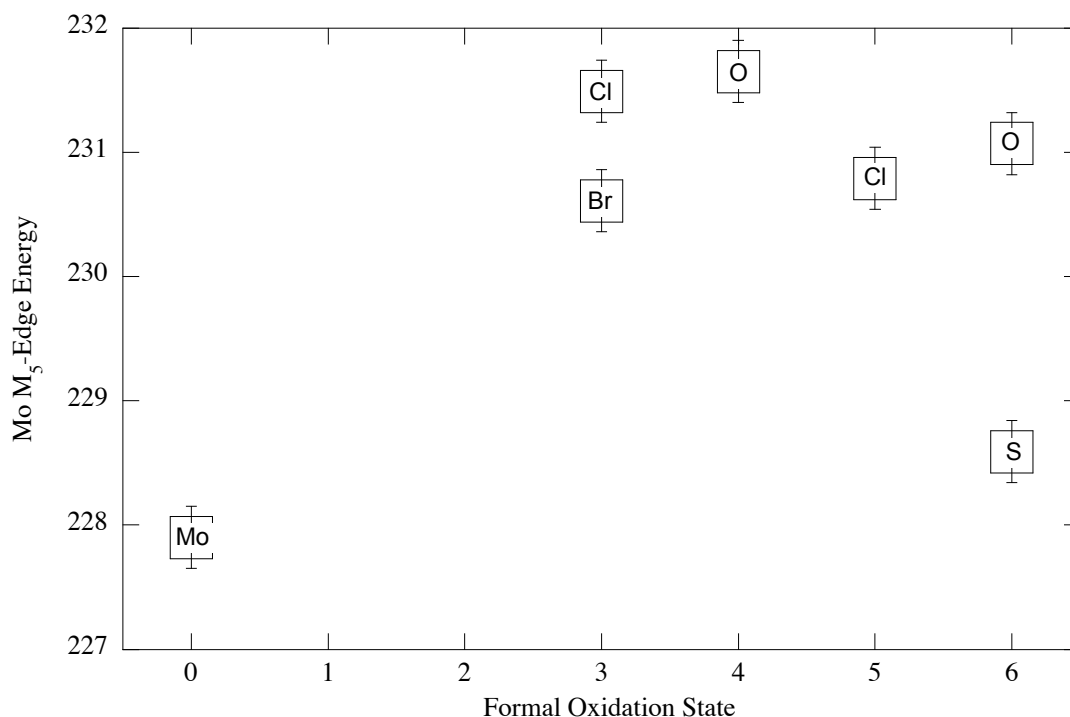


Figure 49: Molybdenum M₅-edge shift comparison. Here the trend is not clear as it is in Figure 47.

corresponding to the $4p \rightarrow 3d$ and $4s \rightarrow 3p$ transitions, respectively. STJ detectors do have the energy resolution to separate these lines from the carbon K, nitrogen K and oxygen K background fluorescence in biological samples. Figure 50 illustrates the advantages of STJs and the scientific problem. While the detector resolution is sufficient, the molybdenum M-fluorescence yields are very low, so that even concentrated molybdenum samples produce only small lines in the spectra. This makes details of the STJ response function important, because the background counts in the windows at the molybdenum fluorescence energies are determined by the percent-level artifacts from the stronger lines in the spectrum. The molybdenum M _{ζ} line at 195 eV lies on top of the surface layer artifact of the carbon K line at 277 eV, and the molybdenum fluorescence at 330 eV

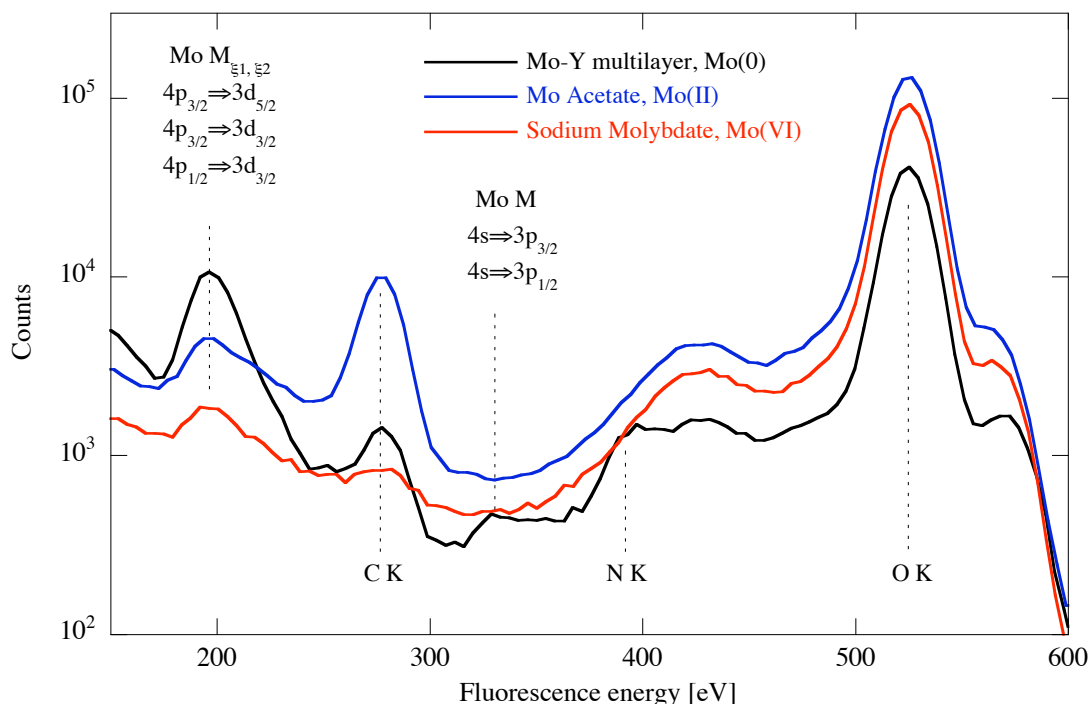


Figure 50: The XRF of three molybdenum compounds is shown. The carbon, nitrogen, and oxygen fluorescence peaks are clearly resolved. The low fluorescence yield of the lower energy molybdenum edge results in small peaks despite the high molybdenum concentration.

overlaps with the surface layer artifact of the nitrogen K line at 392 eV. Note that the fast Coster-Kronig transitions, which convert $3p$ vacancies into $3d$ vacancies with lower binding energy but higher fluorescence yield, always cause the M_{ξ} line at 195 eV to be the strongest molybdenum line in the XRF spectrum, even for $M_{2,3}$ -edge scans or excitation at higher energies (Figure 50). The Coster-Kronig transitions thus cause the appearance of additional X-ray emission lines that can be gated on and that provide an alternative measure of the X-ray absorption in cases where the higher-energy emission is obscured by nearby characteristic fluorescence of the matrix background.

We have then examined if the sensitivity of the STJ spectrometer is sufficient to analyze the molybdenum site in the iron–molybdenum cofactor of nitrogenase, which is $\sim 10\%$

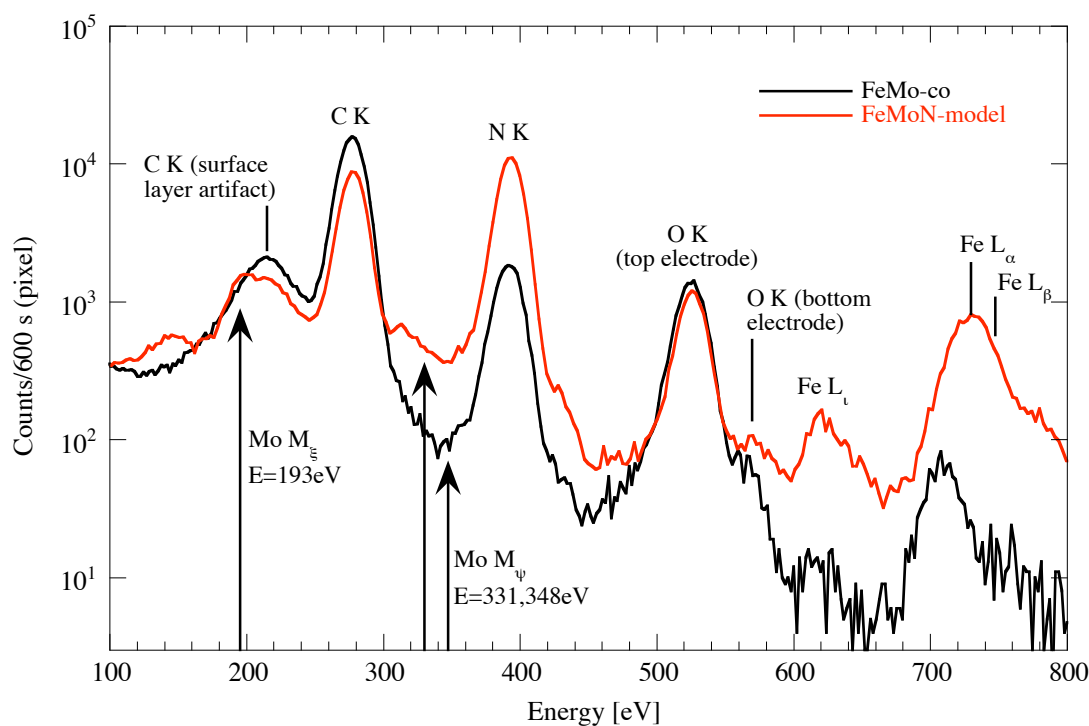


Figure 51: X-ray fluorescence spectra of FeMo-co and Mo-N-Fe mixture of model compounds. These spectra were acquired by a single STJ pixel over 600 s—roughly equivalent to a 15 s acquisition from a 36-pixel detector.

molybdenum in its pure form. These scans have, unfortunately, revealed no trace of an absorption edge whatsoever. The X-ray fluorescence spectra of FeMo-co for excitation at 520 eV show the likely explanation, especially when compared to the XRF spectrum of a Mo-Fe-N mixture of inorganic model compounds with nominally identical Mo, Fe and N concentrations (Figure 51). The spectra were acquired with a single STJ pixel for an acquisition time of 600 s, which is roughly comparable to the spectrum of a 36-channel STJ spectrometer for an acquisition time of 15 s per energy step. However, even under these conditions the molybdenum M-fluorescence from the model compound is barely visible, and it is not visible at all from the FeMo-co. The molybdenum concentration in the FeMo-co sample is seen to be at least an order of magnitude lower than expected, and

attempts to observe a molybdenum M XAS signal above the background were therefore unsuccessful. At an energy of 193 eV, corresponding to the molybdenum M_{ζ} fluorescence, this background is set by the spectral artifact associated with carbon K-fluorescence absorbed in the surface layer on top of the STJ (cf. section 2.4.1). At the energies of 330 eV and 350 eV, the background is set by the low energy tail of the nitrogen K-fluorescence. These artifacts in combination with the extremely low fluorescence yield ($\sim 10^{-4}$) of the molybdenum M-transitions and the lower-than-expected molybdenum concentration currently make fluorescence detected XAS on FeMo-co impossible even after the upgrade of the STJ spectrometer to 36 channels.

If at all possible, STJs would be essential for any fluorescence detected XAS on molybdenum M-edges, since gratings have even lower detection efficiency, and germanium detectors would not be able to separate the molybdenum fluorescence emission from the carbon and nitrogen background. While the energy resolution and count rate capabilities of STJs are sufficient for the proposed measurements, current 36-pixel arrays do not cover a sufficiently large solid angle to capture enough molybdenum fluorescence from FeMo-co to do the XAS measurements in an acceptable time. With the current experimental setup, the sensitivity is of order 10% for PFY XAS on molybdenum M-edges and other elements with a fluorescence yield in the range of 10^{-4} , and therefore not higher compared to TEY measurements. The sensitivity is limited by spectral artifacts and by the finite solid angle coverage. However, in contrast to Si(Li) and Ge detectors, STJs need not necessarily have such an artifact, since there is no intrinsic dead layer from the electrode. There is therefore no fundamental reason that would prevent building STJs where the spectral background is reduced well below the intensity of the molybdenum M-fluorescence, although the practical

engineering challenges may be formidable. We estimate that a future 112-channel STJ array with a purely Gaussian response function would extend the sensitivity to $\sim 0.1\%$. This will be discussed in more detail at the end of section 3.2.

While M-edge XAS on dilute molybdenum compounds such as FeMo-co are currently not possible, XAS on dilute elements with higher fluorescence yield such as nitrogen and iron are very much possible. They will be the subject of sections 3.3 and 3.4.

3.2 Sulfur L-Edge Spectroscopy

Sulfur is one of the essential elements of life. It is contained in the naturally-occurring amino acids methionine and cysteine, and plays a crucial role in defining the structure of many proteins by forming disulfide bonds between cysteine residues. Inorganic sulfur plays a key role in the iron–sulfur clusters which play a variety of biochemical roles both as electron transfer centers, such as in the ferredoxins, and as catalytic sites, such as in the enzyme aconitase [Beinert 83]. The iron–molybdenum cofactor is also a complex molybdenum-iron-sulfur cluster. In all these centers sulfur plays a crucial role. In electron-transfer, X-ray spectroscopy has shown that for iron–sulfur cluster reduction, more than half of the added electron density resides in molecular orbitals with sulfur character suggesting that much of the redox chemistry is in fact ligand based. Similarly, in catalysis, DFT calculations suggest that protonation of iron–sulfur sites occurs at the inorganic sulfur sub-sites. It is therefore desirable to analyze the sulfur chemistry of nitrogenase, particularly if it can provide information about sulfur metal bonding complementary to XAS of the metal site, and thereby probe the electronic and structural changes to the active

site during the catalytic cycle.

Absorption spectroscopy of sulfur samples has traditionally been somewhat awkward since the sulfur K-edge at 2.5 keV lies at an energy that used to be below the low-energy cutoff of typical hard X-ray beam lines, and above the high-energy cutoff of most soft X-ray beam lines. Even now, many of the soft X-ray beam lines such as BL 4.0.2 at the ALS where the STJ spectrometer is operated do not extend to the sulfur K energies. Nevertheless, sulfur K-edge spectroscopy has proved to be a powerful probe of the sulfur chemical environment, and hence, there is considerable interest in examining if the much lower sulfur L-edges can be used to extract chemical information. Not only are the spectral features expected to be substantially sharper than at the K-edge, but they are also expected to have better defined chemical shifts. Another advantage is that sulfur L-edge spectra can be taken on the same sample at the same soft X-ray beam line as the transition metal L and M-edges and light-element K-edges, and can therefore provide complimentary chemical information on the same chemical bond.

Fluorescence-detected sulfur L-edge spectroscopy cannot be performed with conventional Ge detectors because the very low fluorescence energy of ~ 145 eV lies within their baseline noise. STJ detectors, on the other hand, operate comfortably in that energy range. Figure 52 shows the cumulative fluorescence spectra a Na_2MoS_4 sample mounted on carbon tape, acquired with three STJ pixels located on different chips (fabricated together on the same wafer) during a sulfur L-edge scan from 155 eV to 180 eV (gray shaded area). The spectra of the first half of the scan are shown in blue, and the second half is shown in red, so that the contribution of the scattered beam (which changes during a scan) can be separated from the contributions of the fluorescence lines (which stay constant). Although

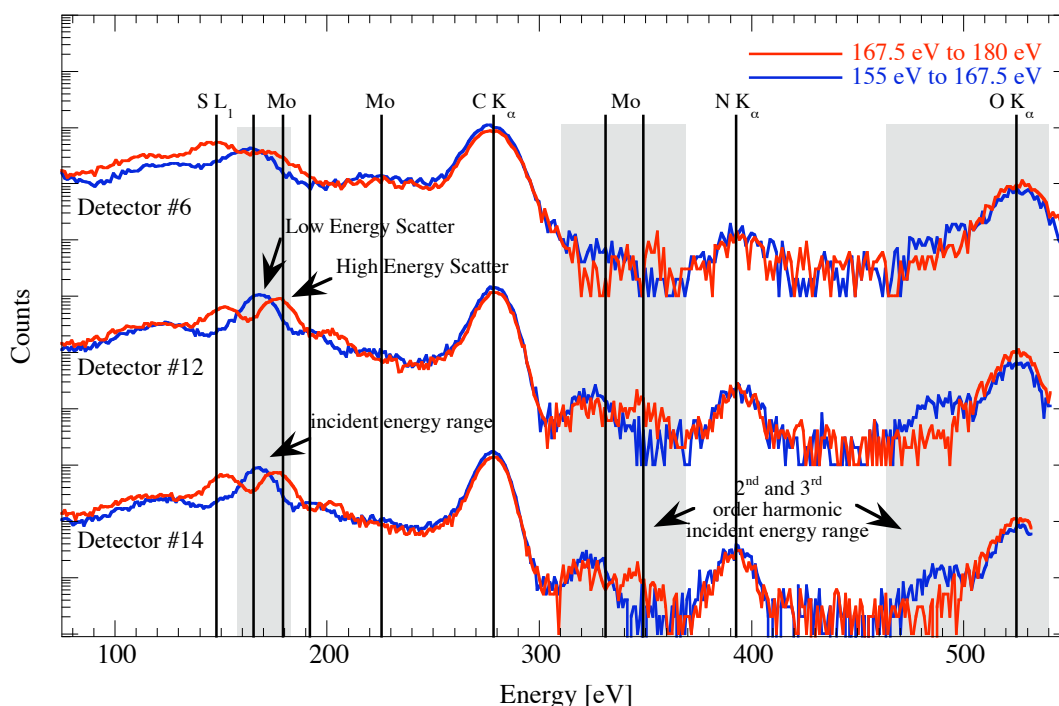


Figure 52: Na_2MoS_4 Fluorescence Spectra taken from three pixels. The spectra for each incident energy of the first half of the scan (155 eV to 167.5 eV) are summed (MCA bins) and superimposed on those of the last half (167.5 eV to 180 eV). Since characteristic lines have a fixed energy, scatter can be recognized by a shifting peak. The gray areas indicate regions where scatter will be observed.

the maximum incident energy during this scan is nominally only 180 eV, the light elements carbon, nitrogen and oxygen are all excited by the higher harmonics of the incident beam.

These higher harmonics can actually be observed directly in the spectra, since they are also scattered into the detector at twice and three times the incident energy (second and third gray shaded areas). Note that the intensity of the carbon K line decreases during the scan since carbon is excited less efficiently, while the oxygen K fluorescence intensity increases in the second half of the scan as the third harmonic crosses the oxygen K-edge. The sulfur L-fluorescence can be seen at ~ 145 eV as expected, although it is significantly weaker than the carbon K-fluorescence despite the fact that carbon is only excited by the higher

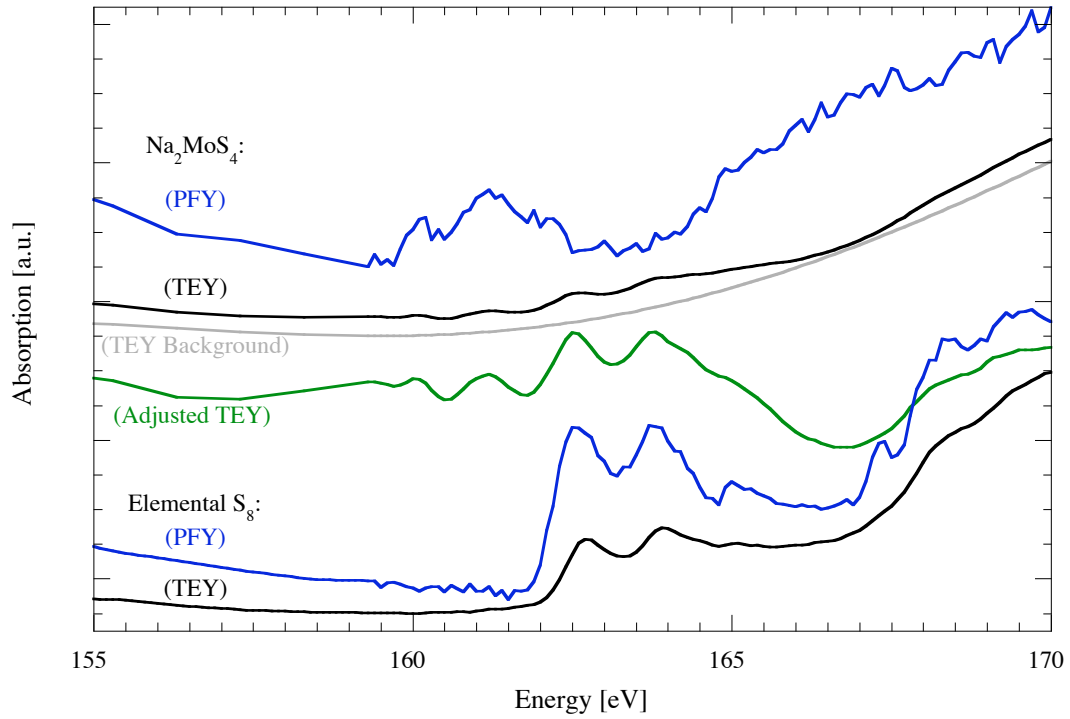


Figure 53: Raw Sulfur $L_{2,3}$ -edges. The energy is calibrated by setting the L_3 -edge of elemental sulfur (S_8) to the literature value of 162.5 eV. The PFY and TEY spectra are normalized by I_0 . The adjusted TEY spectrum is calculated by subtracting a fourth-order polynomial fit (TEY background). Both the PFY and TEY data were acquired during the same scan.

harmonics and great care was taken to cover the entire carbon tape with the Na_2MoS_4 sample. It is also not surprising to see line overlap with the elastically scattered incident beam, since its energy difference with sulfur L is very small and the four 3×3 pixel STJ arrays cannot all be at the ideal angle of 90° where the scatter is minimized. Note that there is less scatter in STJ pixel #6, indicating that this particular pixel is held at an angle closer to 90° with the incident beam than the other two pixels in Figure 52.

When gating on the sulfur L-lines to extract the absorption spectrum, the two sulfur L-edges are clearly visible even in the raw PFY spectra, especially when compared to the total electron yield data (Figure 53). In fact, the first time we took sulfur L-edge spectra

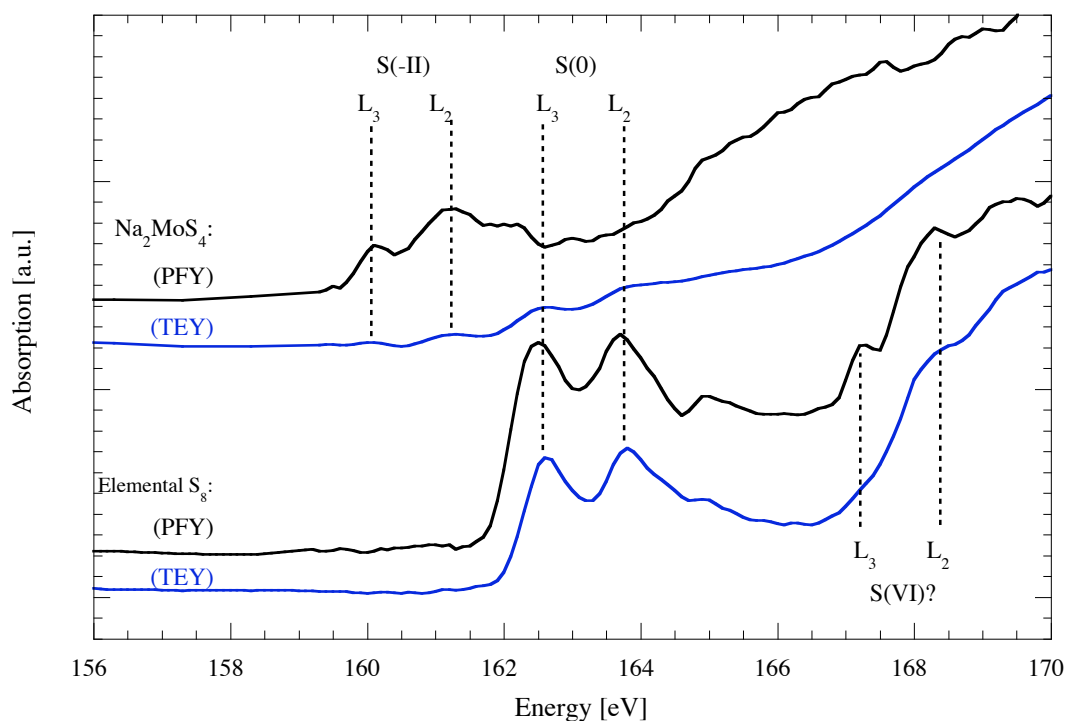


Figure 54: Normalized Sulfur $L_{2,3}$ -edges. The energy has been. The PFY and TEY spectra are normalized by I_0 and a linear background has been subtracted.

by TEY, the assignment of the edges was almost impossible, and could be understood only after the PFY spectra with the STJ detector became available. This is partially because the sulfur L-edges are weak and can be masked by significantly larger charging effects and lower energy effects. Also, TEY spectra are surface sensitive, and partial oxidation or reduction at the surface can produce additional peaks of similar magnitude as the main edges with chemical shifts that are comparable to the line splitting and that depend sensitively on sample preparation.

This is illustrated in Figure 54 that shows the same spectra after processing. They were normalized by I_0 , a linear background was subtracted, three scans were averaged and the energy was calibrated by setting the peak of the L_3 -edge of elemental sulfur to

the literature value of 162.5 eV. The $L_{2,3}$ -edges are separated by ~ 1.1 eV as expected, and their edge width is only ~ 0.5 eV. To measure chemical shifts in sulfur, we have also taken XAS spectra on Na_2MoS_4 where sulfur exists in a nominally S(-II) oxidation state (Figure 54, top traces). The lower energy peaks at 160.1 eV and 161.2 eV can now be identified as belonging to the S(-II) species, with an energy shift of ~ 1.2 eV per oxidation state compared to S(0). Interestingly, the TEY spectra of Na_2MoS_4 still show clear peaks at 162.5 eV and 163.6 eV, while the bulk-sensitive PFY spectra do not. This indicates that a certain fraction of the sulfur has formed elemental S(0) at the surface, either during sample preparation or on exposure to vacuum. On the other hand, the two sulfur L-edges in Na_2MoS_4 appear split into two peaks that are separated by ~ 1 eV, which is comparable in magnitude to the $L_{2,3}$ -edge separation. This splitting is more noticeable at the higher-energy L_2 -edge, and causes the small peak at 162.2 eV. The splitting also affects the lower-energy L_3 -edge, and causes the L_2 -edge to be larger than the L_3 -edge. It is likely caused by the interaction of the sulfur levels with the electronic structure of the molybdenum that they are bound to, given that molybdenum in high oxidation states can show an edge splitting of comparable magnitude (cf. section 3.1).

In addition, the PFY spectra on elemental S_8 exhibit two peaks at 167.2 eV and 168.3 eV, whose splitting of 1.1 eV agrees with the $L_{2,3}$ -edge spin-orbit splitting in sulfur and suggests that they originate from a highly oxidized sulfur species. Assuming a chemical shift of ~ 1 eV per oxidation state based on the difference between the L_3 -edges in S(0) and S(-II), we can tentatively assign the peaks at 167.2 eV and 168.3 eV to a S(VI) species, as would be formed in sulfate anions. Note that the edge shifts of more than 1 eV per oxidation state are twice as large as the sulfur L-edgewidth, thereby again validating the approach to

measure chemical shifts at these low-energy edges.

We have attempted to take sulfur L-edge spectra on an iron–sulfur cluster in FeMo-co to determine the average sulfur oxidation state in the active site of nitrogenase. Unfortunately, the S/N was too poor to extract any useful information. The S/N in the sulfur L-edge spectra of Na_2MoS_4 was about 20 for an average of three half-hour scans with a total of 30 s per energy step. While the nominal sulfur content of a pure dried FeMo-co sample is only about a factor of two less than for Na_2MoS_4 , measurements of the iron–nitrogen ratio in the sample show that the sample likely another factor three more dilute due to residual solvents (and possibly salts) used during sample preparation. Although disappointing, it is therefore not surprising that sulfur L-edge spectroscopy on FeMo-co is not (or at best marginally) possible with the current setup.

What then can be done to improve the sensitivity in this very low energy range to enable sulfur L-edge spectroscopy on FeMo-co and other biological systems with similar sulfur concentrations? Among the different possibilities, Figure 52 shows that the most significant gain of the current setup would arise from a reduction of the scattered beam. This requires all STJ pixels to be as close to 90° with the incident beam as possible. Since this cannot be done with four separate 3×3 pixel STJs on four separate chips, we are currently collaborating with the Institute of Physical High Technology in Jena, Germany, on the development of close-packed 36-pixel STJ arrays. The first of these close-packed STJ arrays have just been received as of this writing (Figure 55), and their X-ray response will be tested within the next weeks. The next important step would be to reduce the contribution of the X-ray lines excited by the higher harmonics of the incident beam. This can be done either by reducing the higher harmonics themselves, or by improving the

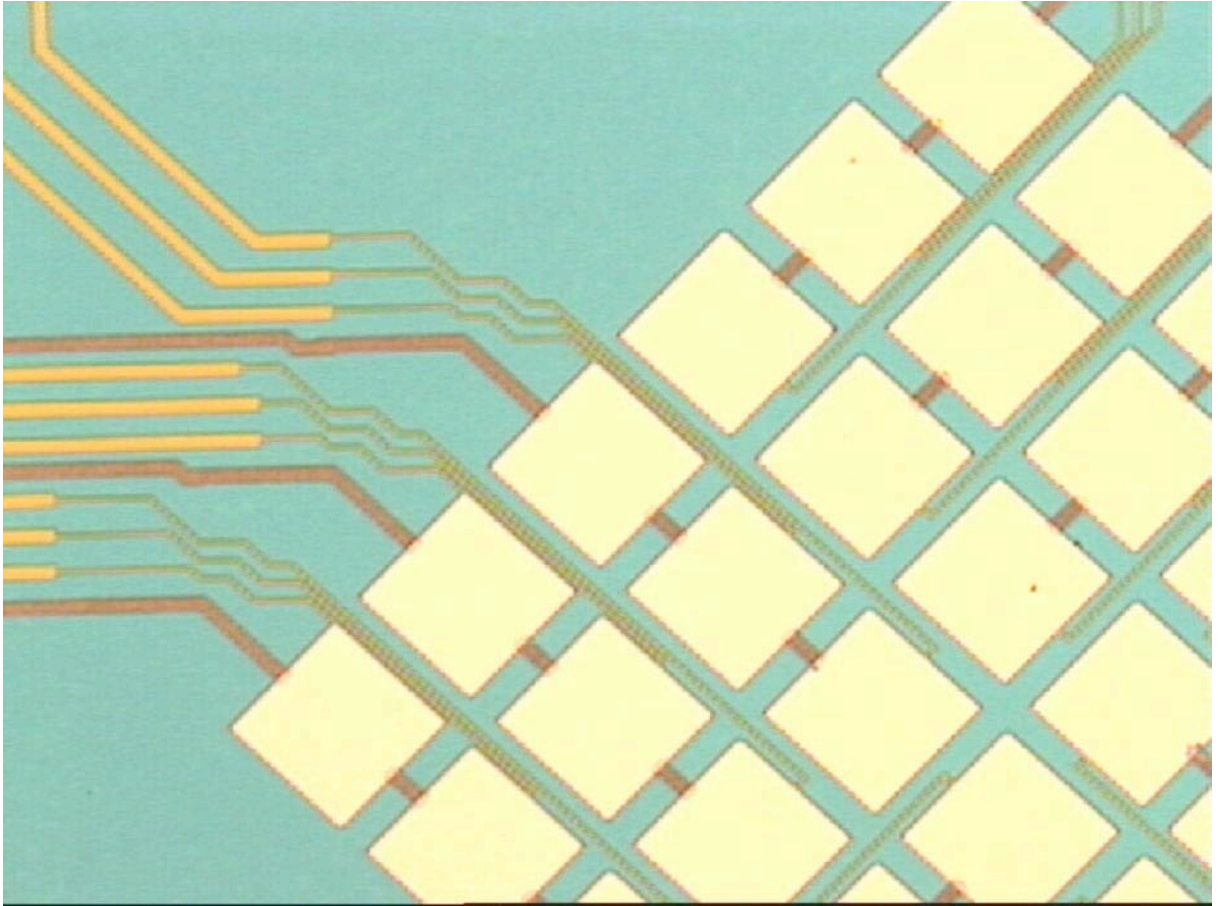


Figure 55: View showing the interconnect detail of the 36-Pixel Close-Packed Array STJ Detector.

response function of the STJ such that fewer counts of the excited lines leak down into the window of interest. In most beam lines, including BL 4.0.2, the spectral content of the higher undulator harmonics is not well suppressed. The incident beam can therefore contain a significant fraction of its intensity in the harmonics, about $\sim 10\%$ in the case of BL 4.0.2. It can be reduced with a pair of crystal mirrors whose critical angle lies somewhere between the first and second harmonic so that the first undulator harmonic is reflected while the higher harmonics are absorbed.

The alternative is to reduce the influence of these lower energy-excited X-ray lines by improving the spectral purity of the STJ response. Since (in the not untypical case

of FeMo-co) the interfering carbon K and sulfur L-lines are separated by 130 eV, an improvement in energy resolution is not required. Rather, it is important to further reduce the processes that cause carbon K X-rays at 277 eV to be mis-identified and produce counts in the sulfur L window around 145 eV. These artifacts of carbon emission are caused by a reduced response for X-ray absorption in a 20 nm surface layer of SiO₂ and hydrocarbons on the top niobium absorber film [Friedrich 05]. They can be suppressed in future devices by changing the mask layout and processing geometry (no residual SiO₂ over most of the STJ), by switching to tantalum-based STJs (no deep surface oxidation of niobium) and by keeping the STJs in a meticulously clean atmosphere between fabrication and mounting so that there is no hydrocarbon deposition. Note that these artifacts are only on the order of 1%, and therefore already much lower than the artifacts caused by the dead layer in semiconductor-based devices [Drury 05]. However, there is no fundamental reason for any such a surface layer in STJs, as opposed to semiconductor detectors that require an electrode layer over the entire active detector surface to apply a bias voltage.

Another interesting approach to increase the STJ spectrometer sensitivity could be to improve the X-ray transmission of the three IR-blocking windows between the sample and the detector. A search through the periodic table, and several discussions with Ed Graper at Lebow Company [Lebow06] with regards to manufacturability, indicates that palladium could potentially be well-suited as a window material, since its X-ray transmission peaks in the energy range around sulfur L (Figure 56), and it can be produced as thin free-standing films. Lebow Company has kindly provided such 50 nm thick free-standing Pd films, and we have measured their infrared transmission in the wavelength range of 300 K blackbody radiation. Unfortunately, its infrared transmission is extremely high, especially compared

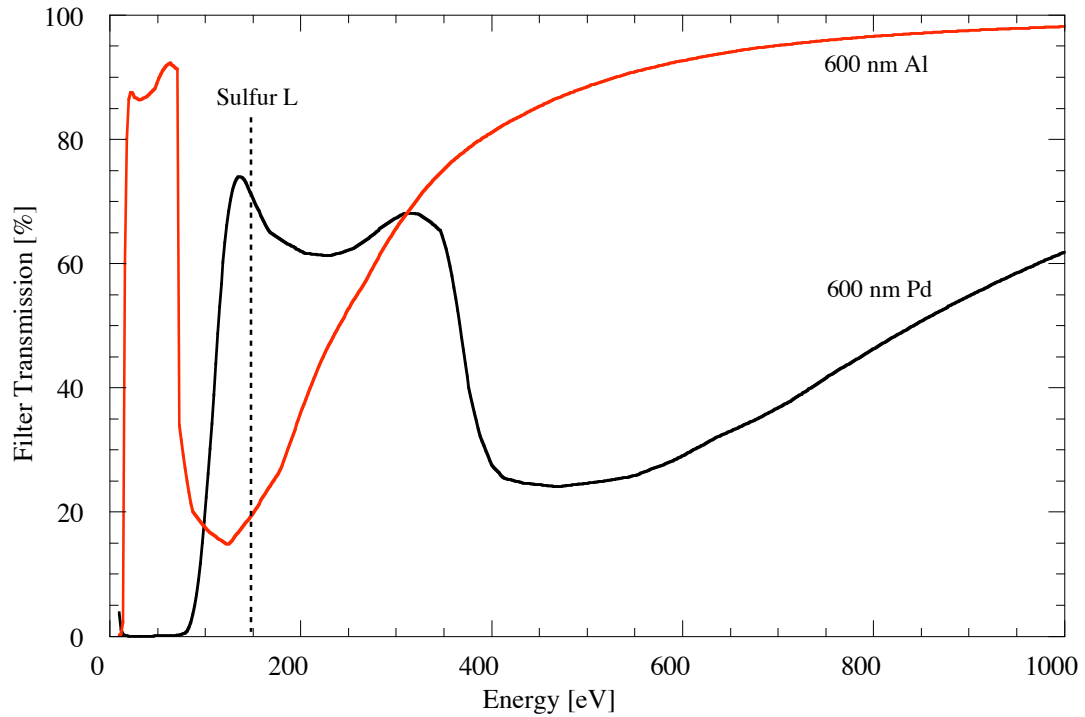


Figure 56: X-ray transmission of aluminum and palladium.

to Al that is used in traditional IR-blocking windows (at 500 1/cm, $\sim 0.7\%$ for Pd and $\sim 0.004\%$ for Al) (Figure 57), and precludes the use of Pd as a high-transmission window material for cryogenic detectors.

Since the size of individual STJ pixels is limited by Fiske mode resonances to $\sim 200\ \mu\text{m} \times 200\ \mu\text{m}$, further increases in spectrometer sensitivity can be made mostly with the brute-force approach of using larger arrays and placing them closer to the sample. We are therefore currently collaborating with the Paul Scherrer Institut in Viligen, Switzerland, on the development of 112-pixel Ta-based STJs that incorporate all the desirable design changes outlined above (Figure 58).

Placing these arrays any closer to the sample is difficult with the current spectrometer geometry, given that three IR-blocking windows are required between room temperature

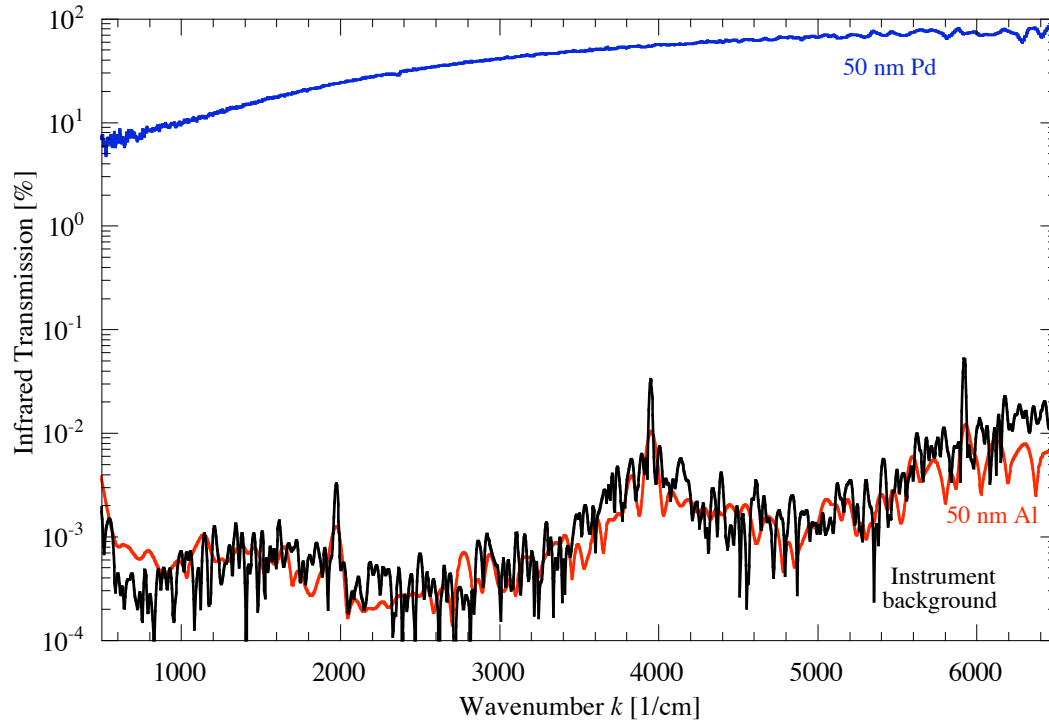


Figure 57: Infrared transmission of aluminum and palladium.

and the STJ at 0.1 K and that any distance less than 1 mm–2 mm between the windows makes the spectrometer prone to failure due to the differential cooldown of different materials and subsequent touches between different stages. One alternative possibility, albeit a rather drastic one that requires a new cryostat, would be to change the experimental geometry by removing cold finger, placing the STJ array inside the cryostat and inserting the sample next to it. The sample would be held at (or close to) 4 K so that only a single window would be needed in front of the STJ array. This could reduce the distance between sample and STJ from currently ~ 10 mm to maybe ~ 5 mm. The Advanced Detector Group has successfully used such a geometry in the past in the earlier experiments [Frank 98], but decided against it for the present STJ spectrometer to make it compatible with the existing L-edge chamber. Also, sample alignment with the beam has always been difficult with a

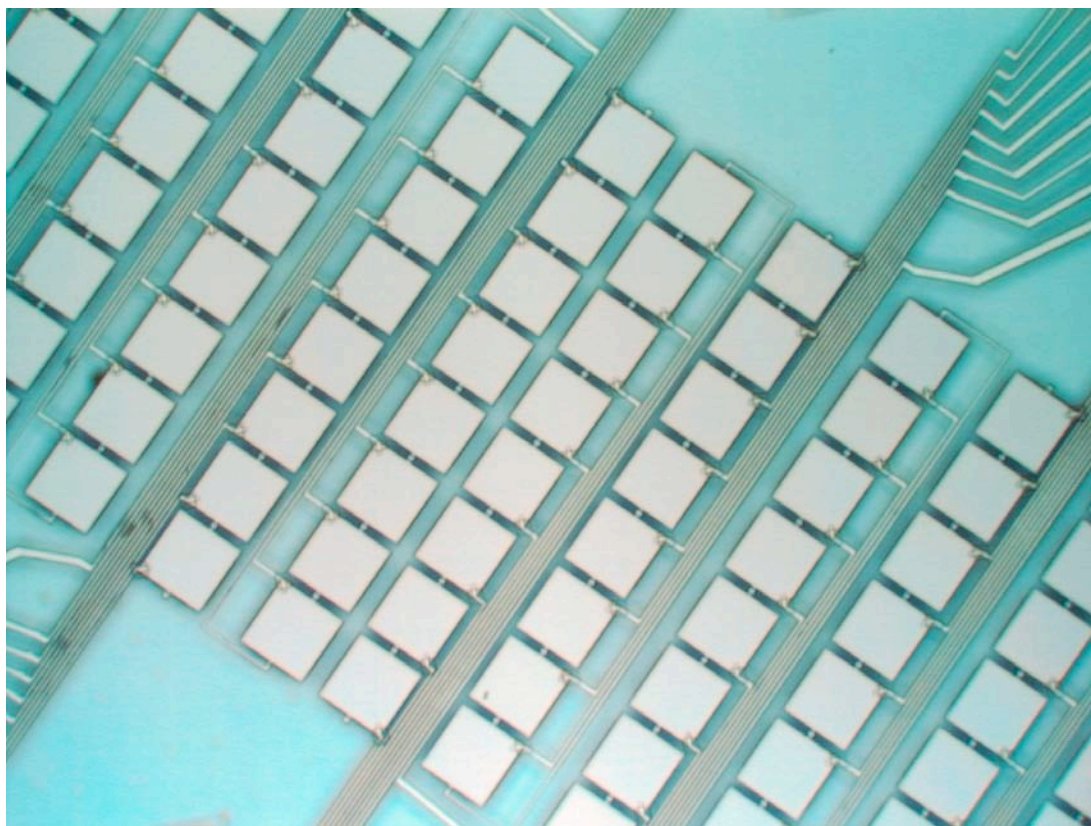


Figure 58: 112-pixel Ta-based STJs.

sample at 4 K that was not visible during alignment. Future cryostat designs need to take this into account.

We can roughly estimate the improvements in sensitivity that can be achieved in future detector upgrades. For a concentrated Na_2MoS_4 sample with a sulfur content of 47% by weight, the raw sulfur L-edge spectrum of in Figure 52 contains ~ 100 signal counts on top of ~ 5000 background counts for an acquisition time of 10 s per energy. Only 22 of the 36 STJ pixels were used in this scan because of limitations of the data acquisition electronics. An FeMo-co sample contains nominally 23% sulfur by weight could theoretically produce ~ 500 counts in 10 s with the same setup, although signal rate around 125 counts/10s is more realistic. If the new closed-packed 36-pixel STJ array can in fact reduce the

background counts due to scatter and surface artifacts to well below this rate—theoretically, this could be the case for perfect right-angle alignment—we would expect a statistics-limited S/N ratio of ~ 11 for the same setup, or ~ 14 if all 36 pixels could be read out. For a 112-pixel array, the S/N would increase to 25 for a 10 s/point data acquisition, and about 80 if 10 scans would be averaged. If this 112-pixel array were to be operated in a new cryostat where the sample can be placed within ~ 5 mm of the STJ, the solid angle coverage would increase by a factor 4 and the S/N ratio by another factor of 2 to about 160. In theory, this is quite achievable, provided that the influence of scatter and second order excitation can in fact be reduced as needed. In practice, our experience has shown that a factor 10 margin is desirable, but even then the experiment seems realistic. Improved STJ spectrometers could therefore enable sulfur L-edge spectroscopy on biologically relevant samples in the not-too-distant future.

3.3 Nitrogen Spectroscopy

One of the most interesting areas in current nitrogen fixation research is centered on whether FeMo-co contains a central interstitial light atom, and if so what element is it? The notion that a central light atom exists in FeMo-co was first suggested by high-resolution X-ray diffraction data of nitrogenase MoFe-protein single crystals [Einsle 02]. The experiments could not distinguish whether the central atom was a carbon, nitrogen or oxygen. Soon after, however, density-functional theory (DFT) calculations suggested that the most likely light atom inside the cluster would be nitrogen [Hinnemann 03]. This notion contradicts the previous general acceptance of an empty iron–sulfur cluster in FeMo-co

and chemists have been trying ever since to either corroborate or refute the hypothesis of “a well-defined cleft” by a “central ligand...most likely nitrogen” [Hinnemann 03]. Einsle et. al. had already suggested that the central atom was a nitrogen, and these authors had speculated that this atom may play a part in the catalytic cycle [Einsle 02]. Clearly identification of the atom is key to understanding the chemistry of the FeMo-co active site.

Soft X-ray spectroscopy offers a novel approach to studying this central atom—nitrogen K-edge spectroscopy. If this atom does in fact exist, and if it is a nitrogen as suggested by the DFT calculations a soft X-ray nitrogen K-edge study should show evidence of metal–ligand interactions. Moreover, this atom should exhibit a strong EXAFS signal because of the symmetric arrangement of the six heavy iron ligands and the more distant nine sulfur atoms of the cluster. Figure 59 shows a calculated (using the program FEFF [Rehr 00]) Nitrogen K-edge EXAFS spectrum for a hypothetical central nitrogen atom in FeMo-co. It is clear that the EXAFS should be clearly visible on the K-edge without detailed processing.

A major technical issue with measuring nitrogen K-edge spectroscopy on biological materials is the need to limit other nitrogen species in the sample. Hence nitrogen K-edge measurements on FeMo-co in nitrogenase protein samples are not possible, and measurements on the isolated cofactor are rendered difficult because the cluster is isolated in the solvent N-methyl formamide (NMF), which contains nitrogen. Our solution for this work was to collaborate with the group of Prof Barry Smith, John Innes Centre, Norwich, England. These workers after some experimentation, successfully exchanged cofactor isolated in NMF into a methanol/acetone mixture. In principle, this material should be free of any extraneous nitrogen atoms. Two samples of this material were available for soft

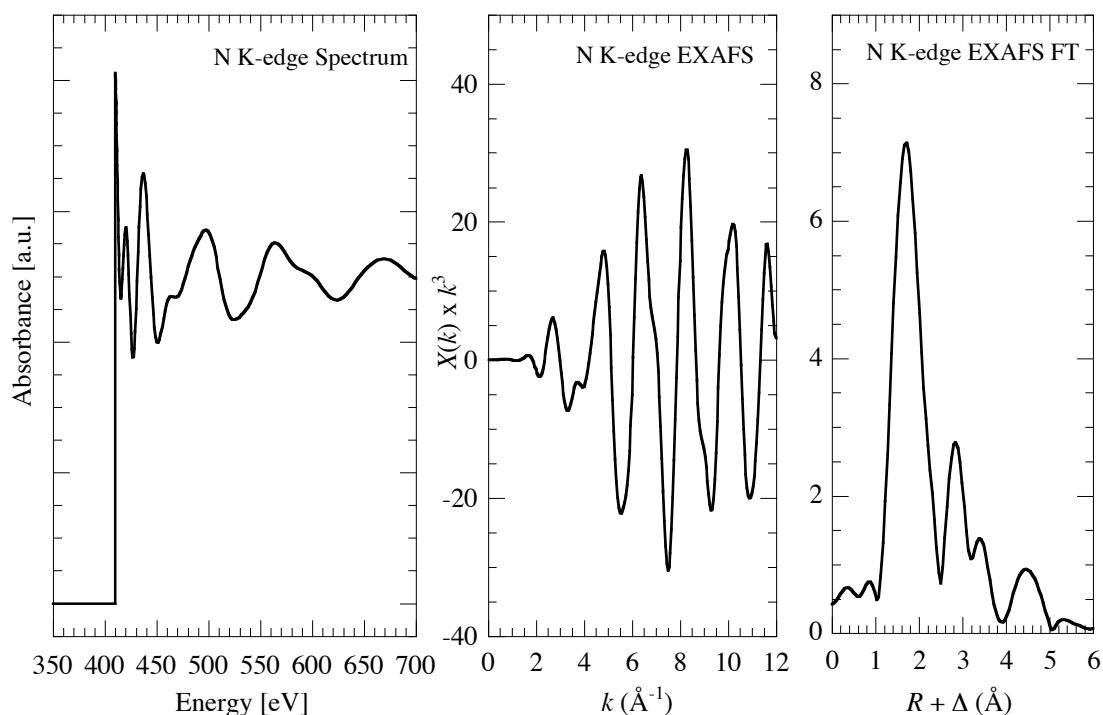


Figure 59: Calculated nitrogen K-edge EXAFS spectrum for a hypothetical central nitrogen atom in FeMo-co. (Left) K-edge, including the EXAFS region (middle) calculated k^3 -weighted EXAFS (right) Fourier transform.

X-ray studies with the STJ detector.

Another technical problem with measuring EXAFS on the nitrogen K-edges at ~ 400 eV is the crowded region which is complicated by the oxygen K-edge at ~ 540 eV. EXAFS relies on measuring small and decaying modulations in the absorption, which are easily swamped by the much stronger oxygen signal, part of which will leak into the energy window around the nitrogen emission at 392 eV. This typically limits the range of EXAFS measurements on nitrogen to an energy range of ~ 140 eV, and subsequently substantially limits the spatial resolution of the EXAFS Fourier transform. In the past, our group and our collaborators have successfully extended the range of EXAFS measurements across the absorption edge of other atoms by separately windowing on the fluorescence of interest

and the interfering fluorescence signal and subtracting a fraction of the interference from the fluorescence of interest [Gu 03, Yano 05]. This is somewhat easier to achieve for hard X-rays because the absorption edges of neighboring atoms are further apart and the leakage of the higher-energy fluorescence into the lower-energy window is less. On the other hand, it can in principle be easier to do such a subtraction when using an STJ detector rather than a semiconductor detector, because STJ detectors do not require a thin electrode over the active area whose dead layer is the primary source of low-energy tails on fluorescence lines in semiconductor detectors. The surface layer artifacts discussed in section 2.4.1 unfortunately limits the performance of our STJs at present, although the low-energy tail it causes is significantly weaker than that of Ge detectors in the soft X-ray range (Figure 29).

We have examined the feasibility of range-extended nitrogen EXAFS on the synthetically produced tetraphenylphosphine salt of the $[\text{Fe}_6\text{N}(\text{CO})_{15}]^{3-}$ cluster [Della Pergola 96]. Single crystal X-ray analysis of the equivalent tetramethyl ammonium salt shows that it possesses an octahedral metal cage similar to the iron–sulfur cluster in FeMo-co with an interstitial nitrogen ligand (Figure 60). All iron atoms are equivalent, each being bound to one bridging and two terminal carbonyls. Measurements on this model compound are more straightforward than on the FeMo-co active site, because aside from the nitrogen atom of interest inside the 6-Fe cluster it contains no other nitrogen atoms and, as it can be prepared to high purity. Also, it turns out that this compound is less affected by X-ray induced photochemistry than FeMo-co samples.

Figure 61 shows the fluorescence-detected XANES spectra on a $[\text{PPh}_4]_3[\text{Fe}_6\text{N}(\text{CO})_{15}]$ sample provided by Roberto Della Pergola. The spectra are interesting. They comprise a pre-edge structure with maxima at 398 eV and 402 eV, an edge maximum at 406 eV and the

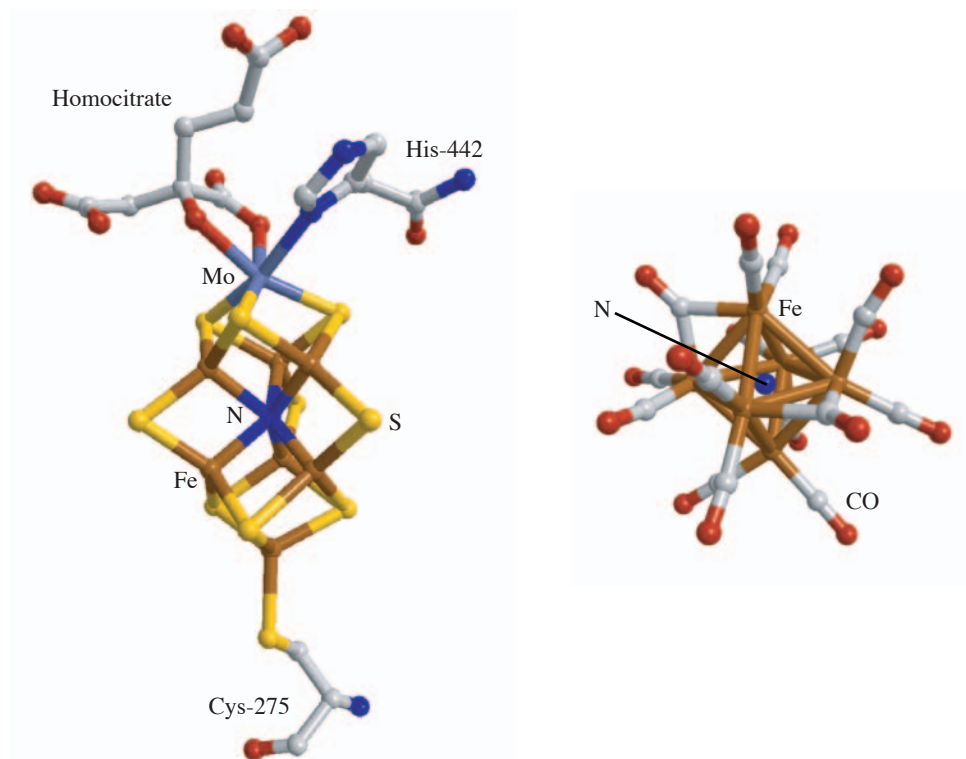


Figure 60: Ball-and-stick diagrams of FeMo-co (left) with an interstitial unknown element and $[\text{Fe}_6\text{N}(\text{CO})_{15}]^{3-}$ (right).

initial EXAFS structure is apparent at ~ 418 eV. The very strong split pre-edge structure is consistent with significant metal character in the N-bonding. The sample showed minimal radiation chemistry. The figure shows three scans from the same sample spot indicating the extent to which the sample changes for a total acquisition time of ~ 1.5 hours, roughly comparable to the time of a single range-extended EXAFS scan to an energy of 700 eV. The spectra show a small but systematic decrease of the pre-edge and edge peaks, which probably is a consequence of X-ray photolysis of the carbonyl ligands on the Fe-cage. However, there is no obvious change in the EXAFS peak at 418 eV within the noise of the experiment at that point (10%). This indicates that the bond lengths between nitrogen and its ligands and thus the structure of the molecule Fe-cage remains constant throughout the

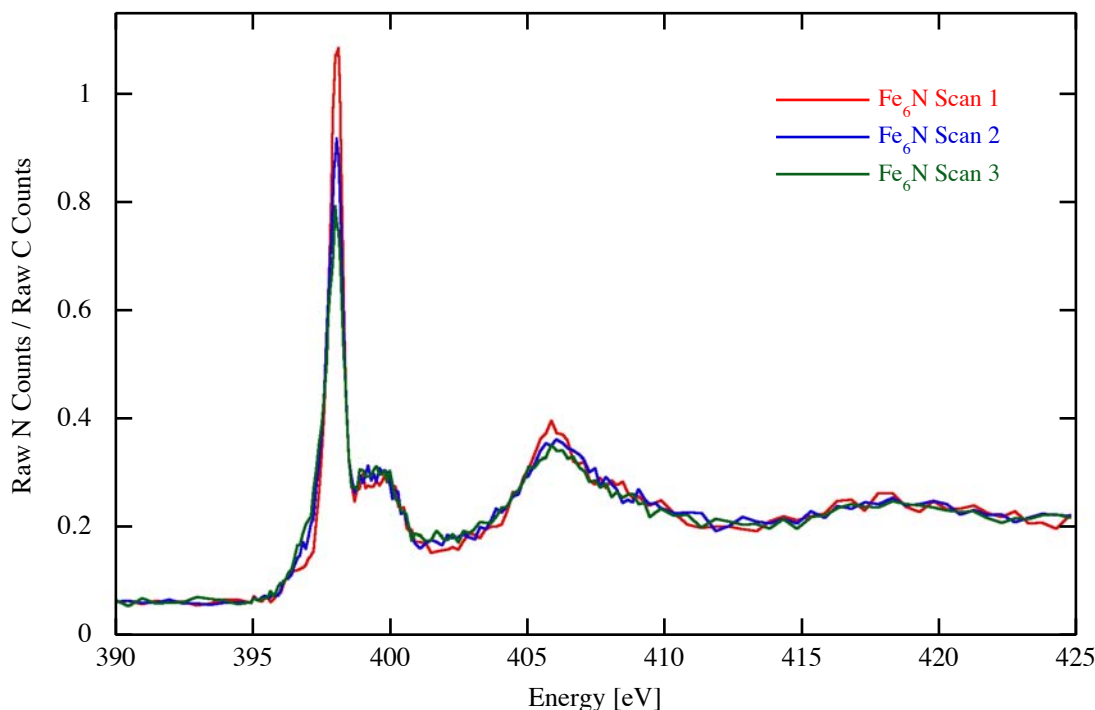


Figure 61: Three nitrogen XANES spectra of $[\text{PPh}_4]_3[\text{Fe}_6\text{N}(\text{CO})_{15}]$ on the same sample location to test sample stability under X-ray irradiation at the ALS beam line 4.0.2.

scans. This is a necessary prerequisite for EXAFS scans.

We have taken EXAFS scans over the energy range of 380 eV–700 eV on fresh spots on the $[\text{Fe}_6\text{N}(\text{CO})_{15}]$ samples, mounted as powders on double-side carbon tape. 22 of the 36 pixels of the STJ array were used, and four scans were averaged to improve the counting statistics. Figure 62 shows the raw counts in the nitrogen and oxygen windows, normalized by the I_0 . As expected, the counts in the nitrogen window increase at the oxygen K-edge because the sample contains a factor ~ 10 more oxygen than nitrogen, and a small fraction of the oxygen K-fluorescence signal leaks into the nitrogen window. Note that some of the STJ pixels showed a substantially lower contribution of the oxygen signal in the nitrogen window than others. This is surprising, since all pixels were taken from the same wafer,

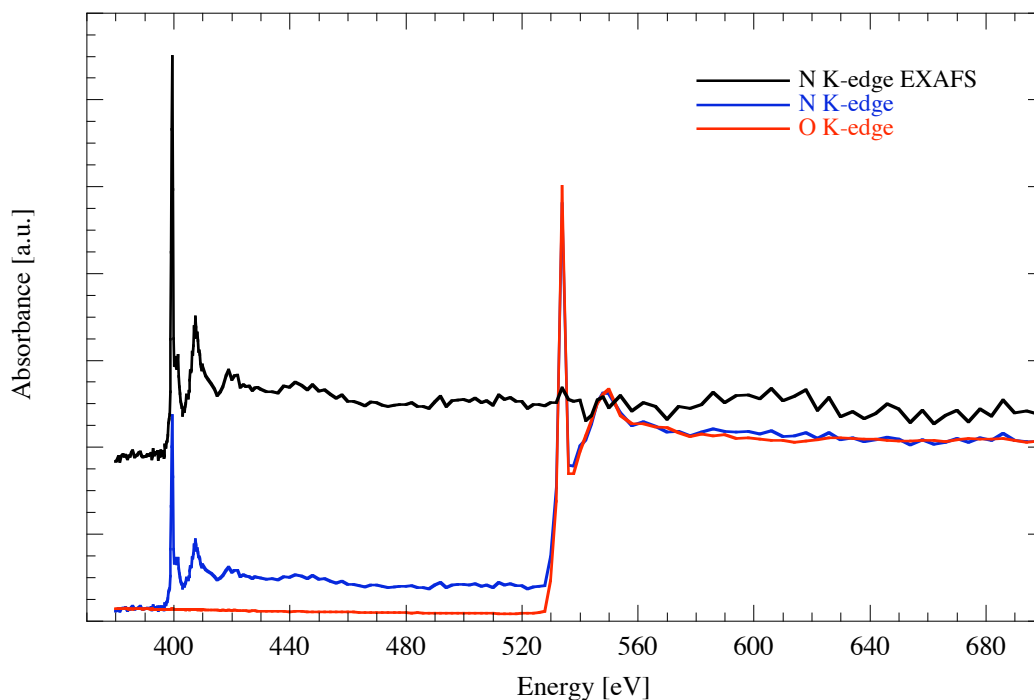


Figure 62: Raw EXAFS signal of $[\text{N}(\text{C}_2\text{H}_5)_4]_3[\text{Fe}_6\text{N}(\text{CO})_{15}]$, normalized by the I_0 grid of the beam line. Use of the carbon K-edge as an I_0 monitor would lead to an erroneous result as the carbon K-edge also exhibits significant EXAFS.

treated nominally identically, and exposed to the same atmosphere. At present, we do not understand what these differences are due to, but are encouraged that the fabrication of STJs with better response functions can be produced. Since the oxygen K-fluorescence signal can be measured independently, and since the leakage into the nitrogen window can be assumed to be proportional the oxygen K, we can subtract a constant fraction c of the oxygen K signal from the nitrogen K signal until the raw nitrogen EXAFS structure appears (Figure 62, top trace). The net nitrogen EXAFS signal can be seen to extend to 700 eV, a cutoff chose because of the iron L-edge at ~ 710 eV. Although the statistical noise in the energy range above ~ 530 eV is increased, the EXAFS oscillations are not correlated to the oxygen K signal, indicating that they are in fact due to backscattering and interference

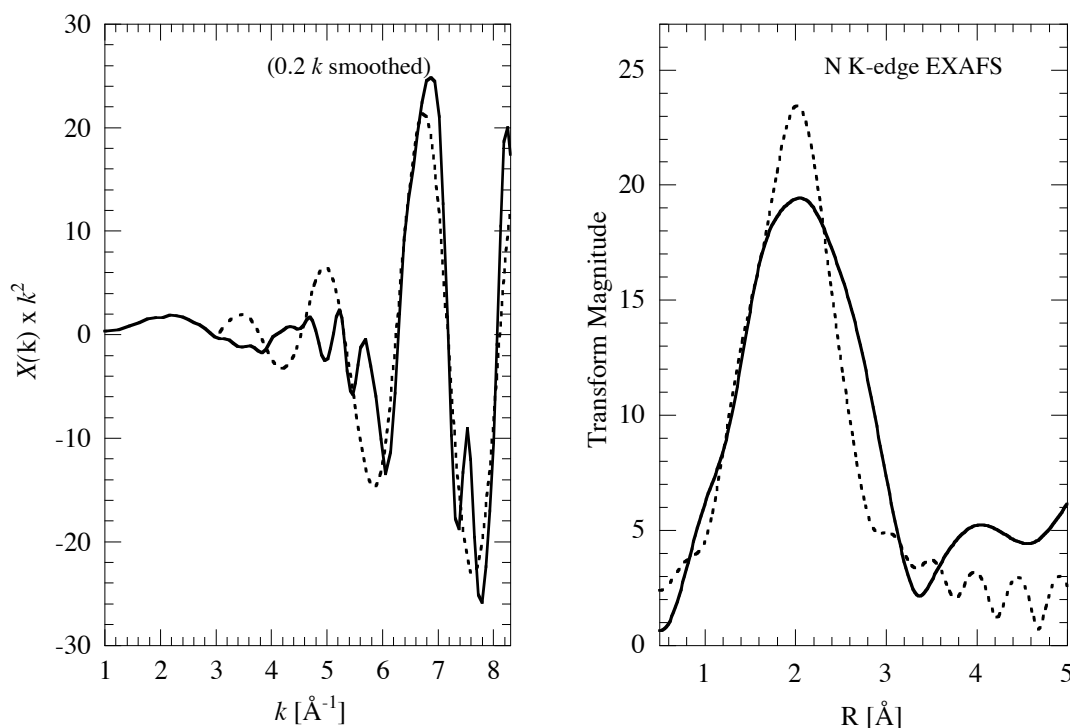


Figure 63: Smoothed EXAFS from $[\text{PPh}_4]_3[\text{Fe}_6\text{N}(\text{CO})_{15}]$. (Left) k^2 -weighted EXAFS. (Right) Fourier Transform phase-corrected for Fe.

Interaction	N	R	σ^2	ΔE
N–Fe	5.00000	2.00800	0.00239	10.33300
N–Fe	1.00000	1.56870	0.00239	10.33300

Table 3: EXAFSPAK fit Parameters for $[\text{PPh}_4]_3[\text{Fe}_6\text{N}(\text{CO})_{15}]$.

effects at the nitrogen atom.

Figure 63 shows the extracted EXAFS. The EXAFS data was analyzed using the EXAFSPAK suite of curve fitting software [George 98]. Significant difficulties were encountered extracting the EXAFS, especially fitting an appropriate spline function, which were not completely resolved. However, our best analysis is presented in Figure 63 and table 3. The data clearly fit to a nitrogen–iron interaction at $\sim 2.00 \text{ \AA} \pm 0.06 \text{ \AA}$, however, the quality of the fit was significantly improved by including a single short interaction at $1.57 \text{ \AA} \pm 0.06 \text{ \AA}$. As the crystal structure indicates an average iron–nitrogen distance of

1.85 Å, this might indicate that the interstitial nitrogen might be off-center within the cage. These experiments show that range-extended EXAFS measurements on dilute nitrogen compounds across the oxygen K-edge are feasible with STJ detectors. By extending the energy range from ~ 140 eV to ~ 300 eV, the spatial resolution can be improved from ~ 1 Å to ~ 0.4 Å. Further improvements are possible with STJ detectors with a cleaner spectral response function.

We have then applied the same approach to nitrogen in the isolated nitrogenase FeMo-co. These were prepared from FeMo-co in either NMF solutions or in methanol/acetone solution as described above. Dried films of the cofactor were prepared on sapphire substrates in the nitrogen atmosphere of a glovebox with an oxygen concentration < 0.5 ppm. One of the advantages of the methanol/acetone mixture was that the films formed very rapidly—within a few minutes—whereas the NMF-derived films required evacuating the sample in a specialized chamber within the glove box. They were transferred into the UHV chamber in an inert atmosphere inside a capped sample holder and cooled to ~ 20 K before the XAS measurements. The fluorescence-detected XANES spectra of FeMo-co (Figure 64) indicate that FeMo-co is significantly more subject to radiation chemistry than the synthetic Fe_6N -model compound analyzed above, even after cooling it to ~ 20 K with the flow-cryostat in our UHV chamber and defocusing the beam to lower the X-ray radiation intensity. The three nitrogen XANES scans over the same spot, taken immediately after one another over a total exposure time of ~ 1 hour. In addition to a reduction of the main peak, new structures appear in the spectra at ~ 395 eV and ~ 397 eV that were not present in the original sample. These may arise from photochemical reduction of the FeMo-co iron centers, and if so, would strongly suggest the presence of nitrogen

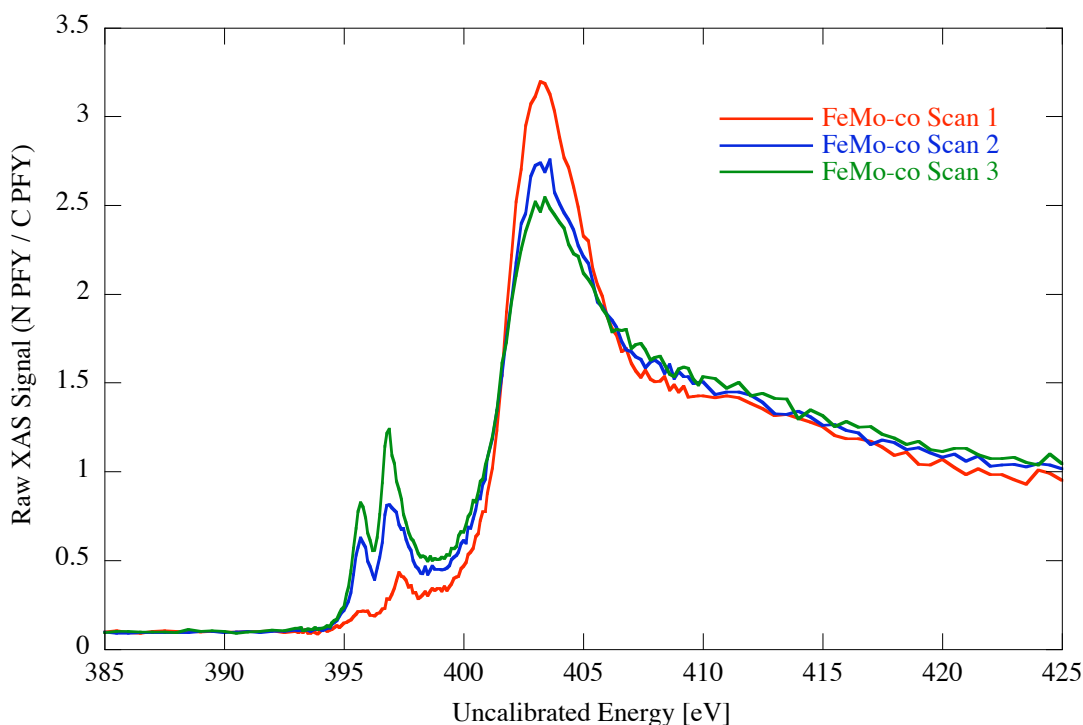


Figure 64: Nitrogen XANES of FeMo-co sample #1 (from an NMF solution). The three scans are acquired on the same spot immediately after one another to assess radiation damage.

coordinated to iron in the sample.

To quantify the time scale over which the radiation chemistry occurs, we have excited a fresh spot on the sample at 397 eV for 25 minutes in 5 second intervals, and monitored the increase of the nitrogen fluorescence (Figure 65). The peak at 397 eV starts to grow in immediately, and continues to increase linearly throughout the 25 minute scan. Although the counts in the nitrogen window in this experiment start at a value twice the level below the nitrogen K-edge, the peak at 397 eV is likely not present in the pristine spectrum at all, and the number of counts in Figure 65 at $t = 0$ reflect the low-energy onset of the K-edge. We estimate that the rapid change of the spectrum limits the time over which the sample can be exposed to radiation without change is about 5 minutes.

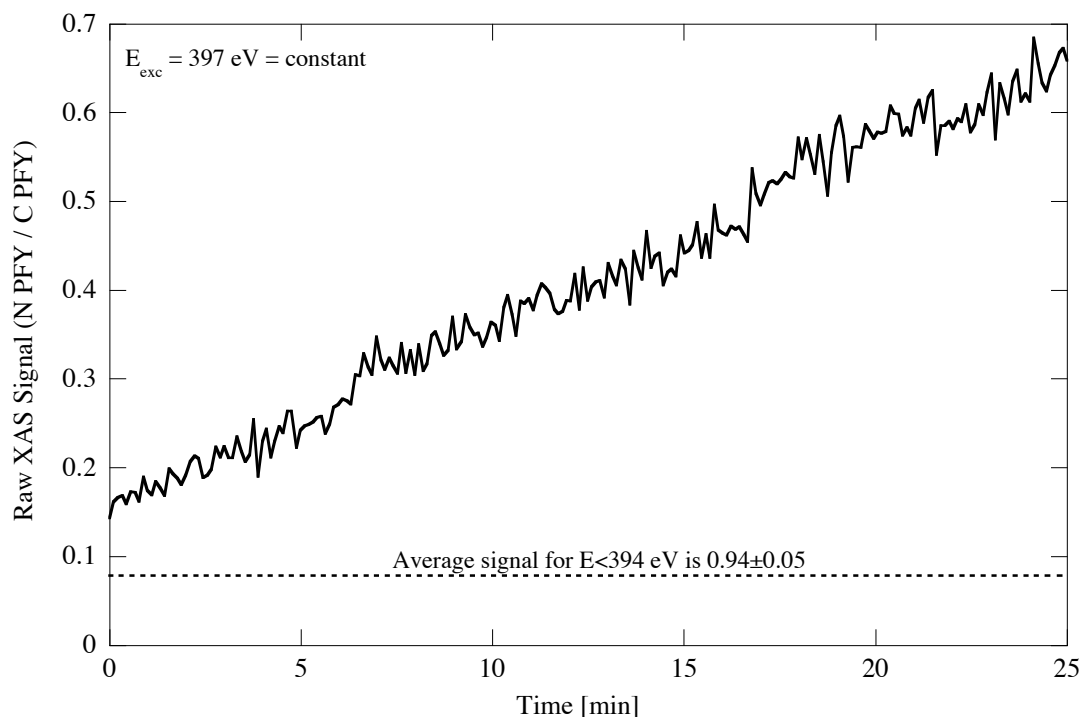


Figure 65: Radiation damage test on FeMo-co, sample #1.

The methanol/acetone FeMo-co sample was prepared as before and again cooled to ~ 20 K before exposure to the X-ray beam. The beam was defocused to reduce the X-ray density and thus minimize radiation damage. In addition, the scan was started at 395 eV, immediately before the energy region with the radiation sensitive features, with the featureless region below 395 eV captured at the end of the scan. Figure 66 shows the raw data of two successive XANES scans from the same spot of the sample, plus the first scan of Figure 64 from the NMF-derived FeMo-co sample for comparison. Interestingly, there is a third absorption feature in the scan of the pristine sample at ~ 400.5 eV that was not present at all in the other FeMo-co sample. This spectral feature has disappeared in the second scan, indicating that it arises from a rather labile nitrogen species.

We have again measured the time scale over which the radiation chemistry occurs by

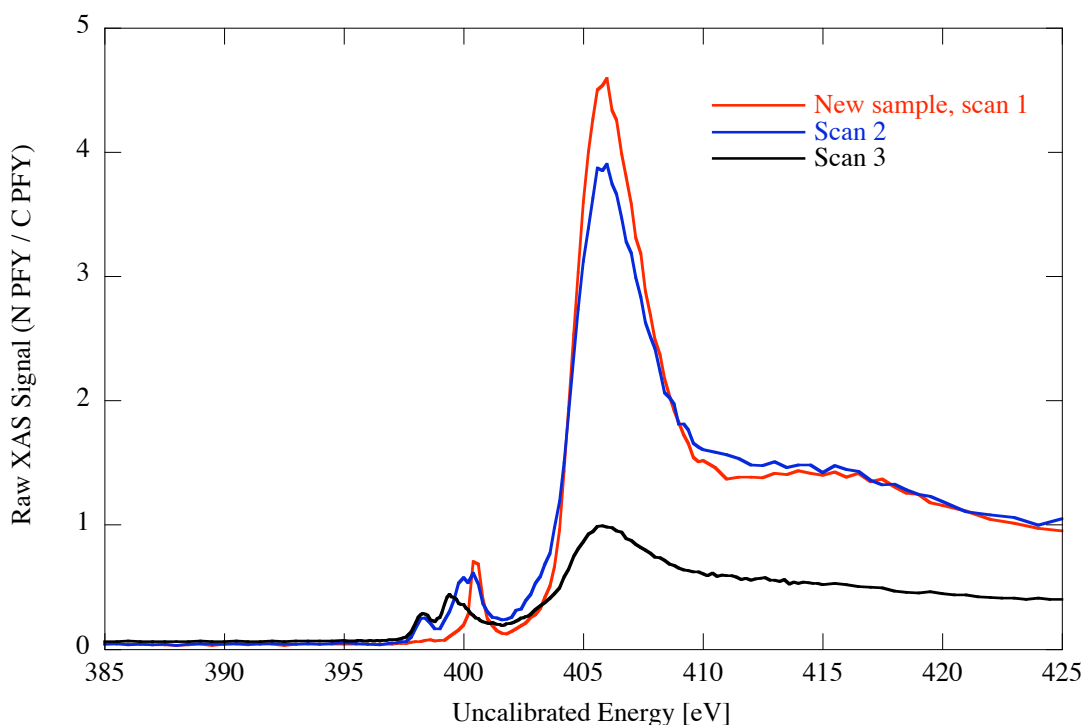


Figure 66: Nitrogen XANES of FeMo-co sample #2 (derived from a methanol/acetone solution). The two scans (top two traces) are acquired on the same spot immediately after one another to assess radiation damage. A scan from the older FeMo-co sample #1 is included for comparison (bottom trace).

exciting a fresh spot on the sample at 400.5 eV for 25 minutes in 5 second intervals, and monitored the decrease of the nitrogen fluorescence (Figure 67). The peak at 400.5 eV starts to disappear immediately, and has completely vanished after ~ 10 minutes. This suggests that each sample spot should be exposed to X-rays for at most ~ 2 minutes before the radiation-induced chemical changes compromise the sample integrity. This is sufficient for a fast XANES scan. However, for EXAFS this raises questions about the integrity of any result. It seems most likely that the observed radiation chemistry is a photoreduction of the FeMo-co. As DFT calculations suggest that one or two electron reductions of the cofactor should not open the cluster or otherwise significantly modify the cluster conformation it

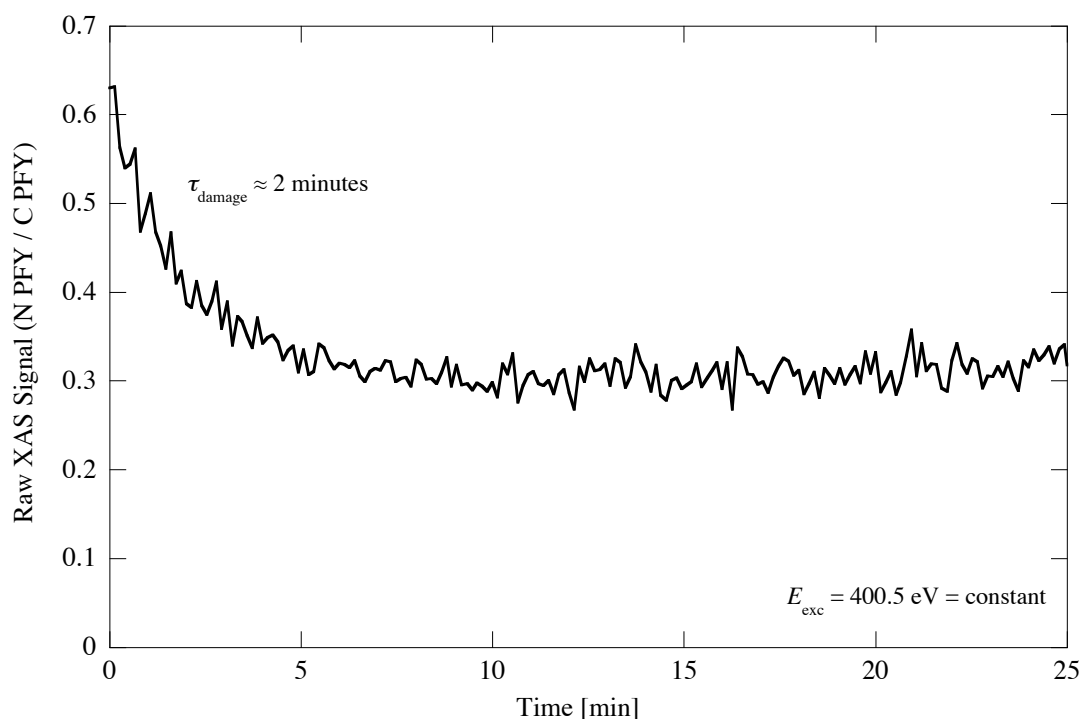


Figure 67: Radiation damage test on FeMo-co, sample #2.

seems probably that an nitrogen K-edge EXAFS spectrum should be measurable with care.

We have also examined which fraction of the nitrogen XANES signal is due to residual NMF from sample extraction that is left in the FeMo-co despite careful cleaning. Figure 68 compares the spectrum of pristine and carefully purified FeMo-co with that of an as-extracted FeMo-co and that of pure NMF. As expected, a FeMo-co sample that is not carefully purified exhibits a nitrogen XANES spectrum that is dominated by NMF, as suggested by the almost identical absorption peaks at 400.7 eV. Similar to NMF, the purified FeMo-co also shows an absorption feature in that energy range, but it peaks at a slightly lower energy of 400.5 eV, has a narrower spectral width and is not accompanied by a shoulder at $\sim 403 \text{ eV}$. This suggests that this spectrum does not contain additional NMF. However in a further experiment we used X-ray fluorescence to determine the ratio

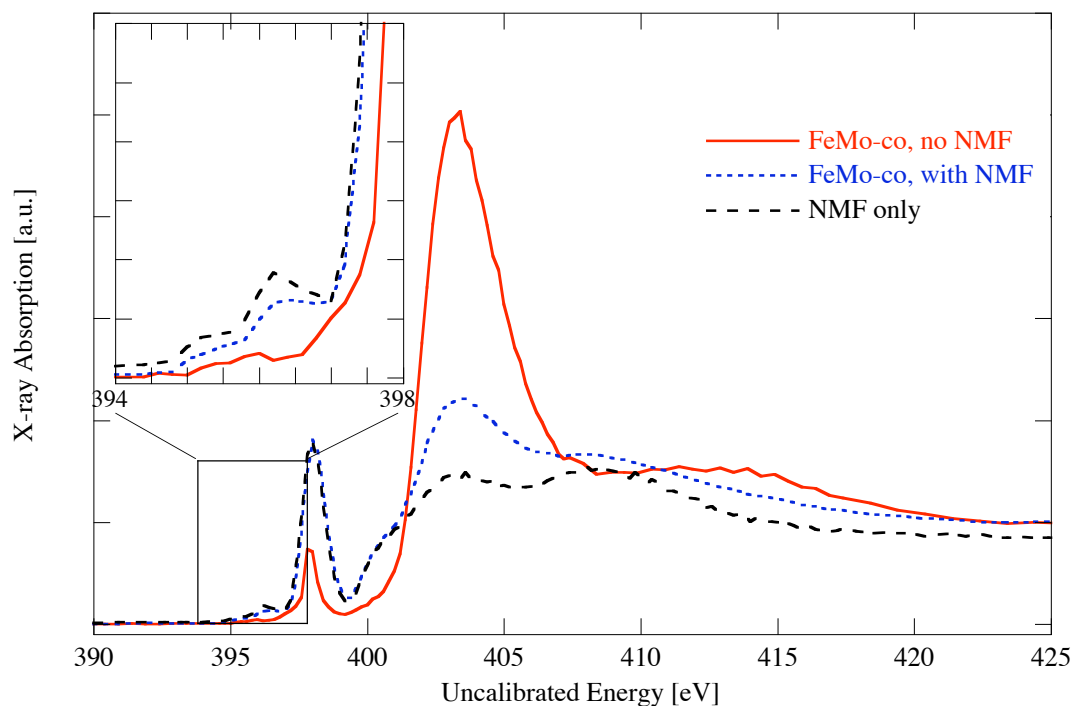


Figure 68: Nitrogen K-edge spectra of FeMo-co: (a) FeMo-co extracted into methanol/acetone (b) FeMo-co extracted into NMF (c) NMF frozen sample.

of nitrogen to iron in this sample. This measurement showed the presence of about 10 nitrogen atoms per FeMo-co. This suggests that there may be up to 10 NMF molecules associated with the FeMo-co hydration sphere.

Figure 69 shows an attempt to measure nitrogen K-edge EXAFS on the FeMo-co film prepared from methanol/acetone. Unfortunately the quality of the data is such that attempts to fit a spline over the extended range were unsuccessful due to the residual oxygen signal. Small oscillations are apparent above 430 eV which may arise from the expected EXAFS as a $\pm 15\%$ effect is expected for the pure FeMo-co, and if the sample is diluted by ~ 10 additional nitrogen then this is reduced to $\sim \pm 1.5\%$. The apparent EXAFS in Figure 69 is perhaps half this size. Hence we can draw one or both of two conclusions:

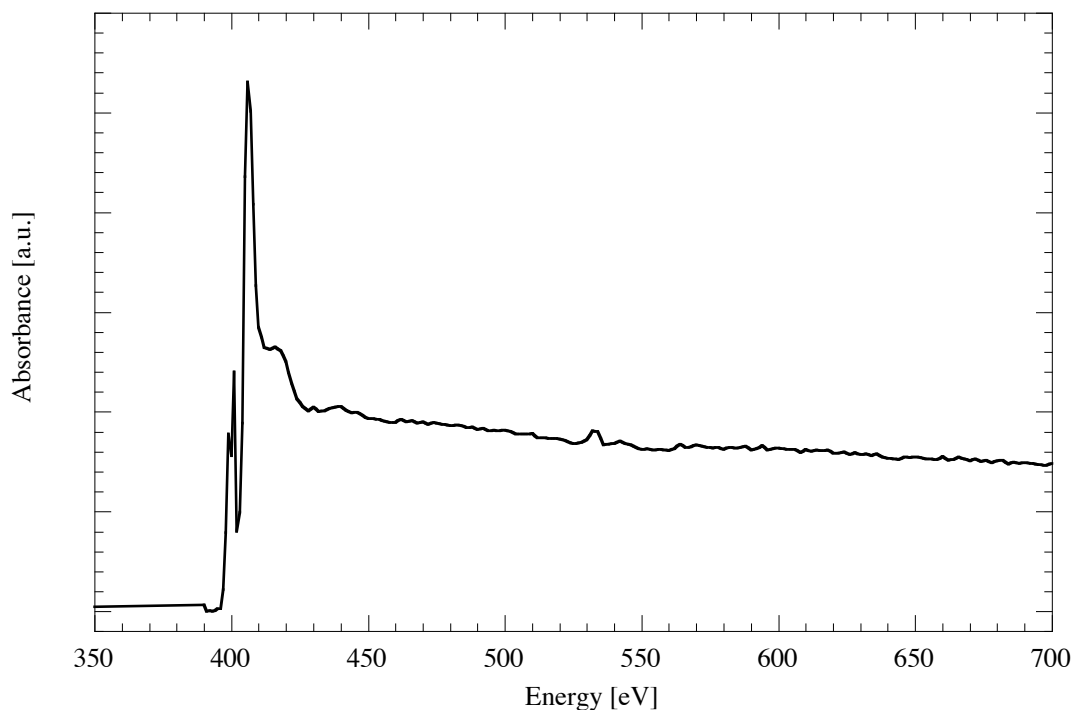


Figure 69: Nitrogen K-edge EXAFS absorption spectrum of FeMo-co.

(1) the central atom is not a nitrogen atom or (2) the presence of adventitious nitrogen in the samples means that range-extended EXAFS on FeMo-co is not yet possible with our current setup. The successful completion of this experiment will likely require STJs with higher sensitivity to capture the signal faster and a cleaner response function to suppress the oxygen signal leakage into the nitrogen window, as well as FeMo-co containing less additional nitrogen atoms.

3.4 Iron Spectroscopy

Different species of $[n\text{Fe-}m\text{S}]$ clusters can attain different oxidation states and thus provide a variety of redox potentials and serve as electron carriers. For example, the $[4\text{Fe-}4\text{S}]$ clusters in ferredoxins vary their redox state between 1 and 2 with a reduction potential

Name	Cluster	Organism	Cluster Ox. St.	Iron Ox. St.
Rubredoxin (Rd)	[1Fe-0S]	<i>Pyrococcus Furiosus</i>	+II or +III	<u>2.0</u> or 3.0
Ferredoxin (Fd)	[2Fe-2S]	<i>Aquifex aeolicus</i>	+I or +II	<u>2.5</u> or 3.0
Ferredoxin (Fd)	[4Fe-4S]	<i>Pyrococcus Furiosus</i>	+I or +II	<u>2.25</u> or 2.5
High-Potential Iron Protein (HiPIP)	[4Fe-4S]	<i>Thermochromatium tepidum</i>	+II or +III	<u>2.5</u> or <u>2.75</u>
Iron Protein (Fe)	[4Fe-4S]	<i>Azotobacter vinelandii</i>	0 or +II or +III	2, <u>2.25</u> or 2.5
Ferric model	[4Fe-4S]	Synthetic	+IV	<u>3.0</u>

Table 4: Iron–sulfur cluster properties.

around -400 mV. The [4Fe-4S] clusters in high potential iron protein can be found in the 2 and 3 states with a positive redox potential up to 450 mV. Finally, the [4Fe-4S] cluster in nitrogenase that is part of the iron protein, can reach the fully reduced state with four ferrous ions. In the other extreme, the all-ferric cluster has been synthesized in the laboratory, but has not yet been observed in nature.

Earlier work in our group has analyzed whether X-ray absorption spectroscopy on the iron L-edges can be used to study valence state of iron ions in different iron–sulfur clusters [Piamonteze 07]. The systems studied were the [1Fe-0S] cluster in rubredoxin (Rb), the [2Fe-2S] ferredoxin from *Aquifex aeolicus* (Aa), the [4Fe-4S] clusters from *Pyrococcus Furiosus* (Pf) ferredoxin, mutations D14C and A33Y, HiPIP from *Thermochromatium tepidum* (Tt), iron protein from *Azotobacter vinelandii* (Av) and a synthetic all-ferric model compound. These [n Fe- m S] clusters can be poised in different cluster oxidation states, and consequently the average iron oxidation state can vary between the extremes of +2.0 and +3.0. Table 4 summarizes the properties of these iron–sulfur clusters, with the average iron oxidation states that were actually analyzed by XAS underlined.

The earlier fluorescence-detected XAS spectra of iron L-edges in these iron–sulfur

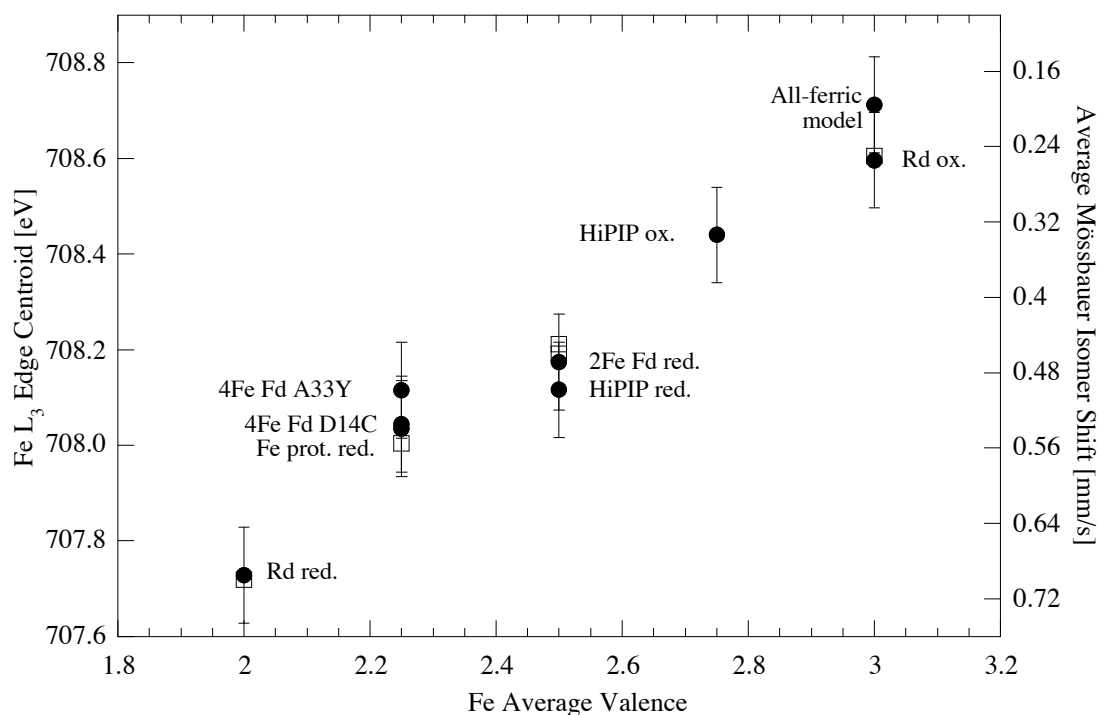


Figure 70: Iron L₃-edge energy shift. Mössbauer data is represented by open squares, and XAS data is represented by filled circles.

clusters were taken with a multi-element Ge detector. As expected, they show a systematic edge shift as a function of average iron oxidation state, with the higher the oxidation state shifting the L₃ centroid to higher energies. This is because higher oxidation states correspond to a reduced electron density and thus reduced electron screening and tighter binding of the core iron levels. Figure 70 summarizes the results of the earlier study, which are currently being prepared for publication [Piamonteze 07]. The systematic change of the iron L-edge with oxidation state provides the basis for determining iron oxidation states in iron–sulfur clusters of unknown charge state.

In this work, we used the STJ spectrometer for iron L-edge spectroscopy on the isolated active-site cofactor of nitrogenase, FeMo-co. The STJ detector had a number of advantages

over the Ge detector, including better background rejection which enabled the measurement of solution samples. The FeMo-co samples were provided by two groups: Prof Barry Smith, John Innes Center, England, and Prof Bill Newton, Virginia Tech, Virginia. The Newton group provided samples extracted from the enzyme into NMF whereas the Smith group provided cofactor further exchanged into a methanol/acetone mixture. They were dried on an sapphire disk in an oxygen-free atmosphere of a glove box, mounted in a capped sample holder during transfer into the UHV chamber, and only uncapped after the sample had been cooled to a temperature around 20 K to suppress chemical changes brought on by exposure to radiation. Figure 71 shows two consecutively acquired iron L-edge spectra, with S/N ratio between ~ 230 and ~ 320 . Even with this very high S/N ratio no statistically different change between the two scans can be observed, indicating that the iron chemistry is not altered due to exposure to X-rays under these conditions. Note that several other FeMo-co samples that were examined in the course of these experiments showed additional absorption features, often dramatically different from those of well-known stable iron-sulfur clusters from the earlier study. These features were considered to be due to adventitious iron contamination, and the spectra were excluded from further investigation. To determine the average iron oxidation state, we use the same algorithm that was developed for the study shown in Figure 70. With this procedure, the L_3 -centroid is found to be at 707.96 eV, corresponding to an averaged iron oxidation state of 2.25 ± 0.1 (Figure 72). As FeMo-co has a spin $S = 3/2$ ground state, it follows that its average valence must either be 2.43 (3Fe(III):4Fe(II)) or 2.14 (1Fe(III):6Fe(II)). The current data is more consistent with the second (1Fe(III):6Fe(II)) option. While the error is not small, it should be noted that damage to FeMo-co will most likely be oxidative which is consistent with

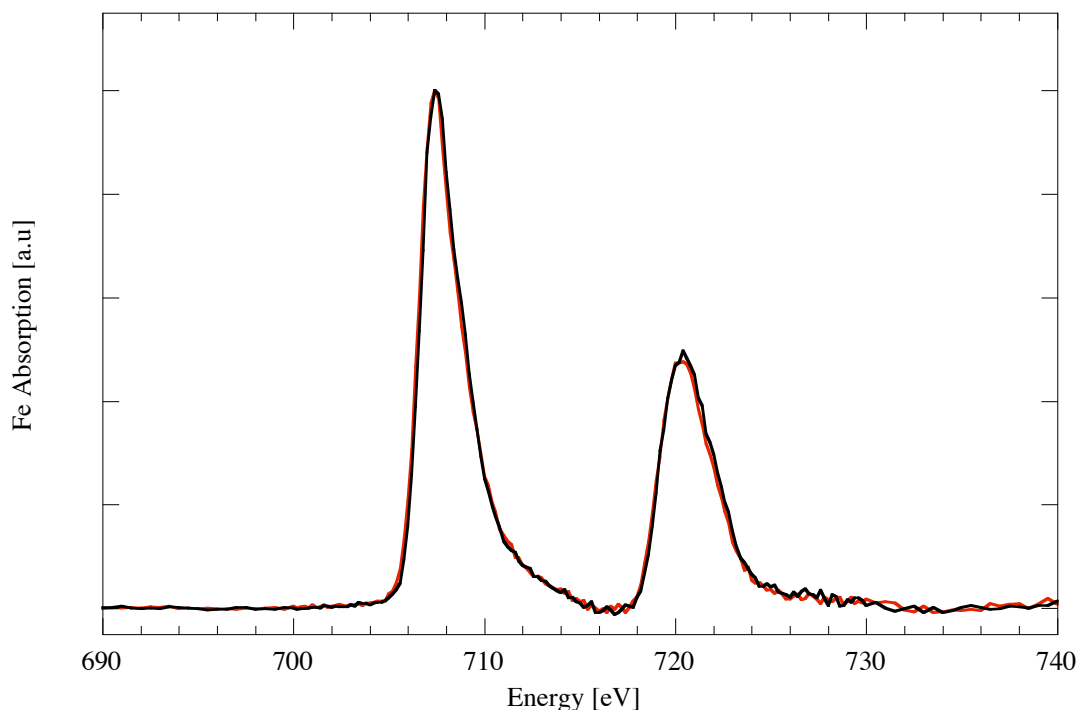


Figure 71: No radiation chemistry effects are observed on the iron $L_{2,3}$ -edges when the FeMo-co sample is cooled. The edge step has been removed and the spectra scaled in order to show that the relative heights, shapes, and positions of the $L_{2,3}$ -edges remains unchanged from one scan to the next.

a slightly increased Fe(III) content in our current measurement. Another possible error arises from the fact that the correlation in Figure 70 was established using iron–sulfur clusters containing only iron with all sulfur ligation. FeMo-co includes a molybdenum site and an interstitial light atom (C, N, O). It is unlikely that including a molybdenum site will significantly alter the calibration of Figure 70. With regard to the interstitial atom, it is relevant that iron–oxygen and iron–nitrogen ligated complexes have centroids 1 eV to 2 eV higher than iron–sulfur clusters, and hence a central light atom may be expected to shift the edge slightly to higher energy which is not inconsistent with the results here. Therefore we conclude that these data indicate a largely Fe(II) cluster with only a single Fe(III) atom.

The high quality of the data in Figure 71, with their low adventitious iron deserves some

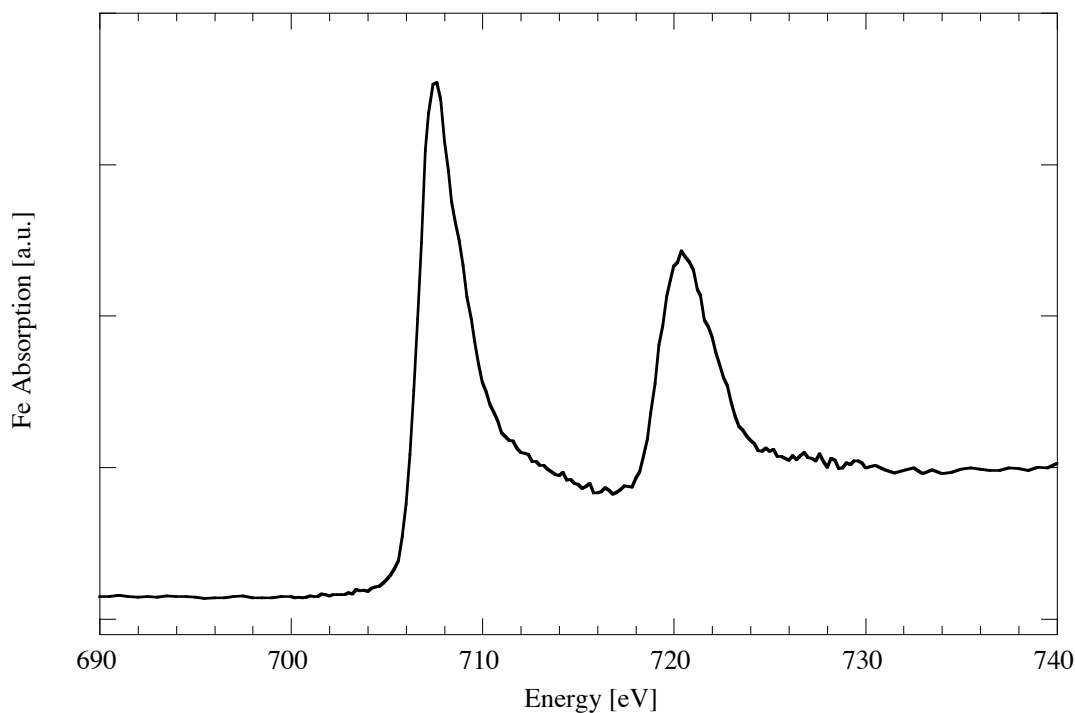


Figure 72: Iron absorption spectrum normalized by counts in the oxygen window. The L_3 -centroid is found to be at 707.96 eV, corresponding to an averaged iron oxidation state of 2.25 ± 0.1

comment. These measurements were taken on FeMo-co films prepared from the cofactor in methanol/acetone provided by the Smith group. As methanol/acetone has a much lower boiling point than NMF the films formed very rapidly—usually in less than 5 minutes, compared to over an hour for the FeMo-co/NMF derived films. It is quite possible that some of the adventitious iron in the NMF samples was formed during the slow drying process with this solvent. However, solution iron L-edge experiments (see below) on the FeMo-co/NMF samples provided by the Newton group also showed significant quantities of adventitious iron.

While the high energy resolution of the STJ spectrometer did not provide new insights into the iron chemistry of FeMo-co that could not have been gained with a conventional

Ge detector, the XAS spectra from the STJ did have a higher S/N ratio and thus a lower statistical error of the iron L₃-centroid. This turned out to be less important in this study of the iron–sulfur cluster in FeMo-co, but it would be crucial if the iron concentration were significantly lower. This will be the case in future experiments to analyze proteins in solution in order to examine their chemistry in a state that resembles their natural environment more closely.

A central concern in the X-ray spectroscopy of biological samples is to maintain sample integrity throughout the experiment. This not only relates to radiation damage of the sample during a scan, but also to the chemical changes caused by drying the samples into films on the sample holder. On the one hand, soft X-ray spectroscopy on a dried protein films is significantly easier than on a liquid samples, since liquids sublime under UHV conditions and dried films have a higher protein concentration. On the other hand, drying can change the chemistry of the sample, especially of proteins, and raises concerns whether the spectral information is representative of the protein under biologically active conditions.

We have initially attempted to address this problem by freezing a liquid protein sample on a sample holder before loading it into the dry N₂ atmosphere in the load lock, and keeping it frozen during the transfer into the UHV chamber and the XAS scan. Surprisingly, these experiments always had a very poor S/N ratio and have never yielded any useful spectra, not even on comparably concentrated samples that should have easily been measurable. We suspect that this is due to a separation of the solvent and the protein during cooldown, with the heavier protein condensing first onto the holder, and the sample surface ending up with a disproportionate amount of the solvent.

We have therefore built a sample holder that is compatible with the existing mounting

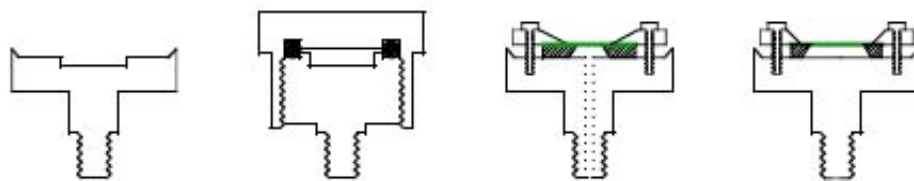


Figure 73: UHV liquid sample holder designs. Starting on the left, is a sample holder designed to hold a frozen ($< 20\text{K}$) sample in a well. The frozen sample will sublime upon exposure to vacuum. Next is a capped holder designed for samples that require an anaerobic environment. The remaining two holders utilize a silicon nitride membrane on a silicon substrate to provide the thin window that prevents evaporation of a liquid sample. One is filled and sealed through a hole in the back, and the other is filled from the top with the window attached after sample placement.

scheme and can hold a liquid sample behind a thin silicon nitride (Si_3N_4) membrane inside a UHV sample chamber (Figure 73). Silicon nitride has a very high tensile strength, so that 100 nm-thin films grown epitaxially on silicon wafers will form stable free-standing windows once the silicon has been selectively etched away. In addition, Si_3N_4 is light, so that these 100 nm-thin films have an appreciable X-ray transmission for soft X-rays. Still, experiments on liquids are less sensitive, because the sample is intrinsically more dilute, the Si_3N_4 window transmission is finite (about 50% at iron L, but significantly less at lower energy), and the distance between sample and STJ detector increases by about a factor of two as the sample can no longer be placed on the edge of the sample holder immediately in front of the outermost IR-blocking window.

We have tested the feasibility of soft XAS on liquid samples by comparing iron L spectra of $\text{K}_3\text{Fe}(\text{CN})_6$ powder with those of a 40 mM solution behind a Si_3N_4 window (Figure 74). While the (S/N ratio of ~ 90 for the solution sample is lower than that of the solid sample with $S/N \approx 420$, it is still very much sufficient to extract detailed chemical information. In addition to an edge shift, the spectrum of the solution exhibits a sharpening

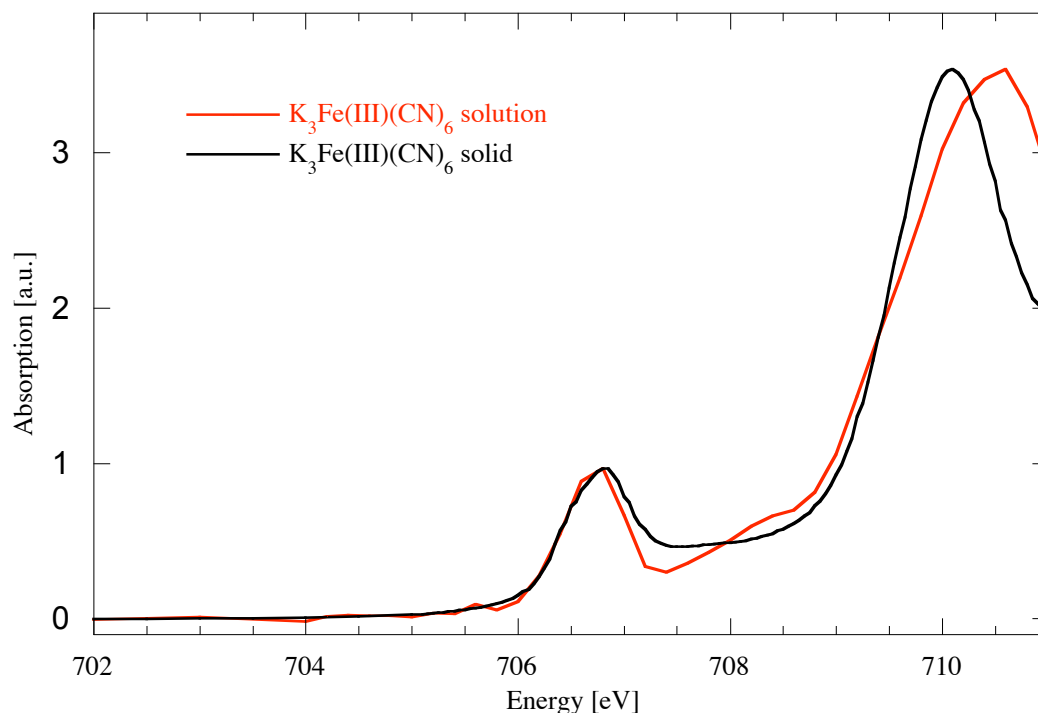


Figure 74: Comparison of solid and solution $\text{K}_3\text{Fe}(\text{CN})_6$ sample absorption spectra.

of the spectral features. This is expected in solutions where the influence of the ligands on the band broadening is reduced. This effect is more easily observed at the L-edges whose natural linewidth is narrower than that of the higher-energy K-edges, and proved an additional incentive to develop soft X-ray instrumentation.

We have also taken iron L-edge spectra on FeMo-co solutions with the same setup (Figure 75). The spectra again have a very high S/N ratio, certainly more than sufficient to extract chemical information with high confidence. However, the spectra showed additional spectral features at 710 eV, 711.5 eV and 723 eV that were fundamentally different from all other iron L-edge spectra on iron–sulfur clusters we had taken on well-characterized samples. They were therefore attributed to some unknown iron species that was not part of the iron–sulfur cluster in FeMo-co, and the spectra could therefore not be used to extract

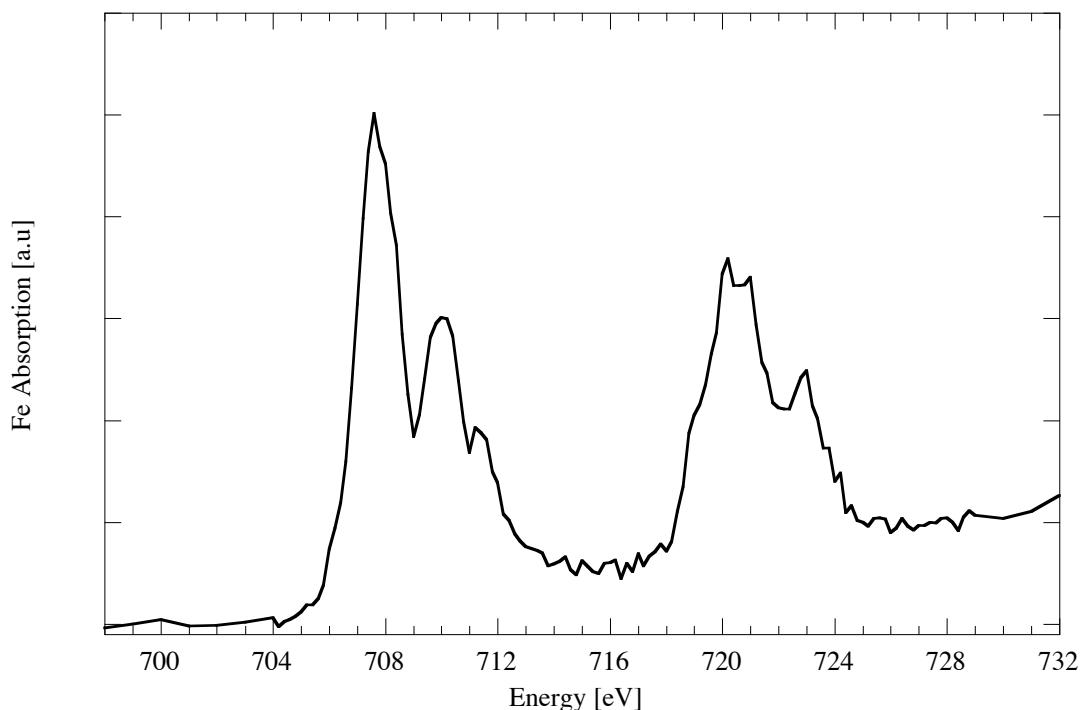


Figure 75: Iron absorption spectrum of FeMo-co solution.

biologically relevant information. Unfortunately, by the time our experimental setup had been developed to the point that spectroscopy on solutions was possible, the high-purity FeMo-co samples used in the spectra in Figure 72 were no longer available, because the scientist who had provided them, Prof Barry Smith, retired.

These experiments show that XAS on solutions is clearly possible with STJs. The sensitivity and thus the feasibility to analyze protein solutions depends on how concentrated the solution can be made, and how the protein and the solute are distributed behind the Si_3N_4 window upon freezing, since proteins at room temperature will likely change chemically upon prolonged exposure to X-rays during an scan. A realistic minimum concentration for a good spectrum with the 36-channel device is 50 ppm iron. This corresponds to ~ 1 mM iron—an achievable concentration for a biological sample.

4 Summary and Outlook

4.1 Summary

We have built a superconducting tunnel junction (STJ) X-ray spectrometer for high-resolution soft X-ray spectroscopy at the synchrotron. STJs are well-suited for the chemical analysis of dilute samples by fluorescence-detected X-ray absorption spectroscopy (XAS), because they combine the high efficiency of solid state detectors with the high energy resolution of low temperature technology and the high count rate capabilities of athermal devices.

The first part of this dissertation describes the design and performance of the instrument. The STJ sensor consists of a pixilated Nb–Al–Al₂O₃–Al–Nb tunnel junction array, and its operation is based on measuring the temporary increase in tunneling current after X-ray absorption in the niobium absorber film. For STJ operation at the synchrotron, we have built a two-stage adiabatic demagnetization refrigerator (ADR) that holds the STJ arrays at the end of a 40 cm-long cold finger that can be inserted into a UHV sample chamber at a beam line end station. The ADR uses liquid nitrogen and liquid helium for pre-cooling to 77 K and 4.2 K, respectively, and two different paramagnets to cool the STJs to their operating temperature of ~ 0.1 K. The two-stage design allows attaining the base temperature without pumping on the He bath in a cooling cycle that has recently been automated, a significant improvement in user-friendliness and turn-around between cooling cycles.

The STJ spectrometer, developed with other members of the Advanced Detector Group at LLNL, has achieved an energy resolution below 10 eV in the soft X-ray band below

1 keV, and can be operated at count rates up to $\sim 30\,000$ counts/s per pixel [Friedrich 06a]. In the course of the last six years, we have repeatedly upgraded the instrument to improve its sensitivity for synchrotron science by increasing the array size to initially 9, later 36 pixels, and by re-designing the detector cold finger to bring the STJ array closer to the sample and increase its solid angle coverage to 10^{-3} . Attempts to increase the spectrometer quantum efficiency by developing new IR-blocking windows have so far not been successful.

We have demonstrated that the current STJ spectrometer is already more sensitive for fluorescence-detected XAS in the soft X-ray band than conventional Si(Li) or Ge detectors (because of its high energy resolution) and than grating spectrometers (because of its high solid angle coverage) [Drury 06]. This capability has led to new scientific insights, not only in the field of bioinorganic chemistry [Funk 04], but also in environmental science [Friedrich 06a] and material science [Melcher 05, Fons 06].

In the second part of this dissertation, we have investigated the contribution that this STJ spectrometer can make to understand the chemistry of the iron-molybdenum cofactor (FeMo-co) in the active site of the metalloprotein nitrogenase that is responsible for bacterial nitrogen fixation. FeMo-co contains the elements iron, sulfur, molybdenum and (potentially) nitrogen, and we have used the STJ spectrometer to examine the lower energy edges of these elements that are not (or not as well) accessible by XAS with conventional Ge or grating spectrometers. We have confirmed that the molybdenum $M_{4,5}$ -edges of model compounds are significantly sharper than the K or L-edges and thus more sensitive to chemical changes [Drury 06]. The molybdenum $M_{2,3}$ -edges of the same compounds increase systematically with higher oxidation state as expected. We have also use the STJ to take the first fluorescence-detected sulfur L-edge spectra on inorganic model

compounds. The $L_{2,3}$ -edges are very narrow and exhibit the predicted strong chemical shifts. The analysis of molybdenum and sulfur in FeMo-co is currently still not possible because of a combination of a very low fluorescence yield, a high spectral background from artifacts in the STJ response function, and an unexpectedly low sample concentration even in nominally pure FeMo-co. For absorption spectroscopy below the oxygen K-edge at ~ 540 eV, the XAS background is limited by a surface layer artifact that causes a low-energy shoulder below the second-order excited oxygen K and carbon K lines. For XAS above ~ 540 eV, the spectral background is set by pile-up of the strong oxygen K and carbon K-lines.

We have acquired iron L-edge spectra on FeMo-co with very high signal-to-noise ratio that can be used to determine the average iron oxidation state. We have also built a solution cell for operation in the UHV chamber that allowed us to take iron L-edge spectra on 20 mM FeCl_3 solutions, which exhibit the expected sharpening of the spectral features in solution compared to solid FeCl_3 . This is an important step towards the future analysis of frozen metalloprotein solutions.

In addition, we have captured the first range-extended nitrogen EXAFS across the oxygen K-edge. After subtracting a signal proportional to the oxygen K fluorescence, the EXAFS range could be extended to 700 eV. This improves the spatial resolution of the EXAFS on dilute nitrogen by a factor of 2. Unfortunately, the same EXAFS measurements on FeMo-co are inconclusive as to whether there exists a central nitrogen atom inside its central iron-sulfur cluster because of adventitious nitrogen in the sample, most likely due to residual NMF used to extract the FeMo-co from the FeMo-protein.

4.2 Outlook

Future developments will continue to focus on improving the sensitivity of the STJ spectrometer by further increasing the solid angle coverage and improving the spectral purity of the response function. An energy resolution of 10 eV to 20 eV FWHM is already sufficient for fluorescence-detected XAS in the soft X-ray band, since emission lines are typically spaced at least 50 eV apart. In fact, we have in the past repeatedly traded off some energy resolution for better solid angle coverage when we placed the STJ array closer to the outermost IR-blocking window where IR-induced shot noise increases. STJ count rate capabilities above 10 000 counts/s are also sufficient, since fluorescence yields are low in the soft X-ray band and observed count rates in the $200\text{ }\mu\text{m} \times 200\text{ }\mu\text{m}$ STJ pixels never exceed the maximum rate [Drury 06].

The solid angle coverage can be increased by increasing the number of pixels in the STJ array, subject to the constraint that the cryostat can handle the increased heat load from the increased number of wires. The next generation STJ spectrometers will be based on a 112-pixel array [Friedrich 06b]. The first prototype arrays have been fabricated and are currently being evaluated. We have already purchased a 112-channel digital signal processing (DSP) readout [Friedrich 06a], and have started the development of a cheap and scalable preamplifier to replace the current single-channel preamps. Increasing the solid angle coverage by placing the STJ array closer to the sample is no longer possible with the current detector geometry, since the distance between the three IR windows has already been reduced to 1 mm–2 mm, and a further reduction would make the spectrometer prone to failure due to touches that develop as a consequence of differential thermal contraction

during cooldown.

The purity of the spectral response can be improved by reducing the surface contamination on top of the niobium absorber film, and by reducing the area over which the electrical contacts to the top STJ electrode cover the electrode. These changes have been implemented into the mask design of the next generation of STJ chips currently under development. In addition, replacing the Nb-based STJs with Ta-based STJs will increase the quantum efficiency of the top absorber film and thus suppress the line-splitting artifact [Friedrich 06b]. The algorithms used in the DSP readout already provide a better pile-up rejection than the analog shaping amplifiers currently used for pulse processing [Friedrich 06a]. Better algorithms may be able to improve the peak-to-background ratio due to pile-up even further.

These changes will increase the sensitivity of the spectrometer by more than an order of magnitude and enable some of the experiments in bioinorganic chemistry that are currently beyond reach. In the context of nitrogen fixation, they include spectroscopy at the molybdenum M-edges and the sulfur L-edges in the FeMo-cofactor of nitrogenase. For other metalloproteins such as hydrogenase or CO-dehydrogenase, spectroscopy will be possible on frozen solutions that are currently too dilute. In the context of radiation-sensitive proteins such as the oxygen-evolving complex in photosystem II, L-edge spectroscopy of the central 4Mn-cluster may be possible over time scales below the damage threshold.

Finally, if STJ spectrometers are ever to be operated by non-specialists, their operation must be further automated so that they can be fully remote-controlled by computer. The first step in this direction is the development of a liquid-cryogen-free ADR that can attain a

base temperature of ~ 0.1 K at the push of a button. Such an ADR, which uses a mechanical pulse-tube refrigerator for precooling to 4 K to replace the cryogenic liquids, is currently being built in collaboration with VeriCold Technologies Inc [VeriCold07]. The next step is the development of a remote-controllable preamplifier so that the detector biasing, which currently still requires a degree of experience and sensitivity, can also be standardized. This automation is part of the ongoing preamplifier development discussed above. Finally, sample motion and spectrometer motion should be automated. This is not fundamentally difficult, and should greatly improve our ability to deal with radiation damage and improve the user-friendliness of STJ spectrometer operation.

During the course of this dissertation, we have advanced the performance of STJ spectrometers to a point that they have turned from a laboratory curiosity to a powerful scientific instrument in synchrotron science. We also have developed a much clearer understanding of which XAS experiments are possible now, and which ones require further instrument refinement. While some of the most promising experiments on metalloproteins are still out of reach, other samples can be (and have been) analyzed with high precision, and the results are being recognized by the synchrotron community. As always, the more we learn, the more we see what we don't yet know.

Appendices

A Analysis Software

Absorption spectra acquired at beam line 4.0.2 are recorded in two formats. Equipment that is part of the beam line saves data in ASCII format, while equipment that is part of the ABEX end station and uses the proprietary Canberra software saves data in a binary format. Our existing Matlab software for analyzing the TEY, Ge and STJ detector data contains two major drawbacks: it crashes often with the attendant loss of progress, and it assumes that the calibration of the fluorescence spectra changes very little over the course of several scans. In addition, it is not very user-friendly when it comes to interpreting complicated spectra that may be affected by scatter or higher harmonics of the monochromator, by structure in the background signal, or by pile-up peaks. It is also limited in the options for background subtraction, especially for TEY spectra whose background variations often exceed the magnitude of the absorption signal of interest. In order to analyze either type of data with a unified set of tools, we have written a software package to import and manage XAS data sets.

Electron yield only data are typically acquired with the beam line equipment, while fluorescence detected XAS and possibly concurrent electron yield data are acquired using the ABEX equipment. The ASCII files consist of delimited text with time, date, energy, and data fields. The binary format consists of a header with information such as time, number of pixels read out, number of multichannel analyzer (MCA) bins, and information regarding the digitizer setup. After the header, blocks of fluorescence spectra for each pixel

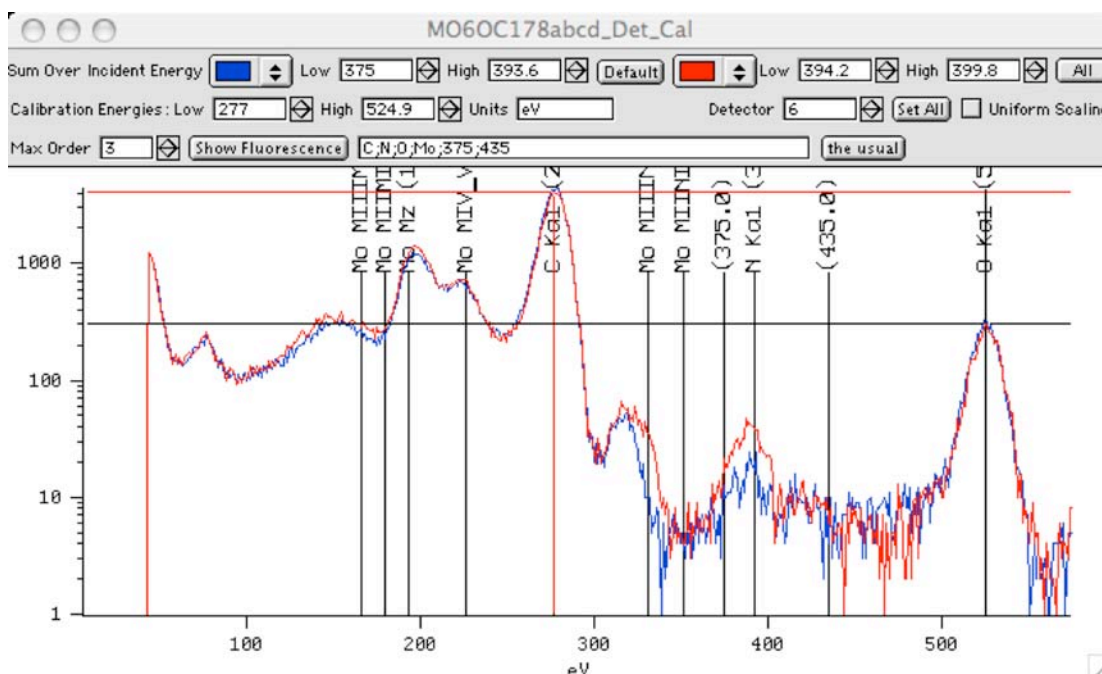


Figure 76: Detector pixel calibration window.

are recorded sequentially; pixel 1–22, for each energy step. This file also contains the I_0 data and the electron yield readout from the sample current and the channeltron.

Importing the ASCII file and displaying the absorption spectrum is straightforward. The fluorescence-detected XAS data then require counting the number of events in a window of energies for each pixel. The previous software relied on the fact that the calibration of the Ge or STJ detector pixels and thus the specification of the windows will not change, so that optimized windows are readily useable for different scans and beam times. This is, in general, not the case. We have therefore chosen to require the calibration of each pixel of the STJ based on strong fluorescence lines to allow the re-use of window specifications. This procedure also helps to differentiate artifacts from small signals.

Figure 76 shows the window used to calibrate each pixel. It shows the (two) X-ray fluorescence (XRF) spectrum of the pixel in logcounts vs. MCA channel. The range of

incident energies for which XRF spectra are added is selectable. By selecting, for example, the first half of the scan for one and the second half for the other XRF spectrum, the user can identify scatter by observing the associated peak shifts.

Two cursors are visible, and the user places them on two known peaks. The energy of each peak is entered, typically in units of eV, and the program performs a linear calibration of the spectrum. A linear calibration is usually sufficient if the intense oxygen K and carbon K peaks are used to calibrate the spectrum, although higher-order calibrations can be performed if necessary. To aid in peak identification and verification of the calibration, elements (separated by semicolons) can be entered in a window above the plot and their fluorescence peak positions displayed. In addition, energies of expected peak positions can be entered and they, as well as the selected harmonics, will be displayed.

Once each pixel has been calibrated, a similar window (Figure 77) is used to set the windows. Here the cursors are used to delineate the window. Via a pull-down menu, the user can choose to set a new window or select an earlier window. In Figure 77, the check box to show the shaded region of all set windows has been selected. Pressing the “Absorption” button will open a plot containing the absorption spectrum of the current pixel and window (Figure 78). Changing the window setting will immediately update the associated XAS spectrum, and thus provide immediate feedback between the choice of windows and the associated XAS spectrum of that pixel. This is particularly useful when a weak line (such as molybdenum M) lies on top of a varying background (such as the surface artifact associated with the carbon K or nitrogen K fluorescence), because it is often not intuitive which choice of windows will produce the XAS spectrum with the highest signal-to-noise ratio. After the windows for one channel have been set, the user can either apply

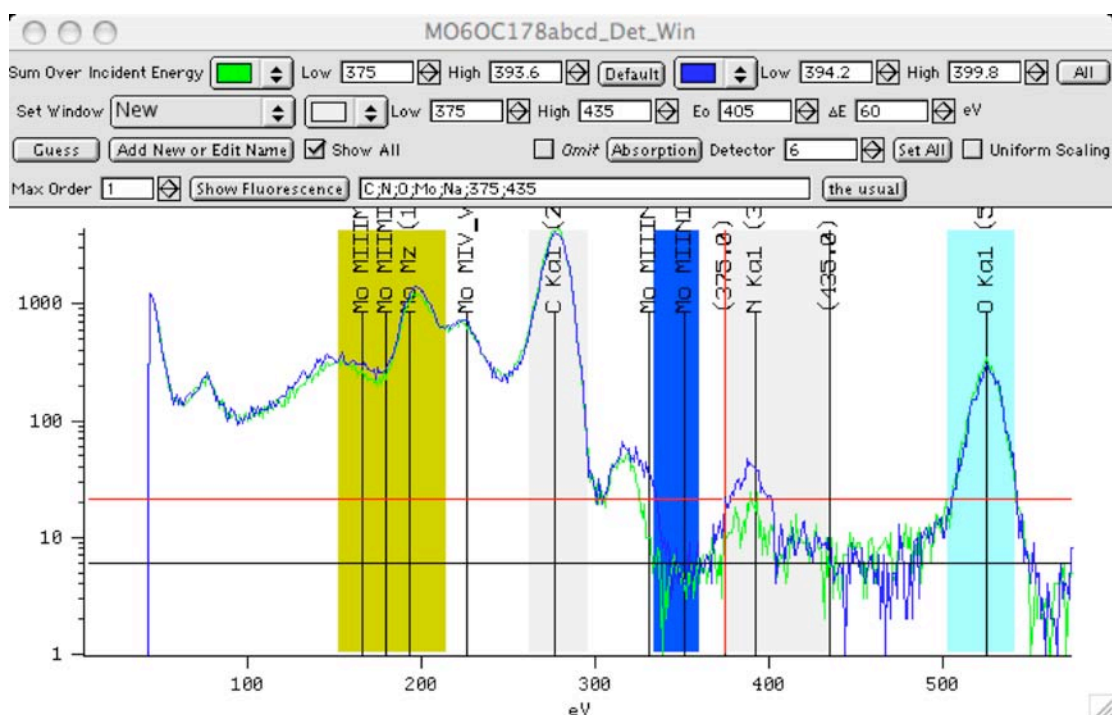


Figure 77: Detector pixel window tool.

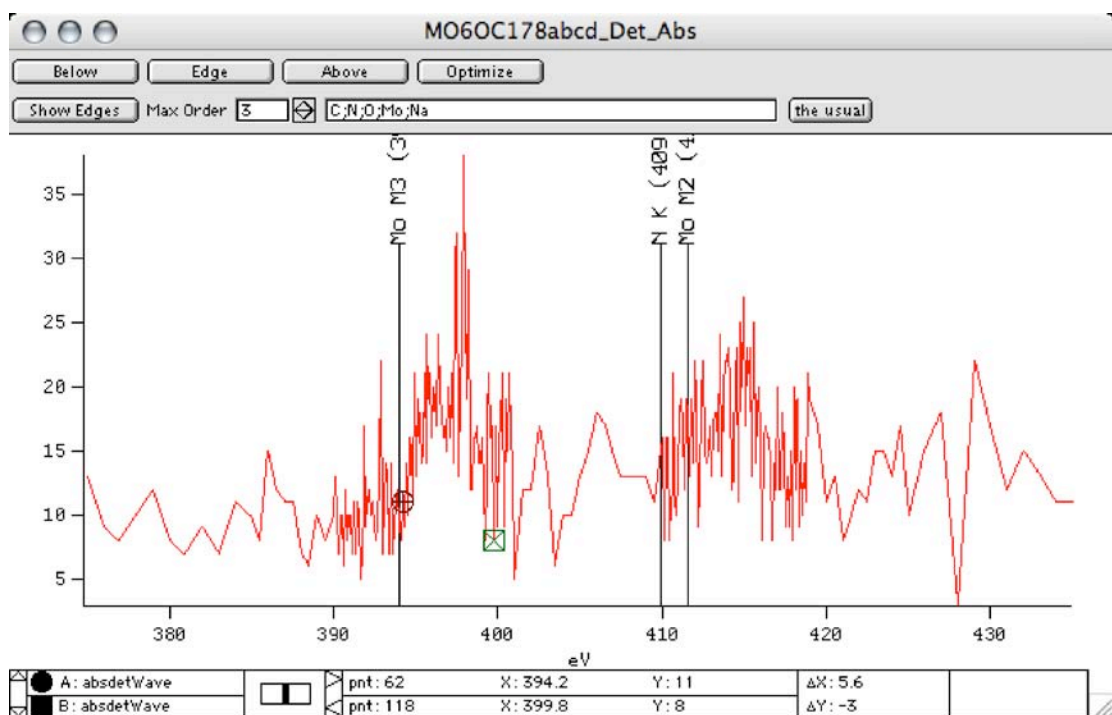


Figure 78: Detector pixel absorption spectrum tool.

the same window setting to all pixels (“set all” button), or manually adjust these windows for each pixel separately. The first option is very convenient when the response function of the different X-ray detectors are similar, which is typically the case for STJs from the same chip, as long as flux trapping is negligible. The second option is more useful if the response function is either very different, or if the lines are very weak and the correct choice of windows is crucial. Most commonly, we initially set the windows identical for all pixels, and then adjust them manually for highest S/N ratio.

The spectra can either be normalized by the I_0 measurement, or by division by the counts in one of the strong XRF lines in the spectrum, typically the oxygen K or carbon K fluorescence. Different spectra can be added, subtracted, multiplied and divided. A polynomial fit up to 19th order can be performed to the background, with user-selected regions over which the fit is supposed to extend. Further extensions of the software will be implemented after additional user input.

B Growth of Paramagnetic FAA Salt Pill

Cooling to temperatures below 0.1 K by adiabatic demagnetization is most commonly accomplished using iron ammonium sulfate dodecahydrate, commonly known among low-temperature physicists as FAA for ferric ammonium alum, because it has an ordering temperature of ~ 50 mK. Several properties of FAA must be taken into consideration for the fabrication of paramagnetic FAA salt pills for ADRs, which are not commercially available. FAA has an intrinsically poor thermal conductivity, and must therefore be grown as single crystals onto metal wires with high thermal conductivity. Also, FAA is corrosive, which requires these metal wires to be made of gold. Finally, the hydration of FAA is crucial to separate its spins for low residual internal fields after demagnetization, and requires the FAA to be enclosed into a leak tight container to prevent water loss to the cryostat under UHV conditions.

Iron ammonium sulfate is commercially available. A saturated solution is produced by adding FAA crystals to deionized water until crystals remain at the bottom. The saturated solution should be prepared in a container that will not be corroded, such as a Teflon beaker, since it will be kept on hand for the duration of the crystal growth over several weeks.

To grow an FAA paramagnet with the correct dimensions to fit inside the bore of the ADR magnet, a clear acrylic mold with the appropriate size is fabricated (Figure 79). Inside the mold, 63 high-purity 0.020 in. dia. wires (Figure 80) are placed in a hexagonal pattern with a maximum separation of ~ 0.1 in. between them. Teflon spacers at the top and the bottom of the mold hold the gold wires in place and ensure that they do not touch each other so that no eddy currents will be induced during the demagnetization cycle. The gold wires

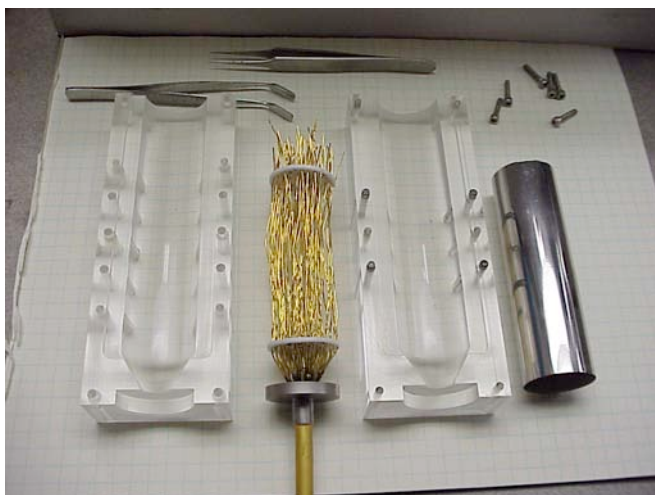


Figure 79: The FAA salt pill skeleton before its placement in mold and subsequent FAA crystal growth.

are brazed to an oxygen-free high-conductivity (OFHC) copper rod that can eventually be clamped to the rest of the 0.1 K detector stage, and to a stainless steel end cap that will form the lid of the leak tight enclosure of the FAA. To protect the brazing alloy from the FAA, the internal exposed joint is potted in Stycast epoxy.

The FAA single crystal is grown by slowly evaporating the saturated solution into the mold with the gold wires and the Teflon spacers (figure 27) Solution is added to a depth of ~ 5 mm each time, and a very gentle flow of clean nitrogen gas from a thin tube helps to accelerate water evaporation. The salt should have a slight pinkish color, indicating proper hydration. Figure 81 shows a layer of dehydrated FAA powder on the surface with a dark line of under-hydrated FAA. Rinsing with deionized water will clean the surface to reveal pink crystals whereupon crystal growth may resume.

The entire growth of the salt pill takes about two months. When the growth is finished, the final assembly of the paramagnet involves inserting the crystal into a thin stainless steel tube (Figure 82) with a wall thickness of 0.01 in. and an end cap on one side, and laser welding the other side to the stainless steel end cap on the OFHC copper rod. To prevent

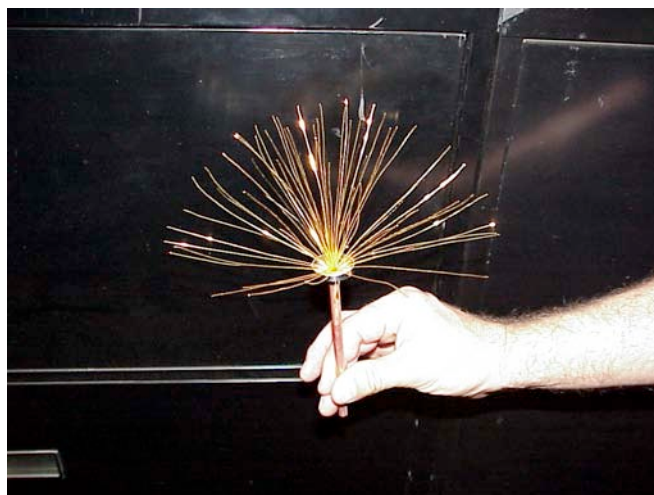


Figure 80: The gold thermal skeleton for the FAA salt pill.

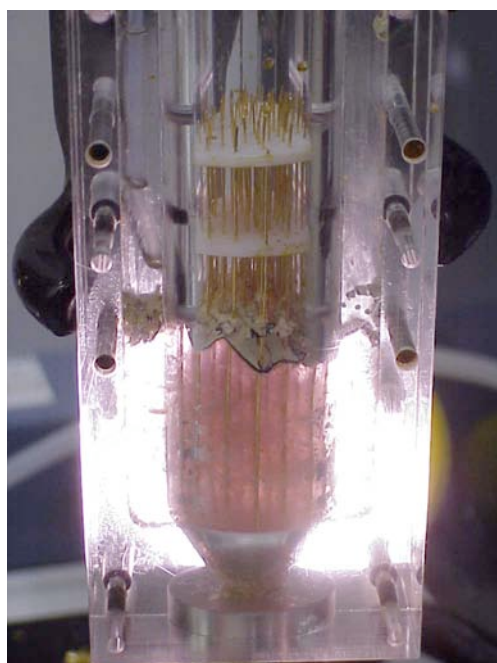


Figure 81: The FAA salt pill has dried out during crystal growth.



Figure 82: The FAA salt pill being inserted into the stainless steel can.

heating the crystal during welding, the end cap is bent by 90° so that the weld joint is at least 12 mm away from the FAA crystal.

The temperature of the FAA paramagnet must always remain below 40°C, the temperature at which the crystal starts to dehydrate, to prevent degradation of its paramagnetic properties. This temperature is well within reach on a hot summer day in California in a laboratory or a car without air conditioning. But if they are not exposed to elevated temperatures, the FAA paramagnets grown according to this procedure are relatively rugged and stable. So far, they have not shown any signs of degradation since they were first installed in various ADRs at LLNL about 8 years ago.

C Cryostat Maintenance

Maintenance on the cryostat should only be performed by researchers experienced in cryogenic engineering. Here we discuss the most common maintenance procedures, namely the assembly and re-tensioning of the support structures that hold the low-temperature stages. This is required periodically since the Kevlar strings used for their assembly lengthen over time, which causes the low-temperature stages to touch the higher-temperature shielding and thereby reduce the ADR hold time. We also briefly discuss the magnet and the heat switch assembly.

Suspension Tower Assembly The suspension system to support the 1 K and 0.1 K stages off the 4 K stage with minimal heat load, often referred to as “towers,” consists of an aluminum post mounted to the 4 K stage, a large molybdenum ring connected to the 1 K stage and a gold-plated copper post for the 0.1 K stage (Figure 83). The three parts are supported off another with Kevlar strings tied to wide nuts with through slots and rounded grooves (“string mounts”). The Kevlar is rated at 50 lbs. tensile strength and provides

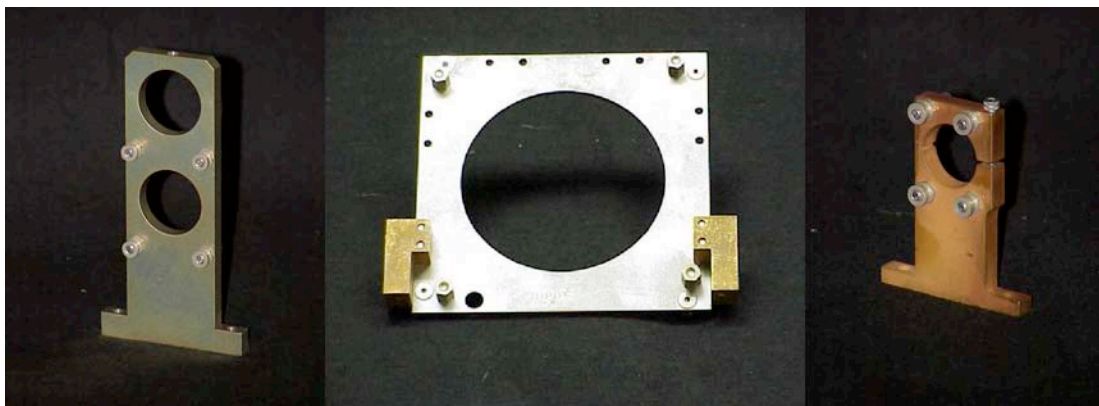


Figure 83: 4 K aluminum post (left), 1 K molybdenum ring (center) and 0.1 K gold-plated copper post (right) of the tower assembly.

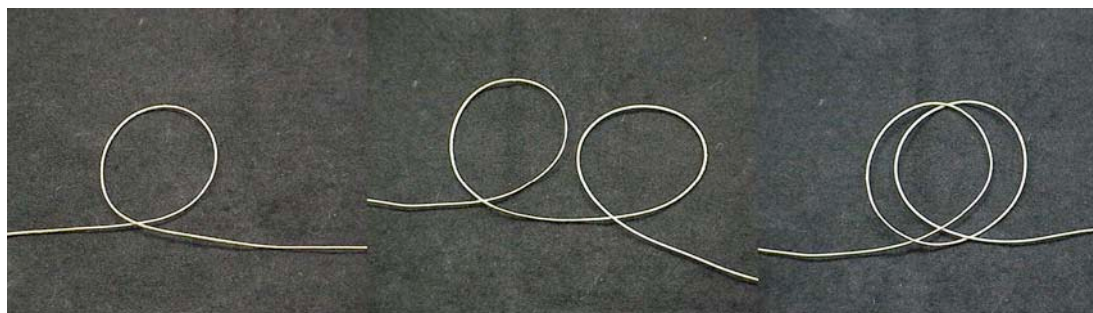


Figure 84: Kevlar string orientation for tying and clove hitch knot.

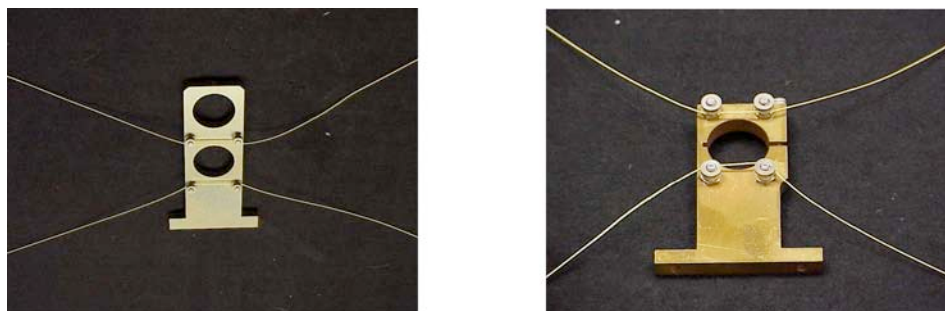


Figure 85: 4 K post—oblique view from above (left) and 0.1 K post—oblique view from below (right) after attaching the Kevlar strings. Note the orientation of the knots.

a compromise between good support and low thermal conductivity. The materials and dimensions of the posts are chosen to contract differently and thereby partially compensate for the lengthening of the Kevlar strings during cooldown.

For tower assembly, attach four string mounts to the 4 K aluminum posts with four $4-40 \times \frac{1}{2}$ " socket head cap screws such that their through slots face to the right. Connect a Kevlar string to the top two string mounts on the 4 K post using a clove hitch knot (Figure 84). Make the loops as shown, place the doubled loop over the string mounts and tighten the strings.

Repeat the procedure on the bottom two mounts on the same side of the 4 K posts. Attach two Kevlar strings to the 0.1 K post using the same string mounts and the same knotting procedure (Figure 85).

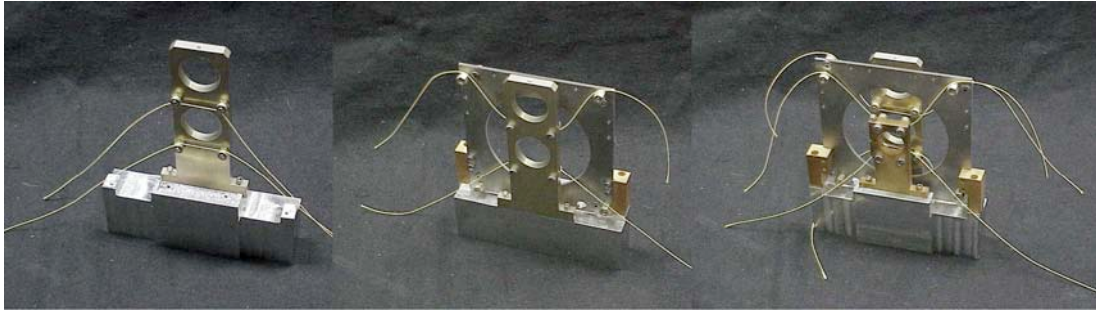


Figure 86: 4 K post (left), 4 K post and 1 K molybdenum ring (center) and 0.1 K and 4 K posts as well as 1 K molybdenum ring mounted on the alignment fixture.



Figure 87: Knot on the adjuster end of the Kevlar strings at the 1 K molybdenum ring. In this figure, the post (representing the adjuster) would rotate clock-wise.

Mount eight string adjusters to the 1 K molybdenum support ring using eight stainless steel $6-32 \times \frac{1}{4}$ " socket flat head cap screws. Assemble as shown in Figure 83 (center). Mount the 4 K aluminum post, the 1 K molybdenum support ring, and the 0.1 K gold-plated copper post to the temporary stringing fixture as shown in Figure 86. The fixture dimensions match the relative distances of the 1 K and 0.1 K stages in the cryostat for perfect alignment, and thus serve as a template during tower assembly.

The knot on the adjuster end of the Kevlar string is made by forming a loop, wrapping that loop around the adjuster, going under the lead-in ends of the string, and placing the loop over the end of the adjuster (Figure 87). Orient the loop on the adjuster such that the string pulls on the adjuster in clock-wise direction, so that the loop tightens the adjuster rather than loosening it. The first loop around will be free-space (up in Figure 86) end of



Figure 88: Fully assembled towers ready for tensioning and thermal cycling. Note the installation of the $\frac{1}{2}$ " spacer in the 0.1 K tower.

the adjuster and then cross over where the two strings double-back against the loop. Sailing knot theorists will recognize this as an especially weak knot. To mitigate this, the strings must wind around at least three more times ending up in the groove next to the molybdenum ring without any additional cross-overs.

Ensure that a $\frac{1}{2}$ " spacer is clamped snugly on the 0.1 K tower (Figure 88.) Tighten the adjuster to a torque of 30 ft.·lbs. and lock them in place with the socket flat head cap screws.

After stringing and tensioning, the assembly needs to be cycled thermally several times and re-tensioned, because Kevlar lengthens much more the first few times it is cooled to cryogenic temperatures than during later cooldowns. For this, put the assembly, while still mounted on the stringing fixture, into a clear plastic bag to prevent excessive ice build-up during warm-up. (Test the plastic bag. It may take a few tries to find one that does not fall apart at 77 K.) Dip the bag with assembly into liquid N₂ until the boil-off stops and the assembly is equilibrated at 77 K. Let it warm up to room temperature, then repeat the process. At this time, the strings will have to be re-tensioned to 30 ft.·lbs. After the final tensioning, the spacer may be removed if the particular tower is clamp the coldfinger.



Figure 89: (Left) Low-temperature assembly of the cryostat. (Right): Open ADR magnet shield.

Magnet and shield assembly to base plate It is unlikely that the ADR magnet, which has been in operation over the last eight years, will have to be taken apart and re-assembled. However, since the paramagnetic salt pills are only supported at the top end, they can become misaligned from the center of the ADR magnet over time and subsequently touch the inside of the magnet bore when the strong magnetic field of up to 5 T produces a radial force during the ADR cycle. This can significantly decrease the hold time of the ADR, especially when the 0.1 K and 4 K stages touch even at low or zero B-field.

To realign the paramagnets inside the ADR magnet, first remove the IR-blocking windows and the snout, and unsolder the connections to the ADR magnet and the heat switch. The entire magnet assembly with the 0.1 K and 1 K stages, the towers and the heat switch is attached to the 4 K He tank only with eight screws between the He tank and the 4 K base plate, and can then be taken out after these screws are removed (Figure 89 left).

The base of the ADR magnet shield can be removed, and the paramagnets inside can be re-aligned after loosening the clamps that hold them in place.

Heat Switch Assembly The heat switch will also likely never have to be taken apart and re-assembled. However, it may very occasionally become necessary to adjust the clamping



Figure 90: Top (left) and bottom (center) solenoids with plungers, attached to stainless steel blocks for mounting to heat switch frame. (Right): Heat switch clamps with the stainless steel links at the top, and the gold-plated OFHC copper “boot” at the bottom that forms the thermal path between the 4 K He bath and the low-temperature stages.

pressure or lubricate the joints. Also, improper high-current operation may burn out the solenoids or the current leads and require their replacement.

The top solenoid is a conical-face Lucas solenoid (part #9824 129409-031), and the bottom solenoid is a flat-faced Lucas solenoid (part #9945 129440-031). They are attached to the heat switch frame with two stainless steel blocks (Figure 90).

The plungers push the links on top of the C-shaped stainless steel clamps that open or close to make contact between the 4 K He bath and the low temperature stages. The two links are attached to the top of the C-clamps with 0.187" diameter 1.00" long dowel pins with a groove at each end to accept a retaining ring. A gold-plated OFHC copper “boot” pivots around the “foot” of the clamps to form the thermal path through two copper braids (Figure 90, right). The “boot” is attached to the “foot” with two springs, which in turn are held in place with 0.03" diameter piano wire pins bent to match each part. For assembly, place the springs in the holes in the front of the foot and hold them in place with the 0.03" pins. Take two pieces of monofilament fishing line, fold it over into a loop, and slip it through the holes in the front of the boot. Hook these loops onto the springs and pull the

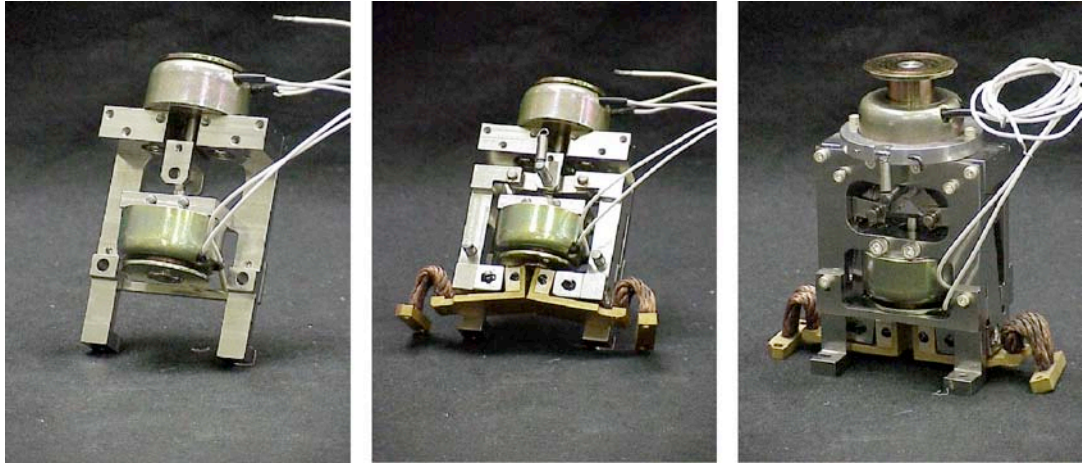


Figure 91: Heat switch assembly.

springs into the boot until you can insert the other pins and hold the other end of the spring inside the boot. Then pull the boot and foot apart just enough to slip the $\frac{3}{16}$ " ball into the socket between the two parts around which the boot can pivot. The remaining heat switch assembly is straightforward, attaching the clamps and solenoids to the heat switch frame with 6-32 screws (Figure 91).

If the heat switch starts to open and close unreliably even when increasing the voltage to ~ 60 V (while limiting the current to < 2 A to avoid burning out the leads), its joints can be lubricated with graphite powder, or the pressure of the clamps can be adjusted with the screws on the bottom of the clamps.

References

- [Abrikosov 57] A. A. Abrikosov. *On the Magnetic Properties of Superconductors of the Second Group*. Journal of Experimental and Theoretical Physics, vol. 5, no. 6, pages 1174–1182, December 1957. (Translated from Zh. Eksp. i Teor. Fiz. vol. 32 page 1442, 1957).
- [Bardeen 57] J. Bardeen, L. N. Cooper & J. R. Schrieffer. *Theory of Superconductivity*. Physical Review, vol. 108, no. 5, pages 1175–1204, December 1957.
- [Barfknecht 91] A. T. Barfknecht, R. C. Ruby & H. L. Ko. *A simple and robust niobium Josephson junction integrated circuit process*. Magnetics, IEEE Transactions on, vol. 27, no. 2, pages 3125–3128, March 1991.
- [Barfknecht 93] A.T. Barfknecht, R.C. Ruby, R.C. Ruby & G.S. Lee. *Josephson junction integrated circuit process with planarized PECVD SiO₂ dielectric*. Applied Superconductivity, IEEE Transactions on, vol. 3, no. 1, pages 2201–22003, March 1993.
- [Bearden 67] J. A. Bearden. *X-Ray Wavelengths*. Reviews of Modern Physics, vol. 39, no. 1, page 78, Jan 1967.
- [Bechstein 04] S. Bechstein, B. Beckhoff, R. Fliegau, J. Weser & G. Ulm. *Characterization of an Nb/Al/AlO_x/Al/Nb superconducting tunnel junction detector with a very high spatial resolution in the soft X-ray range*. Spectrochimica Acta Part B: Atomic Spectroscopy, vol. 59, no. 2, pages 215–221, February 2004.
- [Beinert 83] Helmut Beinert & Andrew J. Thomson. *Three-iron clusters in iron-sulfur proteins*. Archives of Biochemistry and Biophysics, vol. 222, no. 2, pages 333–361, April 1983.
- [Beinert 97] Helmut Beinert, Richard H. Holm & Eckard Munck. *Iron–Sulfur Clusters: Nature’s Modular, Multipurpose Structures*. Science, vol. 277, no. 5326, pages 653–659, 1997.
- [Bishop 86] Paul E. Bishop, R. Premakumar, Dennis R. Dean, Marty R. Jacobson, John R. Chisnell, Thomas M. Rizzo & Jennifer Kopczynski. *Nitrogen Fixation by Azotobacter vinelandii Strains Having Deletions in Structural Genes for Nitrogenase*. Science, vol. 232, no. 4746, pages 92–94, 1986.
- [Bolin 93] J. T. Bolin, N. Campobasso, S. W. Muchmore, T. V. Morgan & L. E. Mortenson. *Structure and Environment of Metal-Clusters in the Nitrogenase Molybdenum Iron Protein From Clostridium-Pasteurianum*. ACS Symposium Series, vol. 535, pages 186–195, 1993.

- [Booth 87] N. E. Booth. *Quasiparticle trapping and the quasiparticle multiplier*. Applied Physics Letters, vol. 50, no. 5, pages 293–295, 1987.
- [Burgess 96] B.K. Burgess & D.J. Lowe. *Mechanism of Molybdenum Nitrogenase*. Chemical Reviews, vol. 96, no. 7, pages 2983–3012, 1996.
- [CANBERRA 88] CANBERRA. *Home Page*. <http://www.canberra.com>, 1988.
- [Casimir 39] H. B. G. Casimir, W. J. de Haas & D. de Klerk. *Measurements on iron ammonium alum*. Physica, vol. 6, pages 241–254, 1939.
- [Cooper 56] Leon N. Cooper. *Bound Electron Pairs in a Degenerate Fermi Gas*. Physical Review, vol. 104, no. 4, pages 1189–1190, November 1956.
- [Crabtree 04] George W. Crabtree, Mildred S. Dresselhaus & Michelle V. Buchanan. *The Hydrogen Economy*. Physics Today, vol. 57, no. 12, pages 39–45, December 2004.
- [Cramer 77] S. P. Cramer. PhD thesis, Stanford University, 1977.
- [Cramer 78] Stephen P. Cramer, Keith O. Hodgson, William O. Gillum & Leonard E. Mortenson. *The Molybdenum Site of Nitrogenase. Preliminary Structural Evidence From X-Ray Absorption Spectroscopy*. Journal of the American Chemical Society, vol. 100, no. 11, pages 3398–3407, 1978.
- [Cramer 91] S. P. Cramer, F. M. F. DeGroot, Y. Ma, C. T. Chen, F. Sette, C. A. Kipke, D. M. Eichhorn, M. K. Chan, W. H. Armstrong & et al. *Ligand field strengths and oxidation states from manganese L-edge spectroscopy*. Journal of the American Chemical Society, vol. 113, no. 21, pages 7937–7940, 1991.
- [CXRO 07] CXRO. *Center for X-Ray Optics*. <http://www.cxro.lbl.gov>, 2007.
- [Dance 03] Ian Dance. *The consequences of an interstitial N atom in the FeMo cofactor of nitrogenase*. Chemical communications, no. 3, pages 324–325, 2003.
- [de Groot 90] F. M. F. de Groot, J. C. Fuggle, B. T. Thole & G. A. Sawatzky. *2p x-ray absorption of 3d transition-metal compounds: An atomic multiplet description including the crystal field*. Physical Review B, vol. 42, no. 9, pages 5459–5468, September 1990.
- [de Korte 92] Piet A. J. de Korte, Marcel L. van den Berg, Marcel P. Bruijn, M. Frericks, J. B. le Grand, J. G. Gijsbertsen, E. P. Houwman & Jaap Flokstra. *Superconductive tunnel junctions for X-ray spectroscopy*. In Oswald H. W. Siegmund, editeur, Proceedings of SPIE, volume 1743, pages 24–35. SPIE, 1992.

- [Della Pergola 96] R. Della Pergola, C. Bandini, F. Demartin, E. Diana, L. Garlaschelli, P. L. Stanghellini & P. Zanello. *Characterization, redox properties and structures of the iron nitridocarbonyl clusters $[Fe_4N(CO)_{11}\{PPh(C_5H_4FeC_5H_5)_2\}]^-$, $[Fe_6N(CO)_{15}]^{3-}$ and $[Fe_6H(N)(CO)_{15}]^{2-}$* . Journal of the Chemical Society-Dalton Transactions, no. 5, pages 747–754, Mar 1996.
- [Deng 93] Haibin Deng & Roald Hoffmann. *How N_2 Might Be Activated by the FeMo-Cofactor in Nitrogenase*. Angewandte Chemie International Edition in English, vol. 32, no. 7, pages 1062–1065, 1993.
- [Drury 05] O. B. Drury & S. Friedrich. *Sensitivity and S/N-ratio of superconducting high-resolution X-ray spectrometers*. Applied Superconductivity, IEEE Transactions on, vol. 15, no. 2, pages 613–617, June 2005.
- [Drury 06] Owen B. Drury, Stephan Friedrich, Simon J. George & Stephen P. Cramer. *The advantages of soft X-rays and cryogenic spectrometers for measuring chemical speciation by X-ray spectroscopy*. Nuclear Instruments and Methods in Physics Research Section A: Accelerators, Spectrometers, Detectors and Associated Equipment, vol. 559, pages 728–730, 2006.
- [Eady 96] R. R. Eady. *Structure-Function Relationships of Alternative Nitrogenases*. Chemical Reviews, vol. 96, no. 7, pages 3013–3030, 1996.
- [Einsle 02] O. Einsle, F. A. Tezcan, S. L. A. Andrade, B. Schmid, M. Yoshida, J. B. Howard & D. C. Rees. *Nitrogenase MoFe-Protein at 1.16 Resolution: A Central Ligand in the FeMo-Cofactor*. Science, vol. 297, no. 5587, pages 1696–1700, September 2002.
- [Fano 47] U. Fano. *Ionization Yield of Radiations. II. The Fluctuations of the Number of Ions*. Physical Review, vol. 72, no. 1, pages 26–29, July 1947.
- [Fisher 73] R. A. Fisher, G. E. Brodale, E. W. Hornung & W. F. Giauque. *Magnetothermodynamics of gadolinium gallium garnet. I. Heat capacity, entropy, magnetic moment from 0.5 to 4.2 °K, with fields to 90 kG along the [100] axis*. The Journal of Chemical Physics, vol. 59, no. 9, pages 4652–4663, November 1973.
- [Fons 06] Paul Fons, Hiroshi Tampo, Alexander V. Kolobov, Masataka Ohkubo, Shigeru Niki, Junji Tominaga, Roberta Carboni, Federico Boscherini & Stephan Friedrich. *Direct Observation of Nitrogen Location in Molecular Beam Epitaxy Grown Nitrogen-Doped ZnO*. Physical Review Letters, vol. 96, no. 4, page 045504, 2006.

- [Frank 98] M. Frank, C. A. Mears, S. E. Labov, L. J. Hiller, J. B. le Grand, M. A. Lindeman, H. Netel, D. Chow & A. T. Barfknecht. *Cryogenic high-resolution X-ray spectrometers for SR-XRF and microanalysis*. Journal of Synchrotron Radiation, vol. 5, no. 3, pages 515–517, May 1998.
- [Friedrich 99a] S. Friedrich, L. J. Hiller, M. Frank, B. le Grand J., C. A. Mears, B. Niderost, S. E. Labov, A. T. Barfknecht, M. LeGros & S. P. Cramer. *Superconducting high-resolution X-ray detectors for metalloprotein L-edge spectroscopy*. Journal of Electron Spectroscopy and Related Phenomena, vol. 101-103, pages 891–896, June 1999.
- [Friedrich 99b] S. Friedrich, J. B. Le Grand, L. J. Hiller, J. Kipp, M. Frank, S. E. Labov, S. P. Cramer & A. T. Barfknecht. *High resolution tunnel junction extreme ultraviolet detectors limited by quasiparticle counting statistics*. Applied Superconductivity, IEEE Transactions on, vol. 9, no. 2, pages 3330–3333, June 1999.
- [Friedrich 01a] S. Friedrich, L. J. Hiller, M. F. Cunningham & S. E. Labov. *Line-splitting in high-resolution superconducting tunnel junction EUV detectors*. Applied Superconductivity, IEEE Transactions on, vol. 11, no. 1, pages 836–839, 2001.
- [Friedrich 01b] S. Friedrich, T. Niedermayr, O. Drury, M. F. Cunningham, M. L. van den Berg, J. N. Ullom, A. Loshak, T. Funk, S. P. Cramer & J. D. Batteux. *A superconducting detector endstation for high-resolution energy-dispersive SR-XRF*. Nuclear Instruments and Methods in Physics Research Section A: Accelerators, Spectrometers, Detectors and Associated Equipment, vol. 467–468, pages 1117–1120, July 2001.
- [Friedrich 02] S. Friedrich, T. Funk, O. Drury, S. E. Labov & S. P. Cramer. *A multichannel superconducting soft x-ray spectrometer for high-resolution spectroscopy of dilute samples*. Review of Scientific Instruments, vol. 73, no. 3, pages 1629–1631, 2002.
- [Friedrich 03] S. Friedrich, A. Vailionis, O. Drury, T. Niedermayr, T. Funk, W. N. Kang, Eun-Mi Choi, Hyeong-Jin Kim, Sung-Ik Lee, S. P. Cramer, Changyoung Kim & S. E. Labov. *A multichannel superconducting tunnel junction detector for high-resolution X-ray spectroscopy of magnesium diboride films*. Applied Superconductivity, IEEE Transactions on, vol. 13, no. 2, pages 1114–1119, 2003.
- [Friedrich 05] Stephan Friedrich, Rolf Fliegauf, Matthias Frank, Markus Veldkamp, Simon Labov, Burkhard Beckhoff & Gerhard Ulm. *The spectral response of superconducting tunnel junction X-ray detectors*. Nuclear Instruments and Methods in Physics Research Section A: Accelerators, Spectrometers, Detectors and Associated Equipment, vol. 551, no. 1, pages 35–45, 2005.

- [Friedrich 06a] Stephan Friedrich, Owen B. Drury, Stephen P. Cramer & Peter G. Green. *A 36-pixel superconducting tunnel junction soft X-ray detector for environmental science applications*. Nuclear Instruments and Methods in Physics Research Section A: Accelerators, Spectrometers, Detectors and Associated Equipment, vol. 559, no. 2, pages 776–778, 2006.
- [Friedrich 06b] Stephan Friedrich, Philippe Lerch & Eugenie Kirk. *Design of a 8x14 pixel Ta-based STJ X-ray detector array*. Nuclear Instruments and Methods in Physics Research Section A: Accelerators, Spectrometers, Detectors and Associated Equipment, vol. 559, no. 2, pages 477–479, April 2006.
- [Fröhlich 50] H. Fröhlich. *Theory of the Superconducting State. I. The Ground State at the Absolute Zero of Temperature*. Physical Review, vol. 79, no. 5, pages 845–856, September 1950.
- [FS4 06] FS4. *Iron–Sulfur Cluster*. Hetero-compound Information Centre - Uppsala, HIC, 2006.
- [Funk 04] T. Funk, W. Gu, S. Friedrich, H. Wang, S. Gencic, D.A. Grahame & S.P. Cramer. *Chemically Distinct Ni Sites in the A-Cluster in Subunit β of the Acetyl-CoA Decarbonylase/Synthase Complex from Methanosarcina hermophila: Ni L-Edge Absorption and X-ray Magnetic Circular Dichroism Analyses*. Journal of the American Chemical Society, vol. 126, no. 1, pages 88–95, 2004.
- [George 90] G. N. George, W. E. Cleland, J. H. Enemark, B. E. Smith, C. A. Kipke, S. A. Roberts & Stephen P. Cramer. *L-Edge spectroscopy of molybdenum compounds and enzymes*. Journal of the American Chemical Society, vol. 112, no. 7, pages 2541–2548, 1990.
- [George 98] G. N. George, S. J. George & I. J. Pickering. *EXAFS-PAK, Stanford Synchrotron Radiation Laboratory*. <http://www-ssrl.slac.stanford.edu/exafspak.html>, 1998.
- [Giaever 60] Ivar Giaever. *Electron Tunneling Between Two Superconductors*. Physical Review Letters, vol. 5, no. 10, pages 464–466, November 1960.
- [Goldie 94] D. J. Goldie, P. L. Brink, C. Patel, N. E. Booth & G. L. Salmon. *Statistical noise due to tunneling in superconducting tunnel junction detectors*. Applied Physics Letters, vol. 64, no. 23, pages 3169–3171, 1994.
- [Gorter 34a] C. J. Gorter & H. Casimir. *On supraconductivity I*. Physica, vol. 1, no. 1, pages 306–320, 1934.

- [Gorter 34b] C. J. Gorter & H. Casimir. *Zur Thermodynamik des supraleitenden Zustandes*. Physik. Zeitschr., vol. 35, pages 963–966, 1934.
- [Gray 78] K. E. Gray. *A superconducting transistor*. Applied Physics Letters, vol. 32, no. 6, pages 392–395, 1978.
- [Gresham05] Gresham Scientific Instruments, Ltd. *Home Page*. <http://www.gsinst.com>, 2005.
- [Gu 03] Weiwei Gu, L. Jacquamet, D. S. Patil, H-X. Wang, D. J. Evans, M. C. Smith, M. Millar, S. Koch, D. M. Eichhorn, M. Latimer & S. P. Cramer. *Refinement of the nickel site structure in Desulfovibrio gigas hydrogenase using range-extended EXAFS spectroscopy*. Journal of Inorganic Biochemistry, vol. 93, no. 1–2, pages 41–51, January 2003.
- [Hagmann 94] C. Hagmann & P. L. Richards. *Two-stage magnetic refrigerator for astronomical applications with reservoir temperatures above 4 K*. Cryogenics, vol. 34, no. 3, pages 221–226, March 1994.
- [HEC 06] HEC. *Heme c*. Hetero-compound Information Centre - Uppsala, 2006.
- [Heer 54] C. V. Heer, C. B. Barnes & J. G. Daunt. *The Design and Operation of a Magnetic Refrigerator for Maintaining Temperatures below 1[degree]K*. Review of Scientific Instruments, vol. 25, no. 11, pages 1088–1098, 1954.
- [Hinnemann 03] B. Hinnemann & J. K. Norskov. *Modeling a Central Ligand in the Nitrogenase FeMo Cofactor*. Journal of the American Chemical Society, vol. 125, no. 6, pages 1466–1467, 2003.
- [Hull 41] J. R. Hull & R. A. Hull. *Tables of Thermodynamic Functions of Paramagnetic Substances and Harmonic Oscillators*. The Journal of Chemical Physics, vol. 9, no. 6, pages 465–469, 1941.
- [IR Labs 06] IR Labs. *Infrared Laboratories Home Page*. <http://www.irlabs.com>, 2006.
- [Jaklevic 77] J. Jaklevic, J. A. Kirby, M. P. Klein, A. S. Robertson, G. S. Brown & P. Eisenberger. *Fluorescence detection of EXAFS: Sensitivity enhancement for dilute species and thin films*. Solid State Communications, vol. 23, no. 9, pages 679–682, September 1977.
- [Josephson 62] B. D. Josephson. *Possible new effects in superconductive tunnelling*. Physics Letters, vol. 1, no. 7, pages 251–253, 1962.
- [Kim 92] Jongsun Kim & D. C. Rees. *Crystallographic structure and functional implications of the nitrogenase molybdenum-iron protein from Azotobacter vinelandii*. Nature, vol. 360, no. 6404, pages 553–560, 1992.

- [Kim 93] Jongsun Kim, D. Woo & D. C. Rees. *X-ray Crystal Structure of the Nitrogenase Molybdenum–Iron Protein from Clostridium Pasteurianum at 3.0- Resolution*. Biochemistry, vol. 32, no. 28, pages 7104–7115, 1993.
- [Kochoyan 91] M. Kochoyan, T.F. Havel, D.T. Nguyen, C.E. Dahl, H.T. Keutmann & M.A. Weiss. *Alternating zinc fingers in the human male associated protein ZFY: 2D NMR structure of an even finger and implications for “jumping-linker” DNA recognition*. RCSB Protein Data Bank, 5ZNF, 1991.
- [Kraus 89] H. Kraus, F. von Feilitzsch, J. Jochum, R. L. Mossbauer, Th. Peterreins & F. Probst. *Quasiparticle trapping in a superconductive detector system exhibiting high energy and position resolution*. Physics Letters B, vol. 231, no. 1–2, pages 195–202, 1989.
- [Krause 79] M. O. Krause. *Atomic radiative and radiationless yields for K and L shells*. Journal of Physical and Chemical Reference Data, vol. 8, no. 2, pages 307–327, April 1979.
- [Kurakado 82] M. Kurakado. *Possibility of high resolution detectors using superconducting tunnel junctions*. Nuclear Instruments and Methods, vol. 196, no. 1, pages 275–277, 1982.
- [Labov 92] Simon E. Labov, Carl A. Mears, George W. Morris, Charles E. Cunningham, Mark A. LeGros, Eric H. Silver, Andrew T. Barfknecht, Norman W. Madden, Don A. Landis, Fred S. Goulding, Roger W. Bland & Kenneth E. Laws. *Superconducting tunnel-junction X-ray detectors with niobium absorbers and aluminum quasi-particle traps*. In Oswald H. W. Siegmund, editeur, Proceedings of SPIE, volume 1743, pages 328–338. SPIE, October 1992.
- [le Grand 98] J. B. le Grand, C. A. Mears, L. J. Hiller, M. Frank, S. E. Labov, H. Netel, D. Chow, S. Friedrich, M. A. Lindeman & A. T. Barfknecht. *A superconducting tunnel junction x-ray detector with performance limited by statistical effects*. Applied Physics Letters, vol. 73, no. 9, pages 1295–1297, August 1998.
- [Lebow06] Lebow Company. *Home Page*. <http://www.lebowcompany.com>, 2006.
- [Lee 97] Hong-In Lee, Brian J. Hales & Brian M. Hoffman. *Metal-Ion Valencies of the FeMo Cofactor in CO-Inhibited and Resting State Nitrogenase by ^{57}Fe Q-Band ENDOR*. Journal of the American Chemical Society, vol. 119, no. 47, pages 11395–11400, 1997.
- [Lepy 00] M. C. Lepy, J. L. Campbell, J. M. Laborie, J. Plagnard, P. Stemmler & W. J. Teesdale. *Experimental study of the response of semiconductor detectors to low-energy photons*. Nuclear Instruments and Methods

- in Physics Research Section A: Accelerators, Spectrometers, Detectors and Associated Equipment, vol. 439, no. 2–3, pages 239–246, 2000.
- [London 35] F. London & H. London. *The Electromagnetic Equations of the Supraconductor*. The Proceedings of the Royal Society of London. Series A Mathematical and Physical Sciences, vol. 149, pages 71–88, March 1935.
- [Lordi 03] Vincenzo Lordi, Vincent Gambin, Stephan Friedrich, Tobias Funk, Toshiyuki Takizawa, Kazuyuki Uno & James S. Harris. *Nearest-Neighbor Configuration in (GaIn)(NAs) Probed by X-Ray Absorption Spectroscopy*. Physical Review Letters, vol. 90, no. 14, page 145505, April 2003.
- [Maxwell 50] Emanuel Maxwell. *Isotope Effect in the Superconductivity of Mercury*. Physical Review, vol. 78, no. 4, page 477, May 1950.
- [Mayer 99] Suzanne M. Mayer, David M. Lawson, Carol A. Gormal, S. Mark Roe & Barry E. Smith. *New Insights into Structure-function Relationships in Nitrogenase: A 1.6 Resolution X-ray Crystallographic Study of Klebsiella pneumoniae MoFe-protein*. Journal of Molecular Biology, vol. 292, no. 4, pages 871–891, October 1999.
- [McGuire 72a] Eugene J. McGuire. *Atomic M-Shell Coster-Kronig, Auger, and Radiative Rates, and Fluorescence Yields for Ca-Th*. Physical Review A, vol. 5, no. 3, pages 1043–1047, Mar 1972.
- [McGuire 72b] Eugene J. McGuire. *Atomic M-Shell Coster-Kronig, Auger, and Radiative Rates and Fluorescence Yields for Ca-Th*. Physical Review A, vol. 6, no. 2, page 851, Aug 1972.
- [Mears 93] C. A. Mears, Simon E. Labov & A. T. Barfknecht. *Energy-resolving superconducting X-ray detectors with charge amplification due to multiple quasiparticle tunneling*. Applied Physics Letters, vol. 63, no. 21, pages 2961–2963, 1993.
- [Meissner 33] W. Meissner & R. Ochsenfeld. *Ein Neuer Effekt bei Eintritt der Supraleitähigkeit*. Naturwissenschaften, vol. 21, no. 44, pages 787–788, November 1933.
- [Melcher 05] C. L. Melcher, S. Friedrich, S. P. Cramer, M. A. Spurrier, P. Szupryczynski & R. Nutt. *Cerium oxidation state in LSO:Ce scintillators*. Nuclear Science, IEEE Transactions on, vol. 52, no. 5, pages 1809–1812, October 2005.
- [Nordgren 00] Joseph Nordgren & Jinghua Guo. *Instrumentation for soft X-ray emission spectroscopy*. Journal of Electron Spectroscopy and Related Phenomena, vol. 110-111, pages 1–13, 2000.

- [Ohkubo 02] M. Ohkubo, K. Suzuki, K. Tanabe, H. Pressler & M. Ukibe. *Vortex trapping in superconducting tunnel junction detectors*. In AIP Conference Proceedings, volume 605, pages 55–58. AIP, 2002.
- [Onnes 11] H. Kammerling Onnes. Leiden Communications, vol. 119b, 120b, 122b, and 124c, 1911.
- [Parallax05] Parallax Research, Inc. *Home Page*. <http://www.parallax-x-ray.com>, 2005.
- [Piamonteze 07] Cinthia Piamonteze, Simon J. George, Francis E. Jenney Jr., Michael W. W. Adams, Karl Fisher, William E. Newton, Jacques Meyer, Yasuhiro Ohki, Kazuyuki Tatsumi & Stephen P. Cramer. *X-ray absorption spectroscopy as a tool for probing Fe valence state in Fe-S proteins*. in preparation, 2007.
- [Pippard 53] A. B. Pippard. *An Experimental and Theoretical Study of the Relation between Magnetic Field and Current in a Superconductor*. Proceedings of the Royal Society of London. Series A, Mathematical and Physical Sciences, vol. 216, no. 1127, pages 547–568, February 1953.
- [Rando 92] N. Rando, A. Peacock, A. van Dordrecht, C. Foden, R. Engelhardt, B. G. Taylor, P. Gare, J. Lumley & C. Pereira. *The properties of niobium superconducting tunneling junctions as X-ray detectors*. Nuclear Instruments and Methods in Physics Research Section A: Accelerators, Spectrometers, Detectors and Associated Equipment, vol. 313, no. 1–2, pages 173–195, 1992.
- [Rees 03] Douglas C Rees & James B Howard. *The Interface Between the Biological and Inorganic Worlds: Iron–Sulfur Metalloclusters*. Science, vol. 300, no. 5621, pages 929–931, May 2003.
- [Rehr 00] J. J. Rehr & R. C. Albers. *Theoretical approaches to x-ray absorption fine structure*. Reviews of Modern Physics, vol. 72, no. 3, pages 621–654, Jul 2000.
- [Reynolds 50] C. A. Reynolds, B. Serin, W. H. Wright & L. B. Nesbitt. *Superconductivity of Isotopes of Mercury*. Physical Review, vol. 78, no. 4, page 487, May 1950.
- [Ryder 77] P. L. Ryder. *Theoretical Analysis of Statistical Limitations to the Accuracy and Spectral Resolution in Energy Dispersive X-Ray Analysis*. Scanning Electron Microscopy, vol. 1, pages 273–280, 1977.
- [Schrock 06] Richard R. Schrock. *Nitrogen Fixation Special Feature: Reduction of dinitrogen*. Proceedings of the National Academy of Sciences, vol. 103, no. 46, pages 17087–, 2006.

- [Segall 00] K. Segall, C. Wilson, L. Frunzio, L. Li, S. Friedrich, M. C. Gaidis, D. E. Prober, A. E. Szymkowiak & S. H. Moseley. *Noise mechanisms in superconducting tunnel-junction detectors*. Applied Physics Letters, vol. 76, no. 26, pages 3998–4000, 2000.
- [Statham 95] P. J. Statham. Quantifying the benefits of resolution and count rate in edx microanalysis, chapitre 8, pages 101–126. Plenum Press, New York, 1995.
- [van den Berg 03] Marcel L. van den Berg, Jan D. Batteux & Simon E. Labov. *Electro-Mechanical Heat Switch for Cryogenic Applications*. US Patent Number 6532759 B1, March 2003.
- [Veldkamp 02] M. Veldkamp, B. Beckhoff, R. Fliegauf, G. Ulm, M. Frank, S. Friedrich & S. E. Labov. *Characterization of superconducting tunnel junction X-ray detectors by means of monochromatized undulator radiation*. Nuclear Instruments and Methods in Physics Research Section A: Accelerators, Spectrometers, Detectors and Associated Equipment, vol. 487, no. 3, pages 450–456, July 2002.
- [VeriCold07] VeriCold Technologies GmbH. *Home Page*. <http://www.vericold.de/>, 2007.
- [Yano 05] J. Yano, Y. Pushkar, P. Glatzel, A. Lewis, K. Sauer, J. Messinger, U. Bergmann & V. Yachandra. *High-Resolution Mn EXAFS of the Oxygen-Evolving Complex in Photosystem II: Structural Implications for the Mn₄Ca Cluster*. Journal of the American Chemical Society, vol. 127, no. 43, pages 14974–14975, 2005.
- [Zehnder 95] A. Zehnder. *Response of superconductive films to localized energy deposition*. Physical Review B, vol. 52, no. 17, pages 12858–12866, November 1995.